Integration of Piezoelectric Sensing and Control for Nano-Scale Vibration Suppression in Hard Disk Drives

by

Sarah Helen Felix

A dissertation submitted in partial satisfaction of the
requirements for the degree of
Doctor of Philosophy

in

Engineering-Mechanical Engineering

in the

GRADUATE DIVISION
of the
UNIVERSITY OF CALIFORNIA, BERKELEY

Committee in charge:
Professor Roberto Horowitz, Chair
Professor Masayoshi Tomizuka
Professor Richard White

Spring 2010

Integration of Piezoelectric Sensing and Control for Nano-Scale Vibration Suppression in Hard Disk Drives

Abstract

Integration of Piezoelectric Sensing and Control for Nano-Scale Vibration Suppression in Hard Disk Drives

by

Sarah Helen Felix
Doctor of Philosophy in Engineering-Mechanical Engineering

University of California, Berkeley

Professor Roberto Horowitz, Chair

Industry goals for magnetic recording are currently in the terabit-per-square-inch regime, with hard disk drives (HDDs) remaining a competitive technology for server level data storage. Such ultrahigh data density requires a multifaceted approach to HDD servo systems, which need to provide nanometer-scale positioning of the read/write head. Dual-stage actuation has been extensively studied and advanced actuation schemes have been deployed in commercial prototypes. However, sensing technology remains limited, since servo sectors on the disk provide the only position information in state-of-the-art commercial drives. This work takes an integrated mechatronic approach to combine a novel sensing scheme with appropriate control methods to improve vibration suppression and tracking.

The major contribution of this work is fabrication, implementation, and evaluation of a novel piezoelectric strain sensor integrated into a PZT-actuated HDD suspension. The sensors consisted of thin-film ZnO fabricated directly onto the steel suspension structure that carries the read/write head. This technology required extensive process development, but allowed for the addition of sensors at arbitrary locations without significantly altering the dynamics of the suspension design. Moreover, the sensors had excellent resolution in the high frequency range where mechanical modes in the suspension are problematic. As a benchmark comparison, a similar PZT-actuated suspension was implemented using self-sensing, wherein a bridge circuit was used to extract a sensing signal from the PZT actuators. Both strategies were deployed in experimental disk drives and used to measure and model system dynamics.

Feedback control was explored using the auxiliary ZnO sensors, with the objective of targeting high-frequency structural vibrations excited by airflow. Optimal closed-loop control simulations with a nominal plant model predicted up to 30% improvement in suppression of windage-induced vibrations with high-resolution strain sensing at increasing sampling rates. A simple feedback damping controller was successfully operated experimentally on instrumented suspension prototypes. Finally, an adaptive lattice filter was formulated that utilized strain sensing to respond to uncertain disturbance conditions and attain optimal performance online. Simulations demonstrated that the filter achieved rapid recovery of optimal performance when varying windage disturbed the suspension.

To my sisters, forever friends.

Contents

List of Figures

List of Tables

Acknowledgments

Six years have brought many people across my path, and all have contributed to my journey and accomplishment in different ways. It is important for me to recount and recognize how so many people played a role in the completion of this project.

First an foremost, I want to thank Professor Roberto Horowitz, who not only guided my research and challenged me to keep my theoretical mind sharp, but also treated us like family. I also appreciate the unwavering behind-the-scenes support of Professor Masayoshi Tomizuka, my "academic grandfather". He has been there as a teacher, committee member for the qualifying exam and dissertation, and recommendation writer. Professor Al Pisano deserves special thanks for providing me valuable guidance and support on several occasions as if I were one of his own students. Thanks also to Professors Laurent El Ghaoui, Kameshwar Poolla, and Richard White, who amicably agreed to serve as committee members for the qualifying exam and dissertation, and provided useful outside perspectives.

The project described in this dissertation is unique in that it was supported by partners in the data storage industry. Hutchinson Technology, Western Digital, the Data Storage Institute in Singapore, and other members of the Information Storage Industry Consortium and Computer Mechanics Laboratory closely followed, and participated in, the progress of this research effort. Particular thanks go to Michael Tiller and Jacob Bjornstrom for directly supporting the fabrication of the instrumented suspension prototypes. Other notable supporters of the instrumented suspension project include Ong Eng Hong, Cynthia Hipwell, Alexei Sacks, and Bob Evans.

The students in our lab group have been a tremendous help to me throughout my graduate career. I can't thank Kenn Oldham and Stanley Kon enough for their many hours of training and help with microfabrication processes. As senior lab members during my early years, Ryozo Nagamune and Jeongun Choi lent me helpful advice and encouragement, especially when it came to crafting my first conference papers. Richard Conway, Josiah Wernow, Claus Danielson, and especially Jianbin Nie, assisted greatly in the realization of my research. Thanks to Professor Bogy and his students, particularly Liang Pan, Sripathi Canchy, and Sean Mosely, for their hospitality and assistance when I used their lab space.

Other UC Berkeley staff members provided invaluable support as well. Pat Giddings and Donna Craig have consistently welcomed me into their office for help with smiles and open doors. Beatriz Lopez-Flores encouraged me to expand my horizons both in Berkeley and abroad. The excellent staff at the Berkeley Micolab provided unparalleled support and professionalism without which most of this work would not have been possible. I have to give special thanks to Brian McNeil, Joe Donnelly, and Mike Linan, for many hours spent away from their home turf trouble-shooting and repairing the sputtering machine in our lab. I also owe thanks to the faculty, students, and industry visitors in the Esashi Lab at Tohoku University in Sendai, Japan. Their hospitality and expertise helped me accomplish a great deal in a short amount of time.

This project was financially supported by the National Science Foundation, the Information Storage Industry Consortium, and the Computer Mechanics Laboratory.

Finally, warm and humble thanks to my family for their understanding and encouragement during this long process. I couldn't have done it without you!

Chapter 1

Introduction

1.1 Background

Hard disk drives (HDDs) are among the most complex electro-mechanical systems encountered in daily life. Precision engineering of subsystems such as magnetic materials, aerodynamics, tribology, and servo control has enabled the storage capacity and performance of HDDs to keep up with aggressive trends of the computer microprocessor industry, as predicted by Moore's Law. Even with the advent of new data storage technologies, the HDD continues to thrive as the most cost effective, reliable solution for rewritable, very high density data storage. It remains a key technology particularly with the growing popularity of server-based cloud computing, novel hybrid enterprize storage solutions, and servers for home media storage. Since data density is the most competitive figure of merit of the HDD, it is critical to continue increasing data capacity at a rapid rate. The current industry target is 1 Tbit/in^2, with advanced research and development beginning to consider 4 Tbit/in^2. This corresponds to data track widths of 50 nanometers or less. Performance specifications in the nanoscale regime necessitate advanced technology leaps in all of the HDD subsystems.

The servo subsystem of the disk drive is a key candidate for improving data storage capacity because it increases tracking precision, enabling adjacent tracks to be placed closer together on the disk. Servo control is required to compensate for two main sources of tracking errors. The first source is track runout, which describes the extent to which the data track itself deviates from a perfect circle. The second source comes from disturbances such as disk flutter, external shock, and airflow; which cause the read/write head to move away from the track. Several key components comprise the conventional disk drive servo system, as illustrated in Fig. 1.1. The magnetic read/write head is suspended over the disk by an arm consisting of a rigid E-block that rotates around a pivot, and a flexible load beam called the suspension. The voice coil motor (VCM) rotates the E-block around the pivot, sweeping the magnetic read/write head to different radial locations across the spinning disk. The read/write head detects its radial position when the head flies over dedicated servo sectors on the disk which indicate how far away the head is from the center of a data track. This is called the position error signal, or PES. The PES feeds

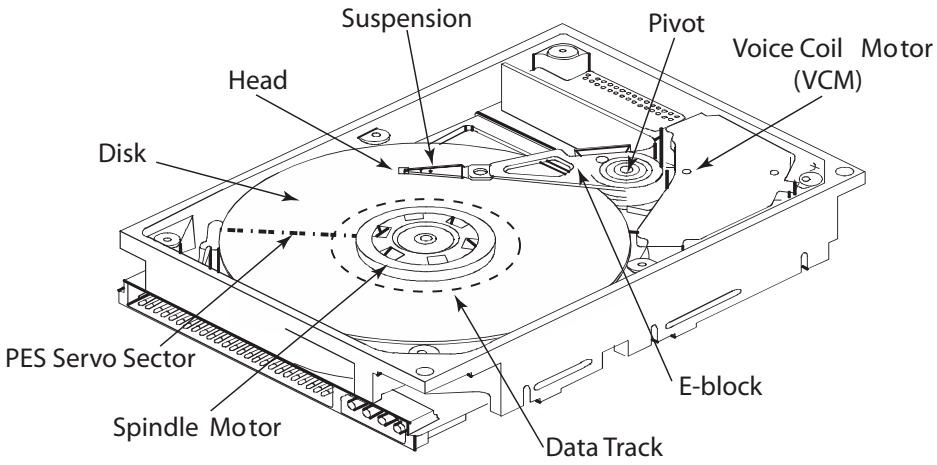

Figure 1.1: A conventional hard disk drive (HDD).

back into a control algorithm that directs the motion of the VCM, thus completing the servo loop. This configuration has remained largely unchanged since the invention of the HDD. Improvements have involved either mechanical design of the components to tailor the dynamics of the system, or novel control algorithms that extract better performance. However, HDD technology has encountered fundamental obstacles in achieving the latest storage capacity goals. In particular, the conventional servo system is unable to adequately suppress structural vibration that are caused by airflow.

1.2 Motivation

1.2.1 Fundamental Limitations

By a careful balance of structural loads and aerodynamic interactions, the read/write head is designed to fly over the disk surface while the disk is spinning. The fly height in state-of-the-art drives is on the order of only a few nanometers. While the airflow caused by the spinning disk is necessary to maintain this fly height, the flow itself can excite problematic vibrations in the suspension structure. In the past, the motion caused by these vibrations have been within the specification for allowable off-track error. However, with higher data densities and closer tracks, the airflow induced force, called *windage*, becomes the dominant contributor to off-track error. For example, 1 Tbit/in^2 density corresponds to a tracking precision requirement of 1.5 nm RMS. Unsuppressed structural vibrations can cause tracking error on the order of 10-50 nm RMS, and can occur at frequencies above 1 kHz.

The conventional system described in the previous section can only do so much to attenuate these high frequency vibrations for two main reasons: the bandwidth of the

VCM actuator, and the sample rate of the PES signal. The bandwidth of the VCM in a closed-loop controller is defined by the range of frequencies over which vibrations are reduced in magnitude. However, Bode's Integral Theorem dictates that outside of this frequency range, disturbances will actually be amplified [1]. The structural vibrations in the suspension occur downstream of the VCM, so it is easy for the relatively massive VCM to excite these vibrations. Moreover, a control system becomes more sensitive to uncertainties in the model. In other words, with a perfect model, a VCM controller could be designed to suppress high frequency vibrations, but because of inevitable uncertainty in the high-frequency range and phase spillover, slight variations in the dynamics would cause such a system to become unstable.

As for the PES sampling rate, in a conventional HDD the PES is obtained by reading dedicated servo sectors permanently encoded onto the disk. Thus, the PES sampling rate is fixed by the disk rotation speed and the number of servo sectors, limiting detection of high-frequency disturbances such as windage. It is undesirable to increase the number of servo sectors because they occupy space that could be used for data bits. Increasing the rotation rate of the disk can actually cause additional vibration, noise, and heat problems [2]. Currently, typical PES sampling rates are as high as 30 kHz. Because of aliasing effects, this allows servo compensation at and below the associated Nyquist frequency of 15 kHz. On top of that, a discrete time system model is a good equivalent to a continuous time system when bandwidth of the closed-loop system is one tenth of the sampling rate [3], further limiting the target controller bandwidth to only 3 kHz.

Various techniques have been employed to attenuate windage-excited frequencies that are beyond the bandwidth of the conventional servo. These include multi-rate discrete-time notch filtering [4] and mode cancelation by a stable digital resonance [5]. These schemes rely on accurate models of the disk drive system dynamics. They may lack adequate robustness when many problematic vibration modes occur at uncertain frequencies that are higher than the Nyquist frequency associated with the PES.

1.2.2 Dual-Stage Actuation

The bandwidth of the servo system can be increased by placing a second actuator, called a "dual-stage" actuator closer to the read/write head. Such an actuator can enable a higher bandwidth than the conventional VCM, and can be located beyond the region of suspension vibrations. Researchers have proposed much new technology involving dual-stage actuation. Various dual-stage servo configurations place a microactuator in the flexible suspension [6] [7] [8] [9], between the suspension and slider containing the read/write head [10] [11] [12] [13], or embedded in the slider itself [14] [15]. These arrangements provide increasing bandwidth from the microactuator in exchange for increasing design and processing complexity. While such configurations have demonstrated improved tracking in the laboratory, practical implementation of such devices has proven difficult because of contamination, mechanical robustness, electrical interconnect requirements, and process integration. At this time, to the best of the author's knowledge, the only dual-stage configuration actually deployed in commercial products is lead zirconate titanate (PZT) suspension-based actuation because

of its relative simplicity and robustness.

1.2.3 Auxiliary Sensing

Another way to increase the servo bandwidth is to integrate auxiliary sensing to obtain a vibration signal at an arbitrarily high sampling rate. Researchers have studied different types of sensors mounted at various locations in the drive to aid in improved servo tracking performance. Accelerometers mounted on the disk drive casing have been used to cancel the effect of external disturbances, for example, in [16]. Reference [17] used strain sensors attached to the VCM to suppress the effect of the actuator's butterfly mode. Bulk PZT-actuated suspensions have been modified to provide sensing information [18] [19] [20] [21]. However, this limits the placement and sensitivity of the sensors, and the large actuator elements have a significant effect on the suspension dynamics. Piezoelectric PVDF has also been investigated for strain sensing and actuation in disk drives [22], [23]. While this polymeric material is more flexible than PZT, it has only been demonstrated as a bulk sheet element bonded to the suspension, similar to PZT. The concept of instrumented suspensions with dedicated miniaturized sensors optimally located on the suspension was first proposed by [24]. Our group demonstrated fabrication and implementation of thin-film ZnO sensors directly onto a suspension structure, decoupling the design of actuators and sensors [25]. The thin-film material does not significantly alter the dynamics of the suspension design. Furthermore, the additive and subtractive processes involved with thin-film fabrication are similar to those used in existing state-of-the-art suspension fabrication. Thus, such sensors could be more economical to integrate than components that require costly assembly steps.

1.3 Strategy and Organization

It is clear that market requirements dictate the adoption of certain technologies. Therefore, a comprehensive mechatronic solution takes into account relevant constraints. A sensing solution should consider feasibility of fabrication and process integration. The evaluation of such sensing should accurately assess the potential for key performance improvements. The control design solution should be theoretically transparent, computationally tractable, and feasible to implement. The work in this dissertation attempts to address these matters, while incorporating emerging microscale technology and appropriate control design tools. The major original contribution of this work is the implementation of novel thin-film sensors in combination with dual-stage actuation in a control system designed for suppression of windage vibrations in a HDD.

The system proposed in this work used thin-film processing technology to integrate piezoelectric strain sensors onto a suspension design with minimal modification to the suspension structure. We selected thin piezoelectric ZnO film to provide a strain-sensing signal by detecting vibrations from both the suspension and the servo arm assembly. I compared this configuration to a previously established strategy that used self-sensing techniques to extract a strain measurement signal from a piezoelectric element that is

simultaneously used for actuation. To best exploit the new auxiliary sensing signal for vibration suppression, I performed several studies and experiments using different closed-loop control designs.

The remainder of this dissertation is organized as follows: Chapter 2 describes the development and fabrication of so-called *instrumented suspensions* using thin-film ZnO strain sensors. Chapter 3 presents the results of testing instrumented suspension prototypes. Chapter 4 describes an alternative method of strain sensing using self-sensing PZT actuation. Chapter 5 discusses closed-loop control design using ZnO strain sensing, and presents both simulation and experimental results. Finally, Chapter 6 summarizes the work and offers recommendations for future directions of the project.

Chapter 2

Thin-Film Strain Sensors

The novel sensing configuration presented here uses thin-film piezoelectric sensors fabricated directly onto HDD suspensions. Since these elements are for dedicated sensing use, their placement on the suspension component can be customized and treated separately from any actuators. Also, thin-film sensors, totalling about 3 to 4 μm in thickness have negligible effect on the dynamics of the 35 μm thick steel suspension. This chapter describes material selection and fabrication of the sensors. It includes some review of sensor design concepts that were previously developed in [26] and [27] and were applied to the prototypes fabricated for this work. In addition, this work includes significant additional process development and characterization that was completed during the fabrication of the prototypes used here, as well as an additional study of PZT thin-film deposition on steel substrates.

2.1 Material Selection and Design

2.1.1 Material Selection

Commonly used piezoelectric thin films are lead zirconate titanate (PZT), zinc oxide (ZnO), and aluminum nitride (AlN). Table 2.1 gives properties for these materials. These films have been used for silicon devices such as resonators, surface acoustic wave filters, atomic force microscopy cantilevers, and other sensors and transducers [28, 29, 30, 31, 32, 33]. Fabricating instrumented suspensions, however, introduces unique fabrication challenges due to the fact that the substrate is made of steel, rather than silicon. The primary constraint is processing temperature due to the thermal expansion differential between steel and piezoelectric thin-film materials. ZnO is a good choice because it can be deposited at a low temperature ($\sim 300^\circ$ C) and is easier to deposit than PZT, since PZT requires a high-temperature annealing step. Also notice that PZT, while typically the material of choice for piezoelectric actuators, does not perform as well for sensing applications. Compared to ZnO, AlN has a similar range of processing temperatures and material properties, such as coefficient of thermal expansion. However, the RF power for the AlN sputtering process is higher and can heat up a steel substrate quicker. It is a feasible candidate, but

Table 2.1: Material properties for piezoelectric sensing candidates

PROPERTY	SYMBOL	UNITS	ZnO	AlN	PZT
Piezoelectric constant	e_{31}	C/m	**.51-.57**	**.58**	**6.5**
Permittivity	ϵ_{33}	-	**10.2-11**	**10.7**	**1470**
Sensing sensitivity per unit film thickness (ϵ_0 is permittivity of vacuum)	$S = (\frac{e_{31}}{\epsilon_0 \epsilon_{33}})$	10^3V/μ	**5.2-6.3**	**6.1**	**.5**
Thermal expansion (at 300K, $\perp$ to c-axis)	α_t	10^{-6}K^{-}1	**4.3**	**4.4**	
Processing temperature	T_p	^{o}C	**300**	**20**	**600**
REFERENCES			[34],[35] [36],[38]	[36],[37],[33] [39],[31]	[34]

would require careful tuning of the sputtering power to control substrate temperature. I used ZnO for the instrumented suspensions fabricated for this work, since Kon previously determined suitable processing conditions for this material [26]. At the end of this chapter is a section describing an additional study that I conducted to evaluate the feasibility of PZT thin films on steel substrates.

2.1.2 Design For Mode Selectivity

Windage excites different structural modes in the suspensions which contribute in varying degrees to off-track motion. For example, the *sway* mode, in which the suspension moves in a yawing motion, directly affects off-track error. A *torsional* mode contributes a small component of motion in the off-track direction as the suspension twists about its long axis. Finally, a *bending* mode makes practically no contribution to off-track motion as the read/write head moves up and down in a pitching motion. More complex modes may contain a combination of sway, torsion, and bending displacements. Fig. 2.1 shows the frequency response magnitudes of a typical PZT-actuated HDD. Along with the suspension modes described above, the dynamics include a rigid-body *flex cable* mode at a low frequency, and a *butterfly* mode that describes a characteristic vibration in the E-block. The most problematic modes for servo control are the ones that cause displacement in the off-track direction, so it is important for the sensor signal to emphasize these modes and minimize signals from non-off-track modes.

Ref. [40] discussed ways to address non-off-track modes in the control design. These techniques added more states to the controller dynamics to account for the non-off-track modes explicitly, increasing the order of the controller. Ideally, we would like to design sensors that have the desired modal selectivity, so that the controller order does not have to be so large. Since the thin-film sensor shape and location can be customized, we used two methods to incorporate modal selectivity into the sensor design itself. The first is using an optimization algorithm to choose the location and shape of the sensors [27]. The second concept is to interconnect symmetrical sensors to cancel the signal from some non-off-track

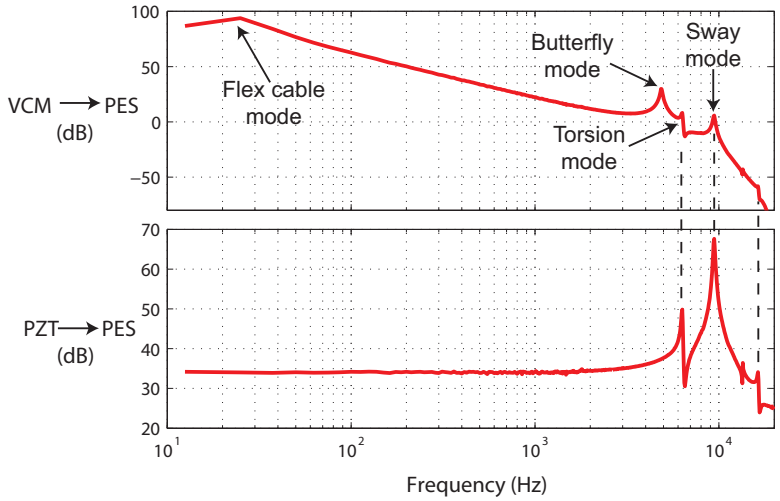

Figure 2.1: Typical frequency response magnitude for a PZT-actuated HDD.

modes. These two techniques, described below, were both incorporated into the prototype instrumented suspensions.

LQG Optimization Algorithm

A cost function for optimizing sensor location should weight more heavily vibration signals from off-track modes. A quadratic cost function based on linear quadratic gaussian control [1] can be constructed which penalizes off-track motion under closed-loop control using measurements from sensor signals. Thus, the cost function directly evaluates how effective a sensor configuration would be in a closed-loop controller. A continuous-time state space model of the HDD servo system was constructed as follows:

$$\begin{aligned} \dot{x} &= Ax + Bu + B_w w \\ y &= C(\Phi)x + \nu(\Phi) \\ z &= C_z x, \end{aligned} \tag{2.1}$$

where $x \in \mathbb{R}^n$ is the state vector, A, B, B_w, C, and C_z are system matrices, $u \in \mathbb{R}^m$ is the control input with m actuators, w is the scalar windage input disturbance with spectral density $\mathbb{W}$, ν is the measurement noise with spectral density $\mathbb{V}$, and y is the sensor strain measurement The variable z is the off-track motion of the read/write head induced by the windage and control inputs. Φ refers to a specific sensor configuration. An LQG controller minimizes the following H_2 norm, J_{H_2}:

$$J_{H_2} = \min_{K,F(\Phi)} E[z^2 + u^T R u], \tag{2.2}$$

where $F(\Phi)$ denotes the Kalman filter gain for a given $C(\Phi)$, and K denotes the optimal linear stationary controller [1]. The variance of off-track motion z is penalized, and R is

a matrix that penalizes the actuator effort. However, since the actuator range of motion is typically much larger than the suspension vibrations, the problem may be simplified by solving the case of "cheap control", *i.e.*, $R \to 0$, as described in [27]. Note that the norm J_{H_2} is a function of sensor configuration, Φ, so the sensor optimization problem is stated as

$$\min_{\Phi} J_{H_2}(\Phi). \tag{2.3}$$

The computation of J_{H_2} requires the solution of a Riccati equation [1], making the evaluation of many sensor configurations numerically intensive. However, two conditions that tend to be satisfied in HDD suspensions lead to an algebraic approximation of the solution [27]. In the following equations, we use subscripts to indicate elements of the B, C, and C_z matrices, e.g., b_{ik}, c_{ji} or $c_{z,j}$.

1. Vibration modes are widely spaced:

$$|\omega_i - \omega_j| >> 0, \tag{2.4}$$

   where ω_i is the resonant frequency of mode i.

2. Sensor noise is large relative to other parameters:

$$|c_{ji}|(\sum_{k=1}^{l} |b_{ik}|)\sqrt{\frac{\mathbb{W}}{\mathbb{V}}} << 1, \tag{2.5}$$

   for all i and j, where l is the number of states.

Then, the quadratic cost function can be approximated by

$$J_{H_2} \approx \sum_{j=1}^{N} \frac{c_{z,j}^2 b_j \sqrt{\mathbb{W}\mathbb{V}}}{\sqrt{c_{1j}^2 + \ldots + c_{rj}^2}}. \tag{2.6}$$

This expression significantly reduces computation time and provides better intuition about how different system parameters enter into the cost. See [41] for details on the validity of the above assumptions and the derivation of the approximation in Eq. (2.6).

To implement this optimization method on instrumented suspensions, we obtained a finite element model of the suspension to compute $x-$, $y-$, and shear ($xy-$) components of strain. We computed the strain at each element of the spatially-discretized model according to contributions from each mode. For example, the matrix

$$C_{\epsilon_x}(p) = \begin{bmatrix} c_{x1} & 0 & c_{x2} & 0 & \ldots & 0 \end{bmatrix} \tag{2.7}$$

describes the contribution of each vibration mode to strain, ϵ_x, in the $x-$direction at element p. Similar vectors are calculated for strain in the $y-$ and shear ($xy-$) directions. Then the $C(\Phi)$ matrix is given by

$$C(\Phi) = \frac{\sum_{p\in\Phi} A_p \Xi \begin{bmatrix} C_{\epsilon_x}(p) \\ C_{\epsilon_y}(p) \\ C_{\epsilon_{xy}}(p) \end{bmatrix}}{C_L + \sum_{p\in\Phi} \frac{A_p \varepsilon_f}{t_f}}. \tag{2.8}$$

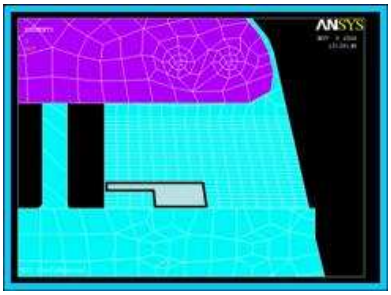

Figure 2.2: ANSYS model of one sensor configuration near the hinge of an instrumented suspension. *Image courtesy Stanley Kon.*

In this expression, A_p is the area of element p, Ξ is a matrix of piezoelectric coefficients in the $x-$, $y-$, and shear directions, C_L is the parasitic capacitance of external leads, ε_f is the permittivity of the piezoelectric film, and t_f is the strain gage thickness. This $C(\Phi)$ matrix was computed for every sensor configuration and the cost function was evaluated using the algebraic approximation in Eq. (2.6). Fig. 2.2 shows an ANSYS model of one sensor configuration near the hinge of a suspension. Note that the ANSYS model need only be run once to obtain coefficients for each element. A program was written to automatically generate reasonable combinations of elements and compute their corresponding cost function. In this way, more than fifty sensor configurations were easily evaluated.

Symmetrical Interconnected Sensors

It is possible to exploit symmetry in a sensor configuration to minimize the response from non-off-track modes. Two symmetrical sensors placed on each side of the suspension hinge will pick up equal signals from prominent non-off-track displacement modes, such as the first bending mode. On the other hand, signals from off-track modes will be 180 degrees out of phase (i.e. have the opposite sign). Thus, if the signal from one sensor is subtracted from the that of other, off-track signals will be amplified by a factor of two, while non-off-track modes will be canceled. Reference [26] proposed the concept of interconnecting symmetrical sensors and provided an ANSYS simulation as validation. Here we experimentally demonstrate mode cancelation using symmetric interconnected PZT elements.

In these tests, I used a PZT-actuated suspension donated by Hutchinson Technology, Inc. On this suspension, two PZT elements that were poled in opposite directions could be hardwired together with a common electrode as ground, as shown in Fig. 2.3. In this way, they were in a suitable configuration to be used as sensors. I installed the suspension in an experimental HDD with no disk so that an excitation from the voice coil motor (VCM) could be applied. Also, a laser doppler velocimeter (LDV) focused on the slider measured off-track motion. Fig. 2.4 shows the frequency responses from VCM excitation to off-track motion, and from the VCM to interconnected PZT sensing output. By comparing the two, we can see that the PZT detects the important off-track modes. The non-off-track

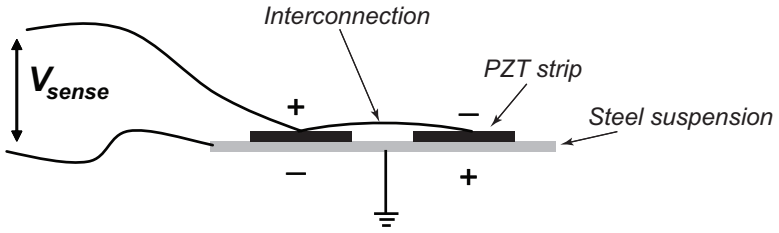

Figure 2.3: Schematic of the wiring used for testing mode cancelation with interconnected piezoelectric elements.

modes that appear are fairly small in magnitude. Next, I physically separated the two PZT elements so that only one PZT was used as a sensor. Fig. 2.4 also shows the frequency response from the VCM to single PZT sensor. In this measurement, non-off-track modes have become more prominent, and the overall signal is not as clean.

Mode cancelation was incorporated into the thin-film sensor design by joining the metal interconnects in such a way that the the difference between the voltage across two symmetrical sensors is measured. Fig. 2.5 shows the interconnect layout to achieve this.

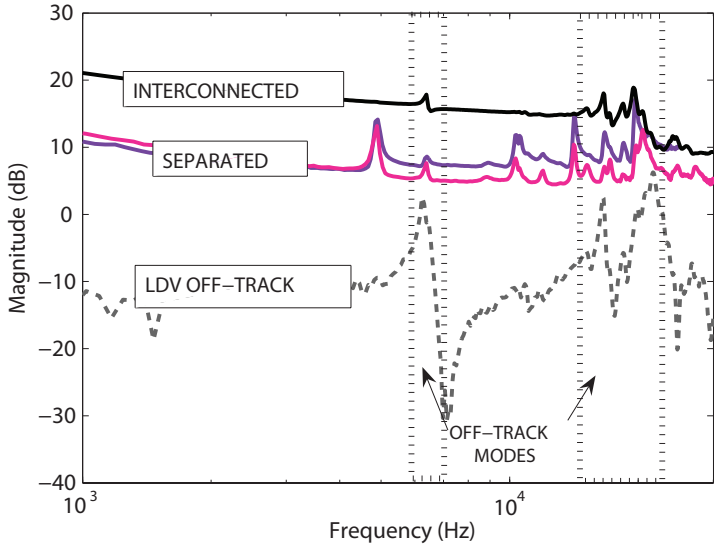

Figure 2.4: Experimental demonstration of used symmetrical interconnected sensors for mode selectivity.

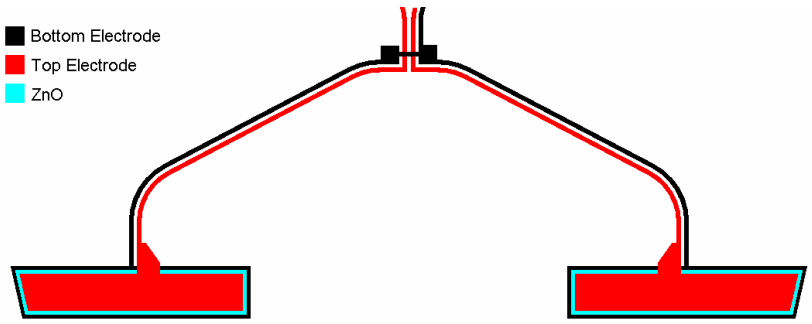

Figure 2.5: Layout for interconnecting thin-film sensors to achieve non-off-track mode cancellation.

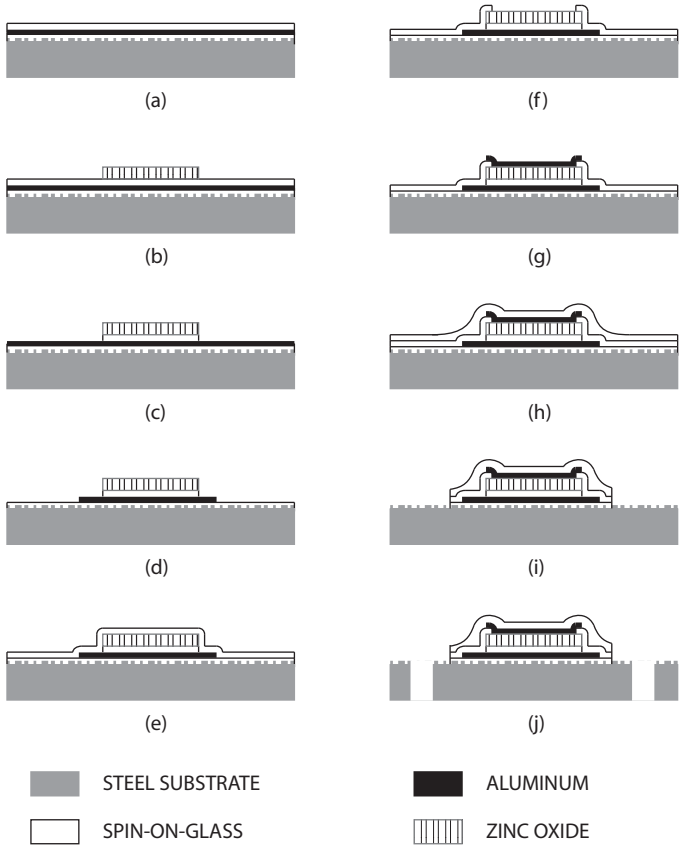

Figure 2.6: Fabrication process flow for instrumented suspensions.

2.2 Fabrication and Characterization

2.2.1 Process Flow

Fig. 2.6 illustrates the process flow for fabricating ZnO strain gages on steel suspensions. There were several special steps that were required to accommodate the steel substrate.

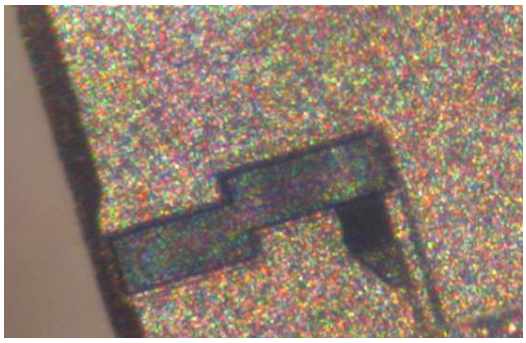

Figure 2.7: Photograph of an actual sensor near the hinge of a suspension prototype. Significant undercut from steel etch can be seen on the left edge as a dark strip.

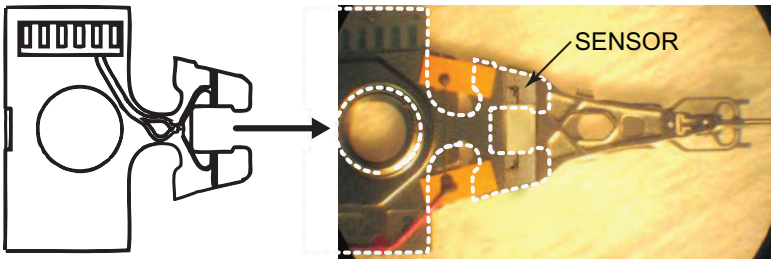

Figure 2.8: Hinge geometry and completed instrumented suspension prototype.

The 35 μm thick 304 stainless steel wafer has a rough surface from a microfabrication standpoint. Furthermore, it is flexible, conductive, subject to oxidation, and presents problems with thermal expansion differences. First, a 0.5-μm thick layer of spin-on-glass (SOG) was deposited onto the steel substrate. This served to planarize the surface, protect it from oxidation, and electrically insulate the substrate from the sensors. Next, a 0.17-μm thick aluminum layer was evaporated onto the wafer. A second SOG layer promoted adhesion of the ZnO and smoothed out the stress gradient between the aluminum and ZnO (Fig. 2.6a). A smooth surface was critical for subsequent ZnO deposition. The process for depositing the ZnO film was RF magnetron sputtering. The deposition rate at 300° C with 200 W forward power, 3.5 mTorr oxygen, and 3.5 mTorr argon was approximately 0.8 μm per hour. Films of 0.8-1 μm have demonstrated good piezoelectric properties. Next, the ZnO sensors were patterned using a wet etch consisting of a 10:10:200 ratio of phosphoric acid, acetic acid, and water, respectively (Fig. 2.6b). The underlying SOG layer was etched in a 90/10 mixture of SF_6/O_2 plasma using the ZnO as a mask (Fig. 2.6c). After this, the bottom Al electrode and leads were patterned and wet etched using potassium ferricyanide, potassium hydroxide, and water in a ratio of 10:1:100. (Fig. 2.6d). A third SOG layer provided insulation (Fig. 2.6e). Contact holes were etched in this SOG layer (Fig. 2.6f). A second layer of aluminum was evaporated and patterned it to definde the top electrode and interconnects (Fig. 2.6g). One more layer of SOG provided passivation and protection of the sensors (Fig. 2.6h). Finally, all the layers of SOG outside of the area of the sensor were etched (Fig. 2.6i). The steel wafers were bulk micromachined at Hutchinson Technology,

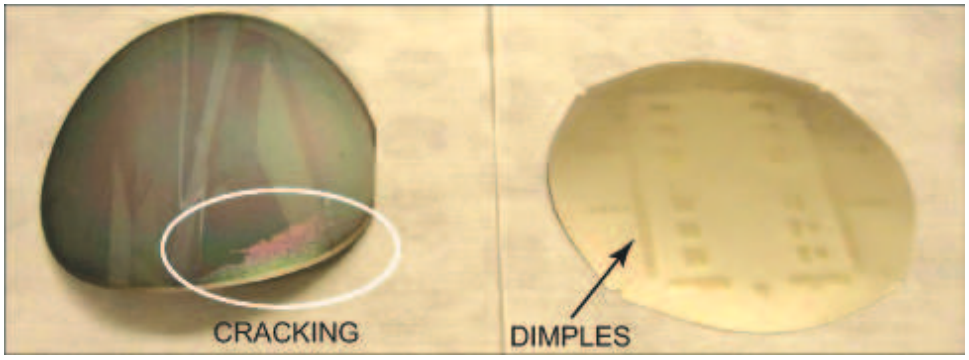

Figure 2.9: Problems with ZnO deposition on steel wafers. A single blanket layer of ZnO resulted in dramatic warping and cracking (left). The wafer on the right had patches of ZnO deposited through a stencil mask, resulting in localized dimples.

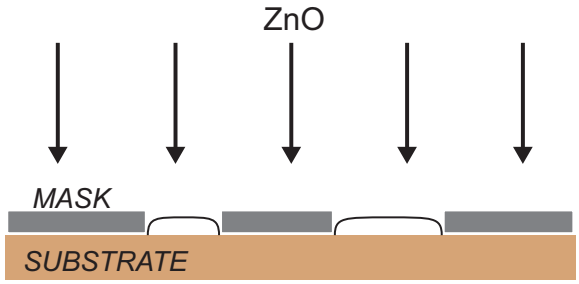

Figure 2.10: Shadow mask method to deposit ZnO only in localized areas.

Inc., using a proprietary process to define the suspension geometry (Fig. 2.6j). At several steps throughout the process, it was necessary to bond the flexible wafers to Si handle wafers using a drop of water. An illustration of a completed sensor is in Fig. 2.7. The area of the largest sensor is about .25 mm^2. Fig. 2.8 shows the outline of the etched steel hinge and its location in a finished suspension prototype.

2.2.2 Challenges

Although the process sequence is relatively simple, the fabrication of instrumented suspensions was uniquely challenging because the substrate was a thin (35 μm) steel wafer. For example, the use of SOG and handle wafers described above is among the special steps that were developed to accommodate the steel substrates. There were two points in the process that were particularly troublesome: the ZnO film deposition, and the lithography for final bulk steel etching. Ref. [26], which describes the original development of an instrumented suspension process, made several recommendations for possibly improving these steps. In fabricating devices for the work in this dissertation, I followed these recommendations. In both cases, the recommended modifications did not work as expected, but the observations and final processes are described in this section.

The most challenging fabrication step posed by processing on a steel substrate was the

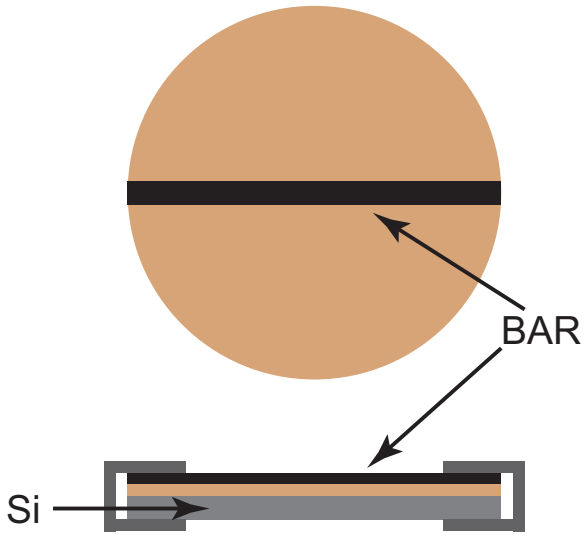

Figure 2.11: Bar method to constrain steel substrate during ZnO deposition.

sputtering, which introduced cracking and deformation due to residual stresses. When a single continuous film of ZnO was sputtered onto a steel substrate, the wafer became severely warped and widespread cracking was observed as seen in Fig. 2.9. In an attempt to address these problems, I incorporated a stencil mask into the process. ZnO was only deposited on the substrate where windows were cut out of the stencil mask, as illustrated in Fig. 2.10. This drastically reduced overall wafer deformation. However, the stencil mask led to localized dimples, seen in Fig. 2.9, that rendered the subsequent lithography impossible. The most successful method was to constrain the wafer with a single bar across the center of the wafer, secured to an underlying Si handle wafer, illustrated in Fig. 2.11. It was possible to constrain the entire wafer to be flat with a single bar, since after ZnO deposition, an unconstrained wafer would warp concave downward. The bar divided the deposited area into two sections, somewhat reducing warping. After depositing the ZnO, I carefully injected a small drop of water under the steel wafer to temporarily bond it to the Si handle wafer. Then I removed the clamp and the wafer remained flat for the duration of the lithography process. It was critical to keep the wafer constrained to be flat, and to perform the lithography and etching as soon as possible after the sputtering deposition, since cracks were more likely to form the longer the wafer sat. As soon as most of the film is removed and only the sensors remain, residual stress was no longer a risk.

Another problem that arose was with the final lithography step for the steel substrate. The first iteration of the process, described in [26] used thick spin-on photoresist, coated on both sides of the wafer. However, problems with photoresist adhesion, pitting, and lateral etching were observed. In an attempt to alleviate these problems in the next round of processing, Hutchinson Technology, Inc., used their own lithography process wherein a laminate photoresist was pressed onto both sides of the wafer in a vacuum. However, this method proved to be mechanically destructive to the sensor devices. Even with several modifications made to the accompanying processes such as chemical cleaning and drying,

the sensors still did not survive the lithography and etching sequence. Therefore, we returned to the method of using thick spin-on photoresist, and focused on perfecting the lithography sequence to avoid the residual moisture that can cause pitting.

Sensor yield was about 85% on the steel wafers, and was reduced to 40% after steel etching and prototype assembly. The main failure mode was cracking of the sensors after assembly. This was likely a result of the forming of a bend radius at the hinge near where the sensors were situated.

These processes addressed in this section are described in more detail in Appendix A.

2.2.3 ZnO Film Characterization

Ref. [26] describes in detail how ZnO sensors were fabricated on a simple Si cantilever for the purpose of estimating piezoelectric coefficients. The cantilever was mechanically excited with an impulse to generate high frequency vibration. The displacement at the tip of the cantilever was measured with a LDV, while measuring the voltage signal from the sensors. Strain was then related to displacement using fundamental beam theory for small deflections. The direct piezoelectric constant e_{31} was estimated using the calculated strain and measured sensor output voltage. Using this technique, the estimated direct piezoelectric constant was e_{31} =.0377 C/m^2. This value was about an order of magnitude smaller than that reported in the literature [38, 35]. Because of this finding, I included several extra tests in the fabrication of the new prototypes, to ensure adequate film characteristics.

I took X-ray diffraction (XRD) measurements to further evaluate the ZnO material properties. The film thickness was between .8 and 1 μm. Fig. 2.12 shows the XRD spectrum of ZnO film deposited on a Si control wafer. The peak orientation measured at 34.4° corresponds to the (002) plane. A rocking curve analysis determined the dispersion of this crystal plane from the desired orientation. A narrow dispersion indicated good piezoelectric film quality, as quantified by the full width at half maximum (FWHM) of the intensity from the rocking curve. The FWHM was 2.5°. FWHM of less than 2° was expected based on previous results with the sputtering equipment used, but literature reports FWHM values for sputtered ZnO films between .9 and 12.47° [42, 43].

Because it was difficult to probe the patterned ZnO films on the steel wafer using XRD, piezoelectric film quality of the steel wafer and Si wafer were correlated using an experimental "tapper" apparatus. The tapper consisted of a probe tip that contained a PZT actuator. The sample rested on a metal platter under, and in contact with, the probe tip. A sinusoidal voltage excited the PZT actuator in the tip, generating a displacement in the material being tested. This displacement in turn generated a charge across the tested material which was measured as a voltage. The output voltage peaked around a resonant frequency. Results tended to vary across the wafer and were dependent on the electrode material used on the sample. While this test was not suitable for extracting actual material properties, it was appropriate for qualitatively comparing samples. The ZnO film on the Si control wafer generated between 40-80 mV, while the ZnO film on the steel process wafer generated between 60-120 mV for the same excitation amplitude. This indicated that the ZnO film on the steel wafer is comparable to the film fabricated on the Si control wafer

that was used for XRD measurements.

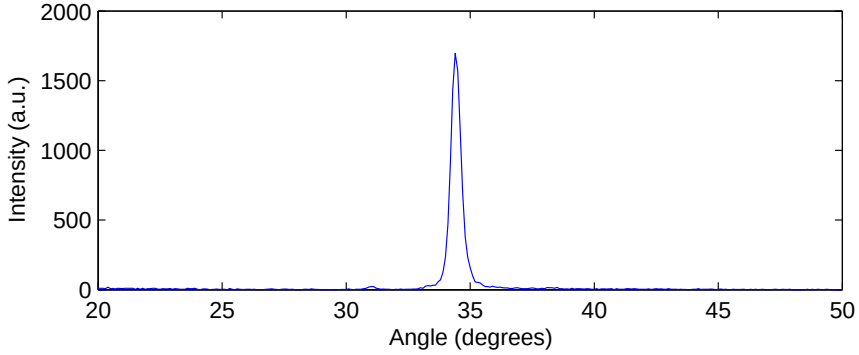

Figure 2.12: X-ray diffraction spectrum for ZnO film deposited on a Si substrate.

Less-than-optimal ZnO film quality was attributed to several factors. First, the sputtering system used to deposit the films was not reaching the target low base pressure. In addition, it was suggested in [26] that parasitic capacitance in the experimental set up reduced the measured piezoelectric constant. However, as will be seen in the following sections, the piezoelectric response was adequate for sensing vibrations.

2.3 PZT Deposition on Steel Substrates

As mentioned above, concerns associated with steel substrates included residual stress, oxidation, roughness, and insulation. It was assumed that PZT thin films would not be viable on a steel substrate due to the high-temperature annealing that is required. I conducted a study to test this claim and explore the possibility of PZT films on steel substrates. If successful, there may be opportunities to use thin-film PZT for actuation purposes as well as sensing on HDD suspensions. I conducted this work at Esashi Laboratory of Tohoku University in Sendai, Japan.

Equipment in this laboratory was outfitted for 2 cm *times* 2 cm substrate. First, round, steel, 35 μm-thick wafers were coated with .5 μm of spin-on-glass and then diced them into 2 cm *times* 2 cm steel substrates. Next, sputtering was used to sequentially deposit 50 nm of Ti, 100 nm of Pt, followed by either 250 or 500 nm of PZT film. The reason I deposited Ti and Pt layers was to mimic a typical electrode stack in a functioning device. The magnetron sputtering process settings for PZT deposition were a gas ratio of 10:7 Ar:O_2, a process pressure of 5 mTorr, RF power of 100W, and temperature of 350^{o}C, resulting in a deposition rate of about 25 nm/min. Typically, a PZT sputtering step is followed by a rapid thermal annealing (RTA) step that reached a maximum temperature of 680 degrees, and then the PZT would be patterned and wet etched. In this study, I compared two process sequences: RTA before etching, and RTA after etching. Results are as follows.

After PZT deposition, the samples with 250 nm films were intact, but the 500 nm films began to crack across the film, as can be seen on the left side of Fig. 2.13. All samples

were warped concave down. The first RTA step caused both substrates to warp upward in the opposite direction as after film deposition, and more cracking occurred on the 500 nm sample. These samples are on the right side of Fig. 2.13. Next, I etched all samples, both with and without RTA, and the results are pictured in Fig. 2.14. The samples that had not been annealed, on the left side of the figure flattened out after etching, but the samples that were annealed prior to etching, maintained the warp that was induced during RTA. The 250 nm samples, both with and without annealing, suffered from some deterioration of the electrode and SOG layers after etching. After etching, I annealed the two samples that had not been annealed yet; these are pictured in Fig. 2.15. Again, the substrates warped upwards. On all samples, I observed severe oxidation on the backside of the wafers, as shown in contrast to a bare, unprocessed steel wafer in Fig. 2.16.

I inspected the test pads under a microscope after processing, and the photographs are shown in Fig. 2.17. On the 250 nm films, test pads of PZT appeared intact, but had a few pin holes. On the 500 nm films, cracking and overetching compromised the overall quality of the test pads, but the thicker films were more uniform and were without pinholes.

To summarize the problems encountered, 500 nm films suffered from cracking immediately after sputtering due to residual stress. The 250 nm films did not crack, but were so thin that pin holes were present. High-temperature RTA caused severe warping and oxidation of the steel wafer, independent of the PZT film. Finally, the wet etch used appeared to attack the Ti/Pt electrode. Performing RTA after the etching process seemed marginally better based on visual quality of the samples, but the micrographs of the films revealed no significant benefit in either case. There are possible solutions to the problems encountered. For example, RTA temperature may be reduced slightly, with the limitation that high temperature and proper ramp rate is required to get the desired piezoelectric crystal structure. Coating the backside of the steel wafer with SOG, and even Ti/Pt, might mitigate warping and oxidation during RTA. Thick films may be achieved by depositing and annealing several thinner layers, or PZT spin-coating may be used. Finally, a dry etch recipe would likely give better etch quality and control, and would not attack the metal electrode. This study was just a first step in investigating the feasibility of PZT thin films on steel substrates. Another caveat is that piezoelectric properties were not evaluated in this study and would need to be verified in future experiments. However, there is now evidence that with extensive process development, deposition of thin layers of PZT that are small in area may be possible on steel.

2.4 Summary

This chapter described the specifics of the design and fabrication of dual-stage instrumented suspensions with thin-film ZnO sensors. Two methods for addressing modal selectivity were used to design sensors that were more sensitive to off-track motion. One method was an algorithm to identify sensor locations that provide the best information for feedback control. The other method was hard-wiring two sensors together to enhance modal selectivity. Micro-scale process were used to fabricate ZnO sensors onto steel suspensions, and subsequently assembly instrumented pieces into full suspension prototypes. Notably,

significant work was done to develop and characterize the deposition and patterning of the ZnO film. Finally, processing experiments were described that began to explore deposition of thin-film PZT onto steel substrates.

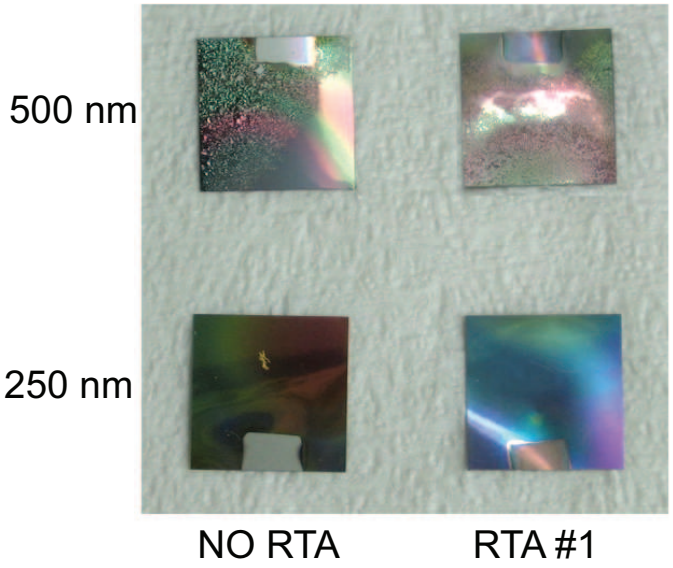

Figure 2.13: Steel samples after Ti/Pt and PZT deposition (left side), followed by rapid thermal annealing (right side).

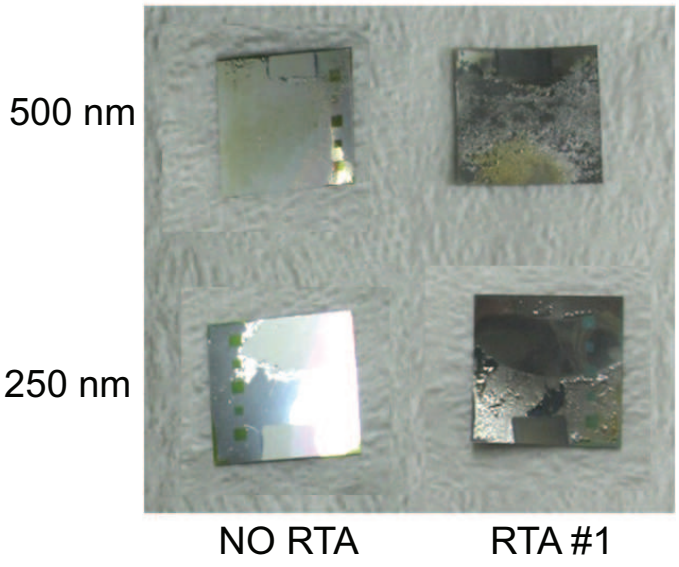

Figure 2.14: Steel samples after wet etching of PZT test pads. The samples on the right have undergone rapid thermal annealing

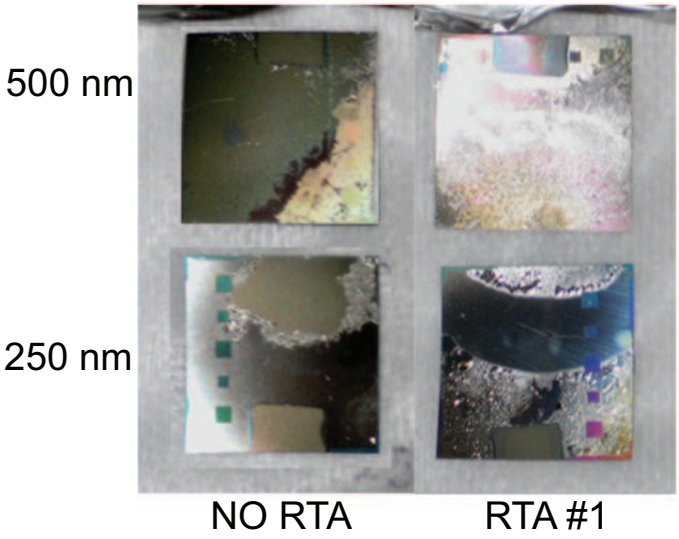

Figure 2.15: Completed samples after rapid thermal annealing the samples on the left side.

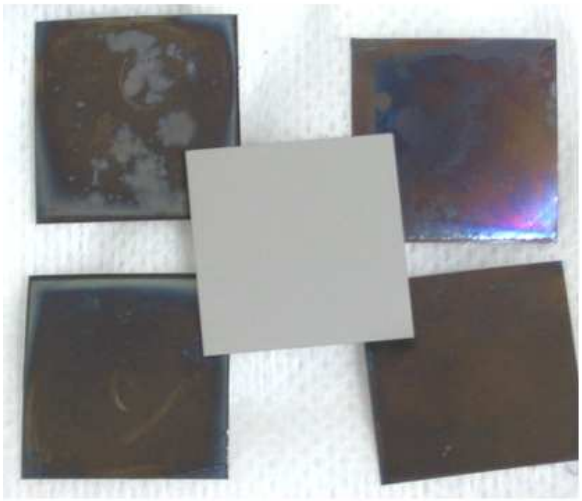

Figure 2.16: Backside oxidation on steel samples, compared to a bare, unprocessed wafer (in the center).

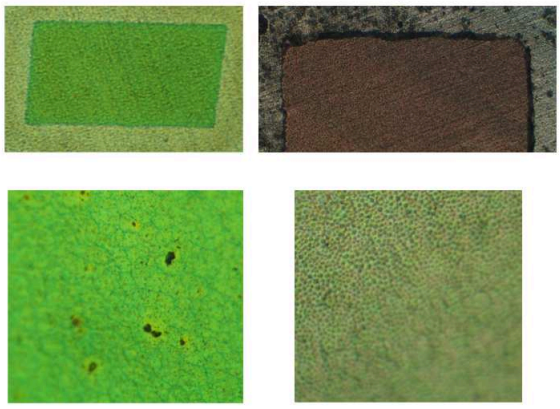

Figure 2.17: Optical micrographs of PZT test pads.

Chapter 3

Prototype Testing

I tested two versions of instrumented suspension prototypes: first-generation prototypes that were fabricated by Stanley Kon, and second-generation dual-stage prototypes that I fabricated. The first-generation prototypes, shown in Fig. 3.1 do not include a dual-stage actuator, and do not incorporate symmetrical interconnected sensing for mode cancelation. I tested these prototypes in open-loop and closed-loop experiments, and the results provided a valuable comparison to the second-generation prototypes, shown in Fig. 3.2. This chapter will describe the open-loop prototype testing results in detail.

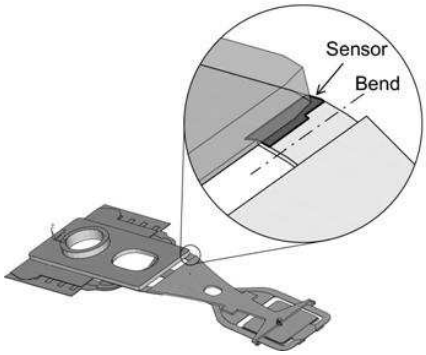

Figure 3.1: Single-stage instrumented suspension prototype. *Image courtesy Stanley Kon.*

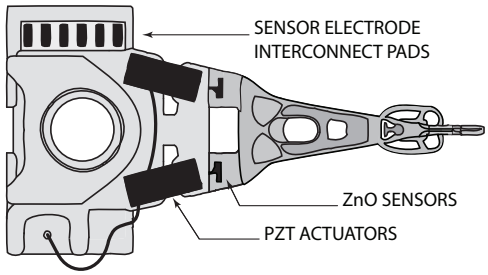

Figure 3.2: Dual-stage instrumented suspension, fabricated as described in this work.

3.1 Experimental Hardware

3.1.1 Amplifier Circuit

Due to both material properties and size scale, the ZnO sensors produced very small currents in response to external strain, on the order of picoamps. Therefore, an appropriate interface circuit was required to condition and amplify the signal. Fig. 3.3 is a diagram

Table 3.1: Circuit component values for interface circuit

COMPONENT	VALUE
C1	2.2 μF
R1	100 Ω
C2	1 μF
R2	2 kΩ
R3	100 Ω
R4	3 kΩ

of the circuit, and Table 3.1 lists the values for the circuit components. The circuit was designed to amplify signals in the frequency range of 1 kHz and 30 kHz where the vibrational modes of interest are found. The circuit was composed of two stages, a buffer stage and a gain stage. The buffer stage utilized a differential input to reduce the common mode noise from both leads with a gain of 100. The relatively large gain was desirable to amplify the signal and increase signal-to-noise ratio (SNR). The second stage was a differential-to-single-end converter with gain of 10, for a total gain of 1000. A high-pass filter was incorporated into the circuit to prevent low-frequency noise and drift from being amplified. The circuit transfer function is as follows:

$$V_s = \left(\frac{sR_4C_2}{1+sR_3C_2}\right)\left(\frac{sC_1(2R_2+R_1)+1}{sC_1R_1+1}\right)[V_2 - V_1], \tag{3.1}$$

where V_s is the output sensing voltage, and V_1 and V_2 are the voltages from the two sensor electrodes. I used this circuit configuration for all prototype instrumented suspensions that I tested.

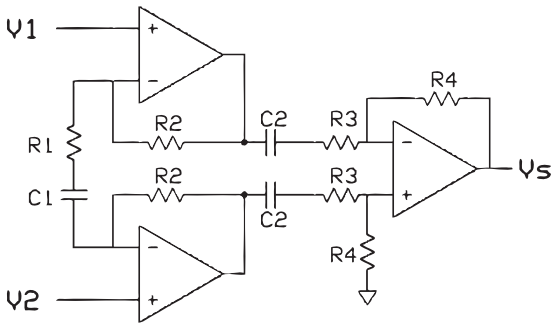

Figure 3.3: Schematic of interface circuit for instrumented suspensions.

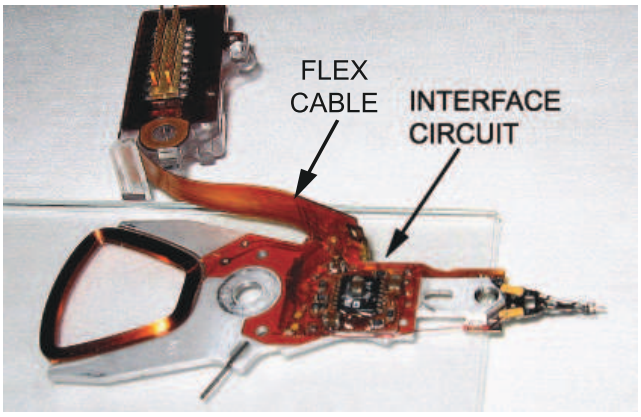

Figure 3.4: The E-block and suspension assembly with interface circuit installed.

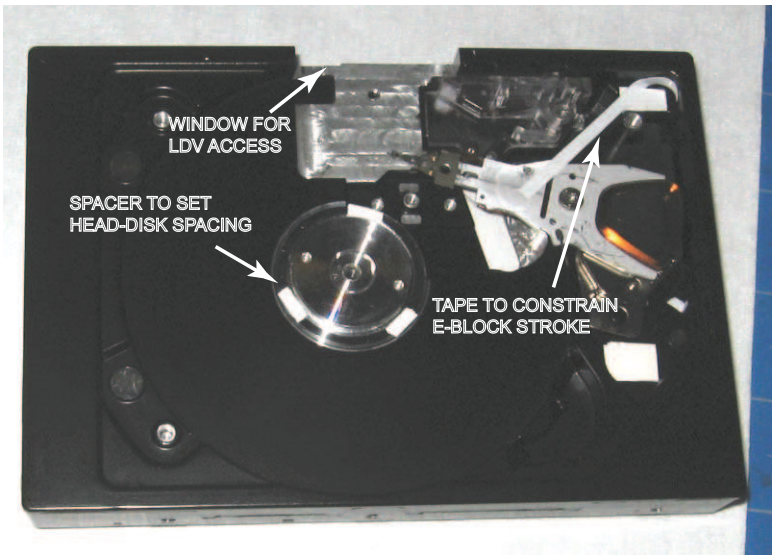

Figure 3.5: Photograph of an opened hard drive showing special features of the experimental set up.

3.1.2 E-Block And Drive Assembly

It was critical to place the circuit close to the sensors to minimize environmental noise and parasitic capacitance. Due to the limited space inside HDDs, I used surface mount components to build the interface circuit directly onto the E-block. Wire-bonded gold connected the components to each other and to interconnects on the E-block that connected to the drive's flex circuit. The flex circuit passed the signals from the sensors to the circuit and from the circuit to pins at the back side of the drive. Next, I potted the entire circuit in clear epoxy to protect the wires and components from damage. Finally, I carefully applied conductive epoxy to connect the sensor electrode pads on the suspension base plate to the lines on the flex cable.

Fig. 3.4 shows the circuit and a prototype suspension installed on a HDD E-block. The entire assembly was placed in an experimental disk drive with one disk platter. We machined a window into the side of the drive to allow access for the LDV, since magnetic servo data could not be accessed via the read/write head in our experimental drives. Based on trial and error, I ensured a conservatively large head-disk spacing to minimize contact and crashing during operation. To prevent the arm from swinging in and crashing into the spindle due to the spring force of the flex cable, I constrained radial location of the E-block using a piece of flexible tape. Fig. 3.5 shows these features of the experimental HDD.

3.2 Windage Characterization

In an early test, I took advantage of the superior resolution of the sensors to characterize the nature of windage disturbance to the suspension. There are different ways to

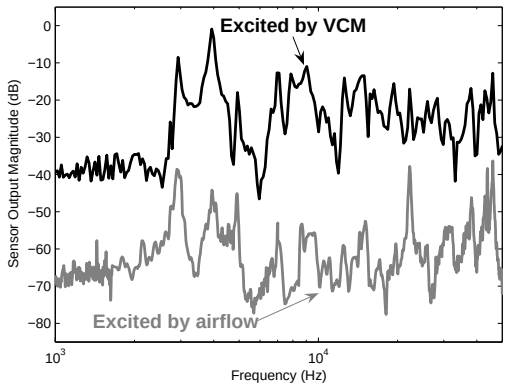

Figure 3.6: Excitation of suspension modes by VCM (top) and airflow (bottom), as measured by thin-film strain sensors.

approximate the windage disturbance when modeling the disk drive servo plant. To simplify modeling, airflow-induced disturbance can be approximated as a white noise input disturbance added to the VCM control input, as in Eq. (3.3),

$$y_m = G_{u,y}(u_v + w), \tag{3.2}$$

where y_m is the measured output, u_v is the VCM input, w is the airflow disturbance, and $G_{u,y}$ is an operator representing the plant model from u to y_m. It is assumed that w is white, Gaussian noise with variance W. However, airflow acts on the suspension directly, not just on the rigid E-block. Therefore certain structural modes may be excited more prominently. Fig. 3.6 shows actual data of suspension modes excited by the VCM and by airflow. The relative magnitudes of the resonant modes are different in the response to airflow compared to the response to VCM excitation. This indicated that certain modes, particularly above 10 kHz, are excited more prominently by airflow. This is consistent with the finite element analysis results observed in [5]. It is therefore more accurate to model the airflow disturbance as

$$y_m = G_{u,y}u_v + G_{w,y}w, \tag{3.3}$$

where $G_{w,y}$ is a model from airflow disturbance to measured output containing the same modes as $G_{u,y}$. The sensor measurement could allow more accurate identification of the elements of $G_{w,y}$.

3.3 Single-Stage Prototypes

A natural questions that arises is whether a single-stage servo system could benefit from additional strain sensing alone. If so, thin-film sensors would be a suitable method of incorporating strain sensing, since it would not alter the dynamics of the suspension. I

attempted to answer this question using the single-stage prototypes. which were configured to utilize the VCM actuation only. Through modeling, simulations, and implementation, I determined that it is difficult to take advantage of high rate strain sensing without dual-stage actuation. The remainder of this section summarizes these studies.

3.3.1 Open-Loop Measurements

The instrumented suspension prototypes used in this experiment were designed to be installed with a 3 mm × 3 mm electrostatic microactuator [27]. However, the purpose of this test was to prove out the use of the sensors on a single-stage suspension, so a functioning microactuator was not used. To simulate the mass of the actuator and obtain the correct flying height, I installed an immobilized dummy microactuator on the gimbal of the experimental suspension.

I obtained open loop transfer functions with the head flying on a spinning disk in an experimental HDD. The E-block was excited by a swept sine input from the VCM. The LDV measured off-track displacement of the slider. The magnitude plots of the transfer functions from VCM to strain sensor and from VCM to LDV are shown in Fig. 3.7. The sensor detected the same modes that appear in the LDV off-track displacement measurement. In addition, the sensor picked up modes that were attributed to non-off-track displacement and repeatable disk-induced disturbances. The strain sensor exhibited good sensitivity, particularly in the high-frequency range.

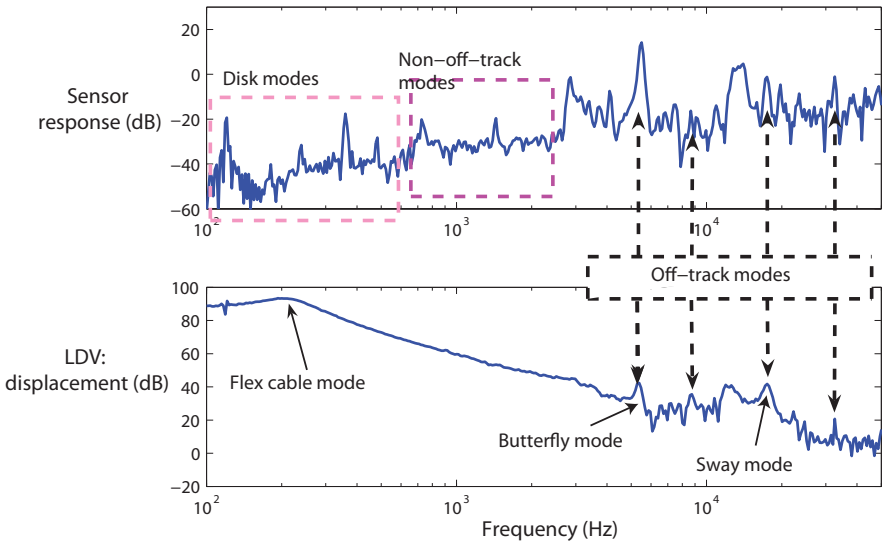

Figure 3.7: Open-loop frequency response magnitudes of single-stage instrumented suspension prototypes, from VCM input to sensor output (top) and to LDV output (bottom).

3.3.2 Modeling

In disk drive system the frequency response from each actuator, u_i, to each displacement sensor, y_j, can be reasonably represented by a summation of second order structural modes, as in

$$G_{ij}(s) = \sum_{n=1}^{N} \frac{\Psi_n^{ij}\omega_n^2}{s^2 + \zeta_n\omega_n s + \omega_n^2}. \tag{3.4}$$

In Eq. (3.4), N is the total number of modes; ω_n and ζ_n are the natural frequency and damping ratio, respectively, of mode n; and Ψ_n^{ij} is the modal constant for mode n from u_i to y_j. The modal parameters, ω_n, ζ_n, and Ψ_n^{ij} can be extracted using a single-degree-of-freedom (SDOF) technique such as the circle-fit method or peak-magnitude method [44]. These methods rely on the assumption that modes are sufficiently separated and lightly damped so that their peaks can be distinguished and their contribution to the total response can be decoupled. I used the peak magnitude method to identify modal parameters from the experimental frequency response data from the instrumented suspension prototypes. For lightly damped modes, the natural frequency approximately equals the resonant frequency,

$$\omega \approx \omega_r. \tag{3.5}$$

The damping ratio can be estimated from the "half-power" frequencies, ω_n and ω_n, at which the magnitude is 3 dB less than the peak magnitude:

$$\zeta \approx \frac{|\omega_a - \omega_b|}{2\omega_r}. \tag{3.6}$$

The modal constant can be estimated by

$$\Psi \approx 2h_r\zeta, \tag{3.7}$$

where h_r is the peak magnitude. For multiple resonant modes, the modal parameters of the largest peak are estimated first. Then the response from this mode is subtracted from the overall response, the process is repeated for the next largest mode, and so on. Finally, the sign of the modal constants were adjusted by trial and error to match the anti-resonances and phase of the frequency response.

The circuit dynamics correspond to the transfer function in Eq. (3.1). A multi-input, multi-output (MIMO) state space model captured the plant dynamics as follows:

$$\begin{aligned} x(k+1) &= A(k)x(k) + B_u(k)u_v(k) + B_w(k)w(k) \\ y_h(k) &= C_h(k)x(k) + \nu_h(k) \\ y_s(k) &= C_s(k)x(k) + \nu_s(k) \end{aligned} \tag{3.8}$$

Here, B_u and B_w are input matrices that separately scale the excitation of modes due to VCM input and windage excitation, respectively. In this way, the windage disturbance model is equivalent to that in Eq. (3.3) The measured outputs are off-track motion, y_h,

and the strain sensor signal, y_s. The measurement noises, ν_h and ν_s are white, Gaussian, and have variance $\mathbb{V}_h$ and $\mathbb{V}_s$ respectively. Models are shown superimposed onto the experimental data in Figs. 3.8 through Fig. 3.9. A number of other modes were neglected in the interest of keeping the order of the controller manageable. Sensor noise was estimated from experiment to be 10 mV RMS. Off track measurement noise was assumed to be 1 nm RMS, which corresponds to typical PES noise of 2% of track width, computed for 1 Tbit/in^2 areal density.

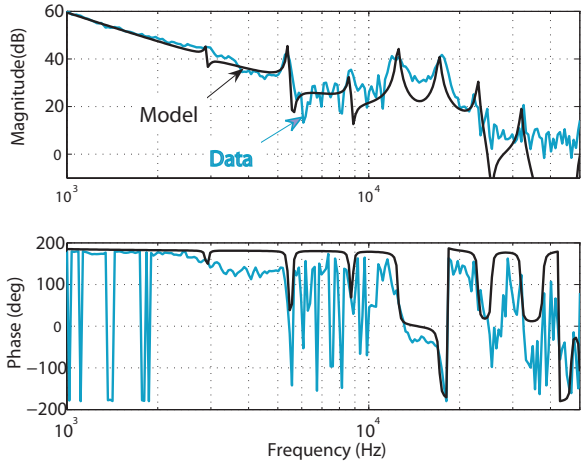

Figure 3.8: Model of transfer function from VCM to LDV on a single-stage instrumented suspension (dark line), superimposed onto experimental data (light line).

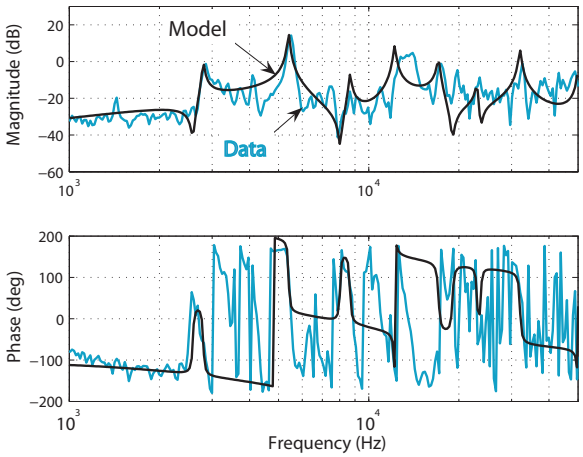

Figure 3.9: Model of transfer function from VCM to sensor on a single-stage instrumented suspension (dark line), superimposed onto experimental data (light line).

3.4 Dual-Stage Prototypes

Fig. 3.10 shows the completed dual-stage instrumented suspension prototype fabricated using the process described in Chapter 2. Among the many designs for dual-stage actuation in HDDs is the PZT-actuated suspension. The typical configuration is to have two pieces of bulk PZT sheet material bonded symmetrically to a portion of the suspension, as seen in Fig. 3.10. Application of oppositely poled voltage to each PZT element induces a yawing motion in the suspension which can be used to cancel off-track disturbances. A disadvantage to this design is that suspension dynamics are altered significantly; the structure is made flexible to achieve adequate stroke. Bulk PZT actuator elements also add complexity to the suspension assembly process. However, the overall simplicity and mechanical robustness has been favorable, and the design has been deployed in commercial prototypes. Therefore, we used this well-established actuation platform in conjunction with the strain sensing methods that we are evaluating in this work to construct experimental hardware. Moreover, auxiliary sensors offered an additional feedback measurement that could be used to damp out the modes caused by the PZT actuator configuration.

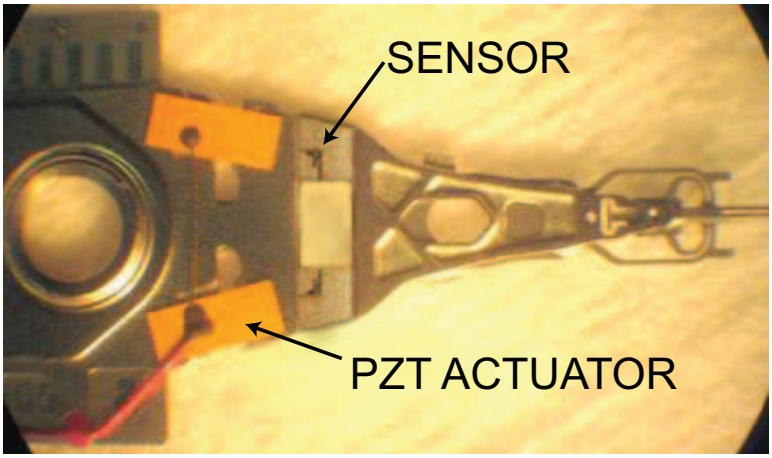

Figure 3.10: Photograph of dual-stage instrumented suspension prototype.

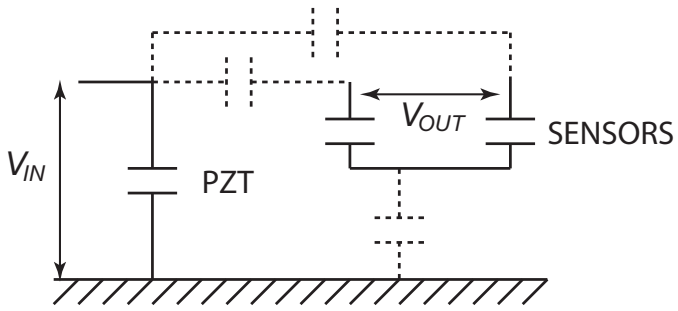

Figure 3.11: Schematic diagram illustrating electrical interactions between the PZT actuators and ZnO sensors due to proximity. Dotted lines indicated capacitance due to air and dielectric material.

The previous chapter discussed the technique of minimizing non-off-track modes, such as the bending mode, by interconnecting symmetrical sensors. This scheme was incorporated into the instrumented suspension prototypes by designing them to have identical sensors on each side of the suspension hinge. Recall that the sensors are hardwired to be interconnected, as shown in Fig. 2.5 so that their signals are subtracted from each other. The common electrode is not grounded, in order to provide an electrical buffer from the driving signal, as illustrated in the schematic in Fig. 3.11.

3.4.1 Open-Loop Measurements

I tested the dual-stage prototypes in the same manner as the single-stage prototypes, with an added input to the PZT actuator. The same circuit configuration amplified the signal. Fig. 3.12 shows the four open-loop transfer functions, from the VCM and PZT, to the LDV and sensors, respectively. Common off-track modes are detected in all four transfer

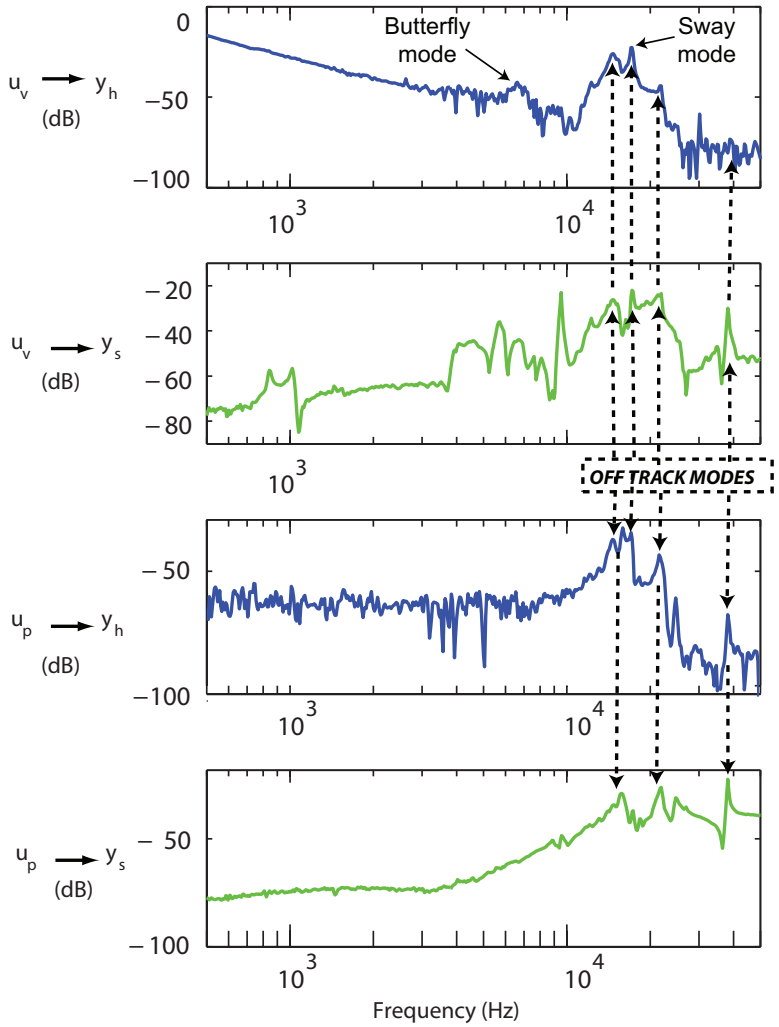

Figure 3.12: Open-loop frequency response magnitudes of dual-stage instrumented suspension prototypes, from VCM input and PZT input to sensor output and to LDV output.

functions. As with the single stage prototypes, the resolution of the sensor measurement is very good throughout the high frequency range. The sensor measurements did not have quite as many peaks as in the single-stage prototypes, indicating that the symmetrical sensors are minimizing some non-off-track modes. However, non-off-track modes still appear in the middle frequency range. Some of these modes may be torsional modes that cannot be fully canceled with symmetrical interconnected sensors. Also, there is likely some mismatch in the two sensors due to process variations such as film thickness and etching that prevented perfect cancelation.

The DC gain of the PZT elements was about 5 nm/V, which I estimated from the frequency response from PZT actuators to the LDV measurement. Again, sensor noise was about 10 mV RMS. One significant characteristic that I observed was feedthrough due to the physical proximity of the PZT actuators and ZnO sensors. This causes the steadily

increasing magnitude in the frequency response from the PZT actuator to the ZnO sensor.

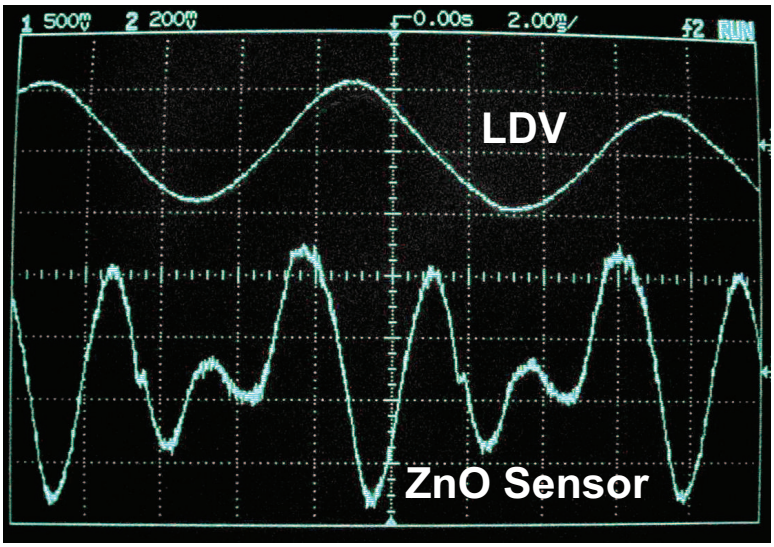

Figure 3.13: Time trace of vibration measurements from LDV (top) and sensors (bottom), showing oscillations at 120 Hz, 240 Hz, and 360 Hz.

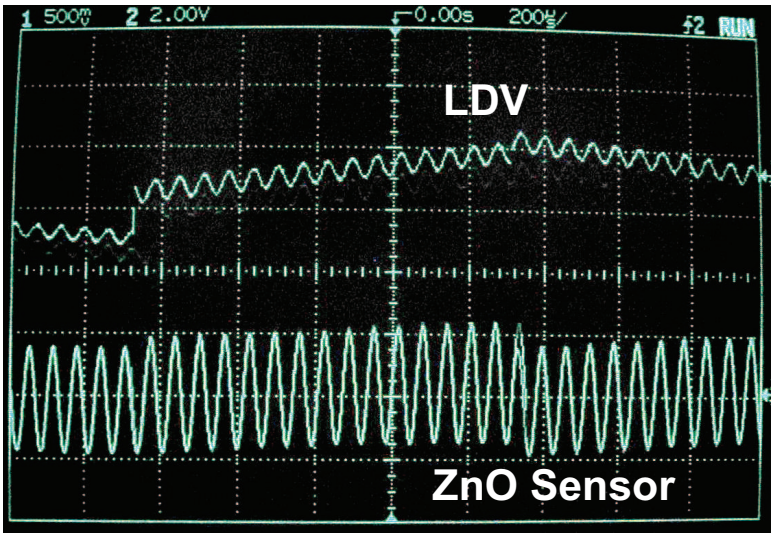

Figure 3.14: Time trace of vibration measurements from LDV (top) and sensors (bottom), near 15000 Hz.

Figs. 3.13 and 3.14 show time traces of the sensor signal and the LDV. Fig. 3.13 shows the response of the sensor and LDV to windage and disk disturbances only, with no actuator input. The large-amplitude oscillation is at about 120 Hz, which corresponds to the disk rotation rate, and also happens to be near the flex-cable (or "rigid body" mode)

at about 130 Hz. The sensor also detects disk modes at 120 Hz and its harmonics at 240 Hz and 360Hz. The sensor signal peak-to peak-amplitude is 800 mV, and the LDV peak-to-peak amplitude is 1 V. (Note that this amplitude corresponds to 2 μm, which is a fairly large drift unique to the experimental setup, with no closed-loop compensation.) Fig. 3.14 shows the response of the sensors and the LDV to a VCM excitation at around 15000 Hz. The sensor peak-to-peak amplitude is about 4 V, while the LDV peak-to-peak amplitude is about 200 mV. It is apparent that the sensor signal is strong around the resonant modes and rivals the LDV measurement in resolution at higher frequencies. With a sensor noise level of only 10 mV RMS, the signal-to-noise ratio (SNR) at resonant frequencies ranges from 25 to over 120.

3.4.2 Modeling

The dual-stage prototype was modeled in a similar state space modal structure as the single-stage prototypes, including both estimated modal parameters, and modeled circuit parameters. The feedthrough effect in the instrumented suspensions was less dramatic than that of self-sensing techniques that will be described in the next chapter. However, since it is caused by parasitic capacitance due to component proximity, it is difficult to model explicitly. I accounted for feedthrough effects by adding extra poles and zeros that I tuned as well as possible to match the observed feedthrough dynamics in the transfer function from the PZT actuators to the ZnO sensors. These feedthrough dynamics were of the form

$$G_{ft} = \frac{(s+\mu_1)(s+\mu_2)}{(s+\rho_1)(s+\rho_2)}. \tag{3.9}$$

Fig. 3.15 shows the model superimposed over the experimental data.

3.4.3 Observations Of Dynamic Characteristics

I evaluated several prototypes throughout the testing process. Comparing the dynamics of several instrumented suspension prototypes provided insight about the performance of the sensors, and of the prototype assemblies themselves. Fig. 3.16 shows the measurements of off-track displacement from VCM excitation and from PZT excitation, respectively, for four different instrumented suspension prototypes. The dynamics of all the assemblies were similar with modes occurring at consistent frequencies and with comparable magnitudes. However, one assembly was installed onto the drive with the read/write head too close to the disk, which altered the dynamics (this assembly eventually crashed). The low-frequency flex-cable mode shifted because it was affected by the strips of tape used to constrain the motion of the E-block, as shown in Fig. 3.5.

Fig. 3.17 shows the sensor response to the VCM excitation for two different instrumented suspensions. One response was measured on the assembly with the read/write head too close to the disk. The second response was measured on a new assembly with a new circuit and a safer head-disk spacing. Because of these differences, the modal dynamics and overall magnitude of the sensor response was different, but quality of the signal was comparable.

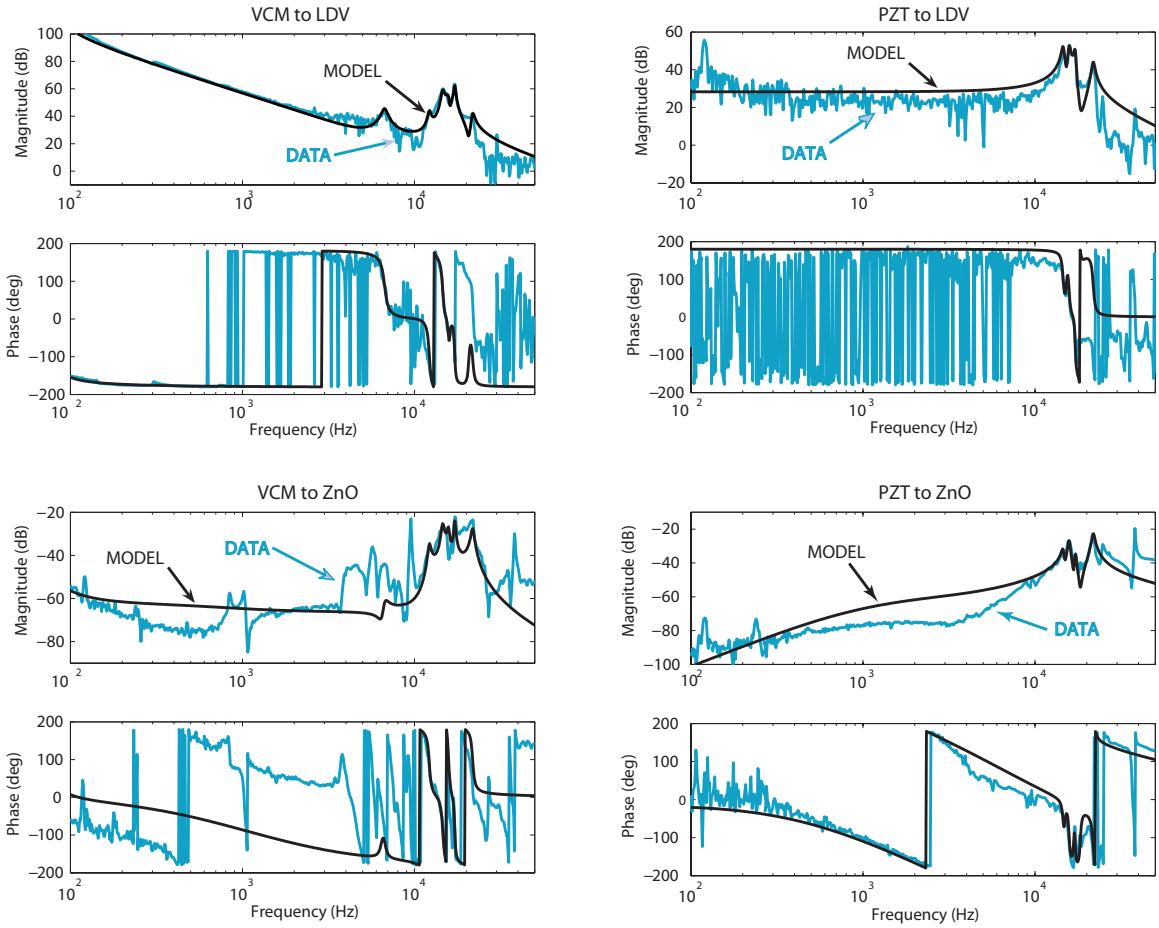

Figure 3.15: Open loop frequency response magnitudes of dual-stage instrumented suspensions, from VCM input and PZT input to sensor output and to LDV output.

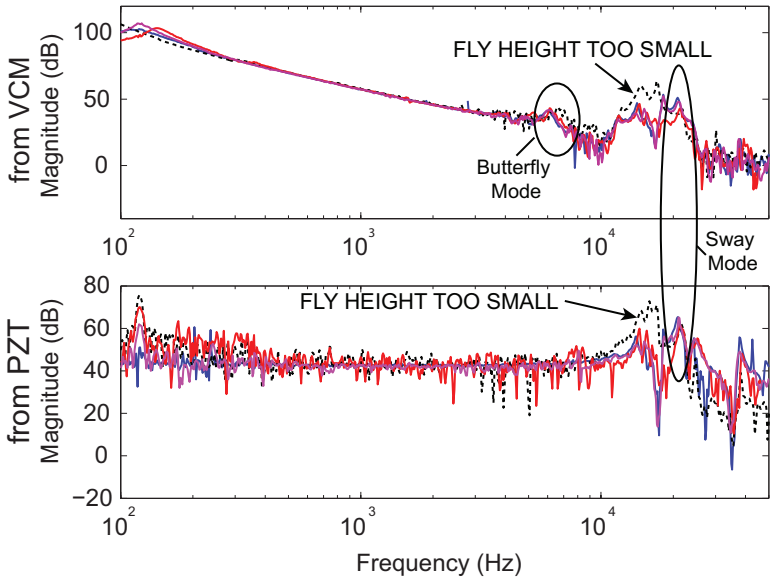

Figure 3.16: Comparison of the off-track motion dynamics of multiple instrumented suspension prototypes.

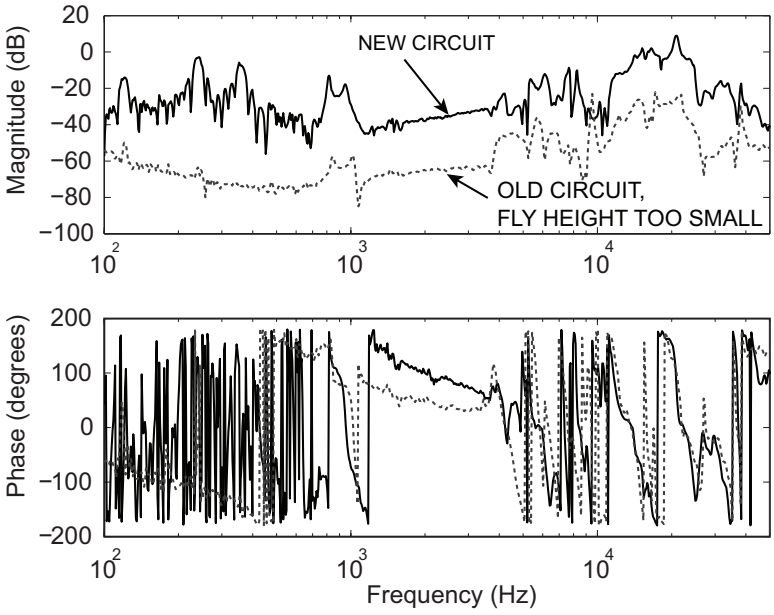

Figure 3.17: Comparison of the sensor response to VCM excitation for several instrumented suspension prototypes.

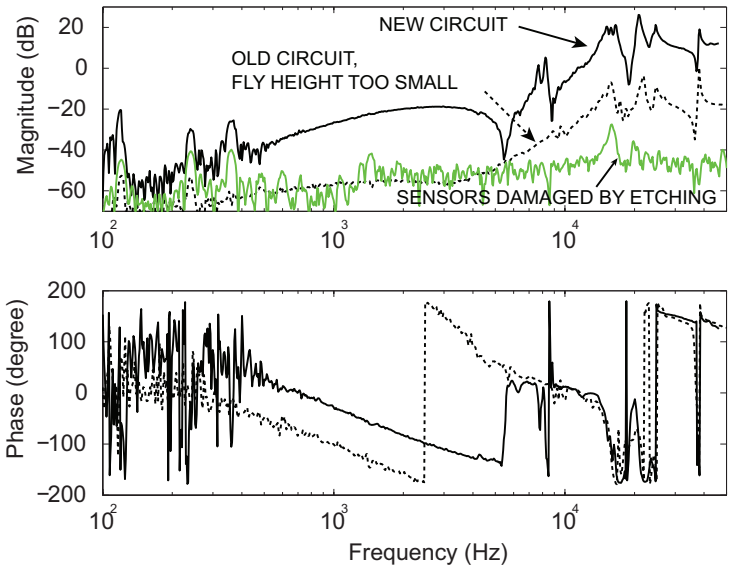

Figure 3.18: Comparison of the sensor response to PZT excitation for several instrumented suspension prototypes.

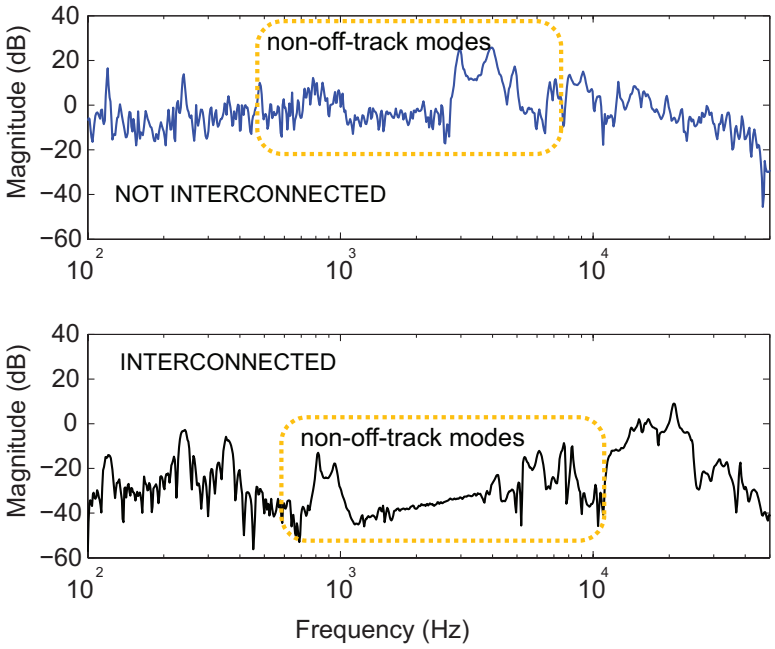

Figure 3.19: Comparison of sensor response to VCM excitation on the first prototype without interconnected sensors and on the second prototype with interconnected sensors.

Fig. 3.18 shows the sensor response to the PZT excitation for the same two suspensions as in Fig. 3.17. As is visible from the phase measurement, the feedthrough characteristics

were similar, but not the same. In addition, there is a measurement from a prototype with sensors whose edges were effected by the steel etching process. It is apparent that the response of these sensors was significantly degraded.

Finally, Fig. 3.19 shows the sensor response to the VCM excitation on the first-generation prototype with no interconnection between the sensors, and the second-generation prototype with interconnected sensors. Both versions picked up a number of non-off-track modes. However, on the second generation prototype, the response of the important off-track modes was higher than the signal from the non-off track modes. This is in contrast to the dynamics of the first-generation prototypes, which were dominated by large non-off-track modes. The signal quality and modal selectivity appeared to have improved marginally in the second-stage prototypes, but not as dramatically as we hoped. This may be because of asymmetry due to variations in processing and assembly.

This ensemble of measurement revealed the irregularities in the dynamics of the instrumented suspension prototypes, compared to those of a typical PZT-actuated HDD shown in Fig. 2.1. The results emphasized that the dynamics were very sensitive to prototype fabrication and assembly, and were not necessarily indicative of a real commercial HDD.

3.5 Summary

This chapter discussed in detail the dynamic testing of instrumented suspension prototypes. First, the experimental set-up and custom miniature instrumentation circuit were described. The subsequent testing included frequency responses from various excitations to displacement and sensor measurement. As a benchmark, testing was performed on early single-stage instrumented suspensions. Dual-stage suspensions demonstrated superior dynamic performance, but still contained some undesirable non-off-track modes in the sensor measurement. On both measurements, the sensors provided high-resolution measurements to allowed realistic characterization and modeling of the system.

Chapter 4

PZT Self-Sensing Actuation

4.1 Introduction

Another sensing solution that has shown promise in HDD applications, referred to as "self-sensing," uses an electronic circuit to extract a sensing signal from a piezoelectric actuator element. The advantage to this approach is that a strain sensing signal can be obtained from a PZT-actuated suspension without integrating additional sensor elements or interconnects, although it relies upon the use of a piezoelectric actuated suspension as the dual-stage configuration. Previously, Li et al. accomplished the same functionality by using one of the elements of a PZT-actuated suspension as a sensor while using the other for actuation [18], and a successful damping controller was implemented. However, disadvantages of this scheme include reduced actuator force and non-off-track modes entering the measurement. It is more desirable to make use of both of the PZT elements because actuator force is doubled, and their symmetrical arrangement can be exploited to minimize sensing signals from non-off-track modes, as described in Chapter 2. Self-sensing uses a bridge circuit to decouple the strain-induced voltage in a piezoelectric element from the actuation voltage across the element, allowing a single piezoelectric element to be used as an actuator and sensor simultaneously. An additional benefit of self-sensing is that sensing and control are collocated, which guarantees stability of a closed-loop vibration control system even when modes exist outside of the controlled bandwidth [45]. Examples of implementation of self-sensing HDDs can be found in [19] and [20]. Self-sensing has also been shown to be useful for nano-scale positioning in such systems as atomic force microscopy [46] [30]. I assembled an experimental drive with a self-sensing suspension of the same design as the instrumented suspensions prototypes, with the PZT elements wired as illustrated in Fig. 4.1. The purpose was twofold: 1) to provide a benchmark to compare to the instrumented suspension prototypes, and evaluate the real benefits of thin-film sensors, and 2) to provide a more simple, robust test bed for proving out control strategies that was not contingent on the completion of second generation instrumented suspension prototypes. This chapter gives an overview of the self-sensing technique, and then describes the assembly and testing of a benchmark self-sensing testbed.

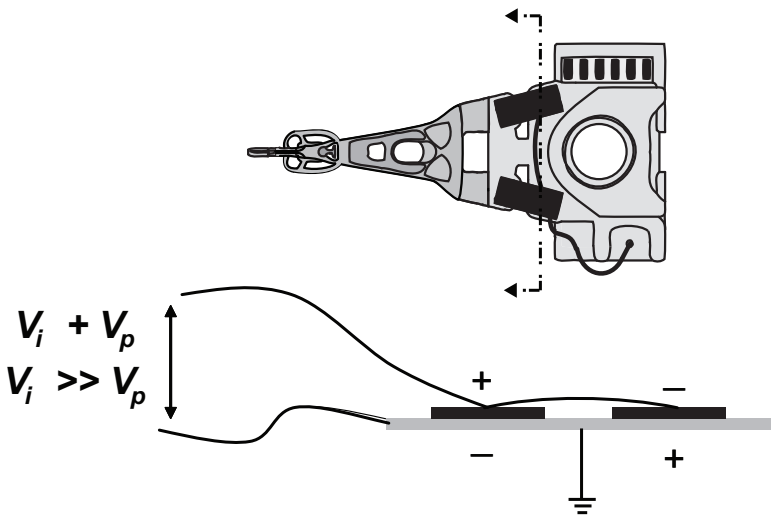

Figure 4.1: Schematic view of PZT-actuated suspension wired for self-sensing.

4.2 Review Of Self-Sensing

The voltage induced across a piezoelectric element as a result of the mechanical response is typically orders of magnitude smaller than the actuation voltage that would be applied to create displacement in the same element. Self-sensing is based on the idea that if the impedance of the piezoelectric element is known, the same actuation voltage can be applied to an equivalent impedance. Then this electrical response can be subtracted from the voltage across the piezoelectric element and the residual signal is the mechanical response.

The scalar constitutive equation describing the electrical response of a piezoelectric material is given by,

$$D_i = e_{ij} S_j + \epsilon_{ik} E_k \tag{4.1}$$

where D_i is electrical displacement in the i direction, e_{ij} is the strain piezoelectric constant, S_j is the mechanical strain in the j direction, ϵ_{ik} is the permittivity constant, and E_k is the electric field applied in the k direction. But $D_i = Q_i/A_i$ and $E_k = V_k/t_k$, where Q_i, A_i, V_k , and t_k are the charge, electrode area, voltage and sensor thickness, respectively. Substituting these into Eq. (4.1), the term $D_i = \epsilon_{ik} E_k$ can be rewritten as

$$Q_i = (\frac{A_i \epsilon_{ik}}{t_k}) V_k = C_k V_k \tag{4.2}$$

which is nothing more than a simple capacitor equation, with capacitance, C_k. The PZT element can then be reasonably modeled as a capacitance in series with a voltage source, V_p, that results from the mechanical-electrical coupling corresponding to the term $e_{ij} S_j$ in Eq. (4.1). Therefore, practical self-sensing circuits are typically designed to balance only a capacitance. A more realistic model includes a resistor in parallel with the capacitor to represent leakage current, since the material will not behave like an ideal capacitor and will have some losses.

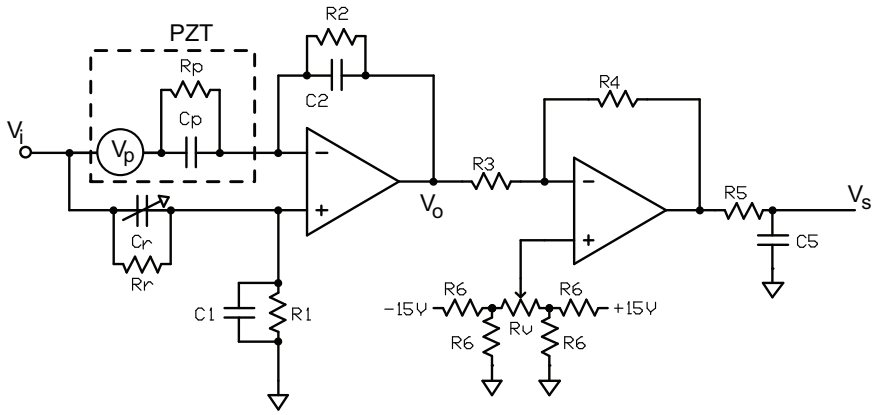

Figure 4.2: Self-sensing circuit for a PZT-actuated suspension.

4.3 Circuit Design

There are two general classes of self-sensing circuits, depending on whether a strain measurement or a strain rate measurement is required. We chose a circuit design that measures strain for the purpose of vibration control because it relates directly to displacement and the PES measurement. Fig. 4.2 shows the self-sensing circuit designed for use with the PZT-actuated suspension. The driving voltage for actuating the PZT is V_i, V_p is the strain-induced voltage across the PZT, V_o is the output voltage from the bridge stage, and V_s is the final circuit output, which is the sensing signal. The first stage is the bridge stage, and it includes an operational amplifier in a differential configuration with four branches. One branch contains the PZT element. A reference branch contains a capacitor matching the capacitance of the PZT, and a resistor in parallel to balance the leakage losses of the PZT. Branches with components labeled 1 and 2 complete the bridge portion of the circuit. Their capacitance and resistance values should match, and the values are chosen to set the frequency range over which the circuit response is linear. The second stage of the circuit provides additional amplification of the residual strain signal, and includes an variable voltage offset to remove any bias from the circuit output. A low pass filter was added to the circuit to remove high frequency noise that can originate either externally or from the operational amplifiers.

Table 4.1: Circuit component values for self-sensing circuit

COMPONENT	VALUE
C_R	1.31 nF
R_R	9.9 MΩ
C_1, C_2	1 nF
R_1, R_2	10 MΩ
R_3	1 kΩ
R_4	100 kΩ
R_5	1 kΩ
C_5	3 pF
R_6	2.1 kΩ

4.4 Circuit Tuning And Mismatch

The transfer function for the circuit shown in Fig. 4.2 is

$$V_o = \left(\frac{R_1(R_rC_rs+1)[R_pR_2(C_p+C_2)s+(R_p+R_2)]-R_2(R_pC_ps+1)[R_rR_1(C_r+C_1)s+(R_r+R_1)]}{R_p(R_2C_2s+1)[R_rR_1(C_r+C_1)s+(R_r+R_1)]}\right)V_i + \left(\frac{R_2(R_pC_ps+1)}{R_p(R_2C_2s+1)}\right)V_p \quad (4.3)$$

If the components C_r, R_r, C_1, R_1, C_2, and R_2 are tuned such than $C_r = C_p$, $R_r = R_p$, $C_1 = C_2$, $R_1 = R_2$, then the numerator in the first term of Eq. (4.3) vanishes. The residual term is proportional to the voltage across the PZT element that is induced from mechanical strain. Mismatch in these components can degrade the quality of the circuit output by failing to cancel the feedthrough from the driving signal, V_i. To study the effect of mismatch on feedthrough, I simulated the transfer function from V_i to V_o with varying mismatch between the components. In this way, I discovered the nature of the mismatch effects, and how best to minimize the distortion in each case. Fig. 4.3 shows several simulation results for values with mismatch ranging from .1% and 1%. Mismatch between C_p and C_r causes the magnitude of the feedthrough to increase throughout the entire frequency range. This is the most critical component to match, and that is why this component needs to be tunable. Mismatch between the bridge resistors, R_1 and R_2, causes low frequency distortion, but these components can be adequately matched by selecting precision off-the-shelf components. Moreover, the frequency range of interest for the HDD sensing application is in the high frequency range, so low frequency distortion is less problematic. Variations in leakage resistance also give rise to low frequency distortion. Unfortunately, this value can vary dramatically during operation, so it is most useful to simply apply a high pass filter to eliminate this effect. Note that the bridge circuit stage already has high-pass filter characteristics, so the bandwidth can be tuned by changing the value of R_1 and R_2. The chosen circuit values are shown in Table 4.1.

Since I wanted to measure strain, the circuit produced an output that was proportional to the voltage across the piezoelectric element. It was necessary to explicitly tune the capacitance across the reference branch to match the capacitance of the PZT element. There

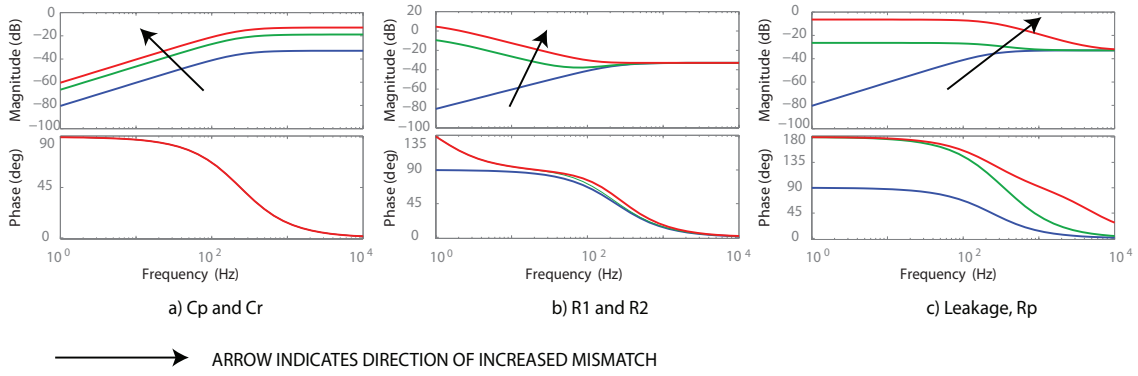

Figure 4.3: Effects of mismatch in self-sensing circuit components on driving voltage feedthrough.

are two types of variable capacitance components that can be used in an instrumentation circuit. One is a "trimmer" capacitor, which is tuned manually. The mechanism for tuning mechanically alters the dielectric layer in the capacitor, changing the resistance. This is a simple way to tune capacitance, but is not always adequately stable when subject to environmental variations. The other type is called a varicap, which is a voltage variable capacitor that can allow automated tuning of the capacitor. I used a trimmer capacitor and found it to be adequately stable during operation, and drift from temperature variations were not observed.

Note that if strain *rate* is measured, the output is proportional to the *current* across the piezoelectric element. In this case, it is possible to configure the reference branch so that the effective capacitance can be tuned with a variable resister, multiplier, or other type of voltage divider, as in [30], [47]. These schemes are simple and easy to control accurately and digitally, but rely on one side of the capacitance being at ground, or zero voltage.

4.5 Open-Loop Measurements

After tuning the circuit, I installed the suspension wired for self-sensing into an experimental HDD, similar to the set up described in Chapter 3. Fig. 4.4 shows the four frequency responses, from the VCM and the PZT actuator, to the LDV and the self-sensing measurement, respectively. Common off-track modes appeared throughout all the measurements, as highlighted in the figure. The PZT sensing also detected a number of non-off-track modes in the mid-frequency range that are excited by the VCM. This was similar to what I observed with the ZnO sensing prototypes. The effect of feedthrough was apparent in the transfer function from the PZT to the PZT self-sensing signal, especially in the low-frequency range. But the circuit was properly tuned to detect high-frequency modes with good resolution.

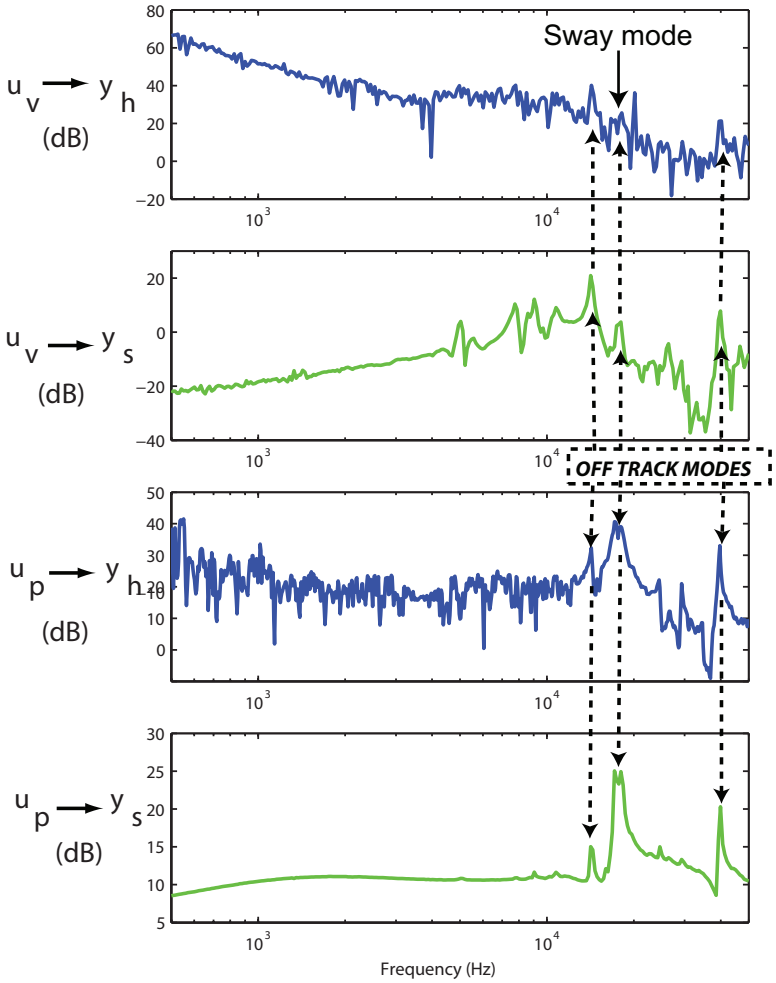

Figure 4.4: Open-loop frequency response magnitudes of self-sensing PZT-actuated suspension, from VCM input and PZT input to PZT sensing output and to LDV output.

I compared the dynamics measured from the self-sensing suspension to the dynamics of the ZnO-instrumented suspension. Recall that the dual-stage instrumented suspension was based on the same suspension design as the suspension used for these self-sensing trials. Fig. 4.5 show the dynamics of the self-sensing suspension and an instrumented suspension in response to the VCM input and the PZT input respectively. The high-frequency modes are notably different. In the self-sensing suspension, the sway mode is much stronger than, and more distinct from, surrounding modes, as compared to the instrumented suspension. This is most likely due to the undercutting that occurred during steel etching on the instrumented suspensions, as well as assembly differences. Fig. 4.6 shows the sensor response to VCM excitation for the self-sensing suspension and an instrumented suspension. The self-sensing signal is stronger and demonstrates slightly better modal selectivity. Fig. 4.7 shows the sensor response to PZT excitation for the self-sensing suspension and an instrumented suspension. Again, the self-sensing signal is stronger but contains a more dramatic

feedthrough effect. This may, in fact, be favorable, since the feedthrough seems to drown out non-off-track modes, while retaining prominent off-track modes.

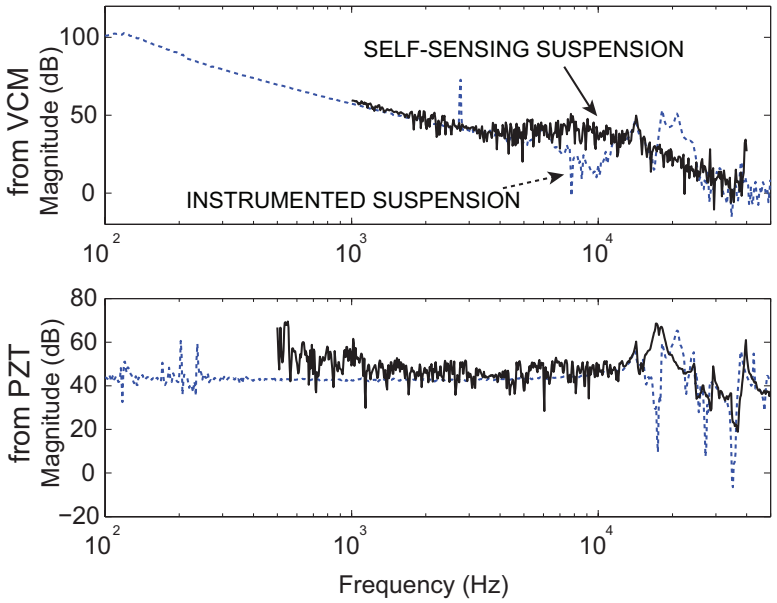

Figure 4.5: Comparison of the dynamics of a self-sensing suspension and an instrumented suspension.

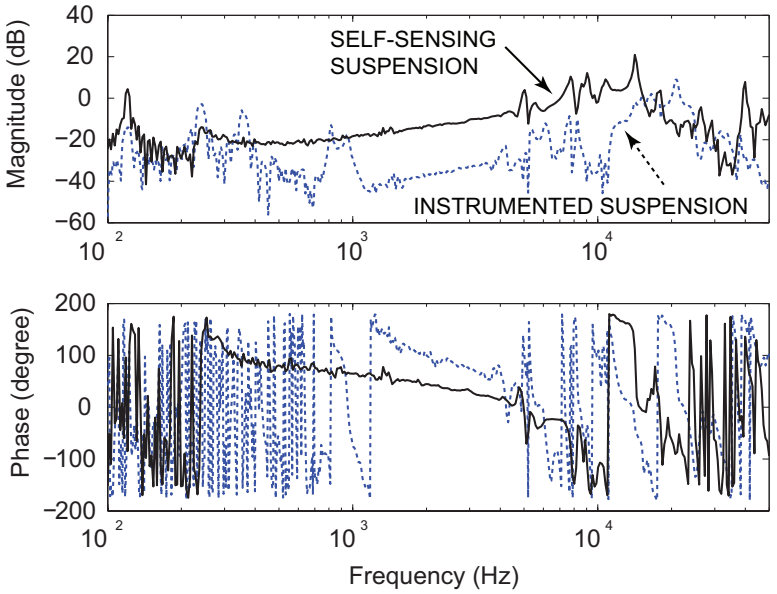

Figure 4.6: Comparison of the sensor response to VCM excitation on a self-sensing suspension and an instrumented suspension.

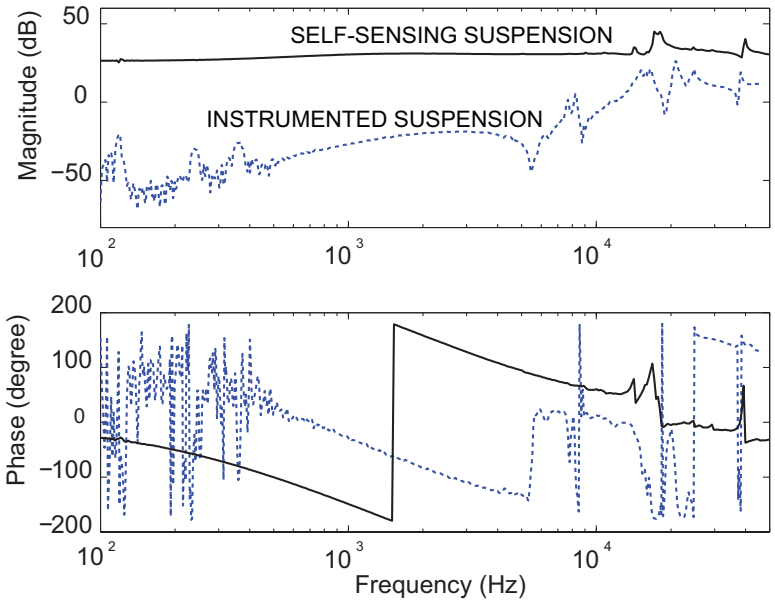

Figure 4.7: Comparison of the sensor response to PZT excitation on a self-sensing suspension and an instrumented suspension.

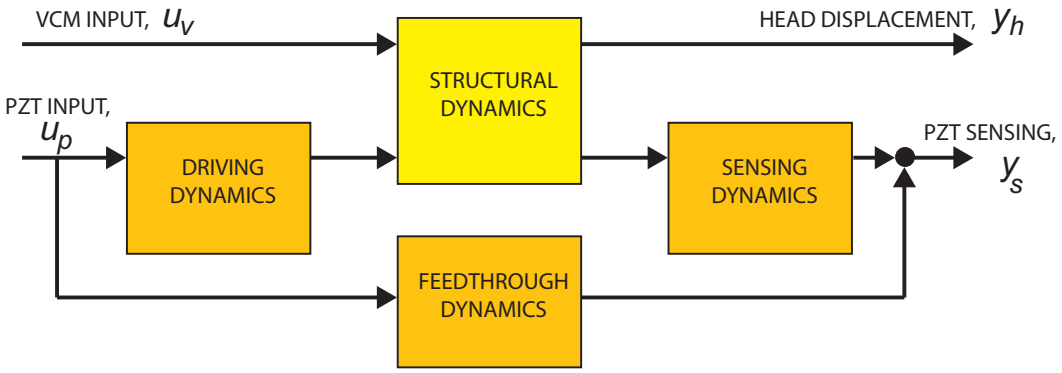

Figure 4.8: Block diagram describing the dynamics of the self-sensing system.

System identification was the next step. Since circuit dynamics affected both the driving and sensing signal, the overall plant was broken down into several sub-plants, as shown in Fig. 4.8. I identified each set of dynamics sequentially as follows. First, I obtained the structural dynamics from the VCM to LDV frequency response, using the peak-magnitude method for identification of modal parameters. Next, with the known structural dynamics, I identified the sensing dynamics from the VCM to PZT frequency response. Similarly, I identified the driving dynamics from the PZT to LDV transfer function. Finally, using the known structural, sensing, and driving dynamics, I identified the feedthrough dynamics from the PZT to PZT transfer function. Identification of all circuit dynamics, includ-

ing feedthrough, was based on the theoretical transfer function given in Eq. (4.3). The model order was minimized by using common eigenvalues for the vibration modes that were repeated in multiple transfer functions. Also, there were only two common poles that occurred in all of the circuit-related dynamics. The identified models are shown in Fig. 4.9, superimposed on the experimental frequency response data.

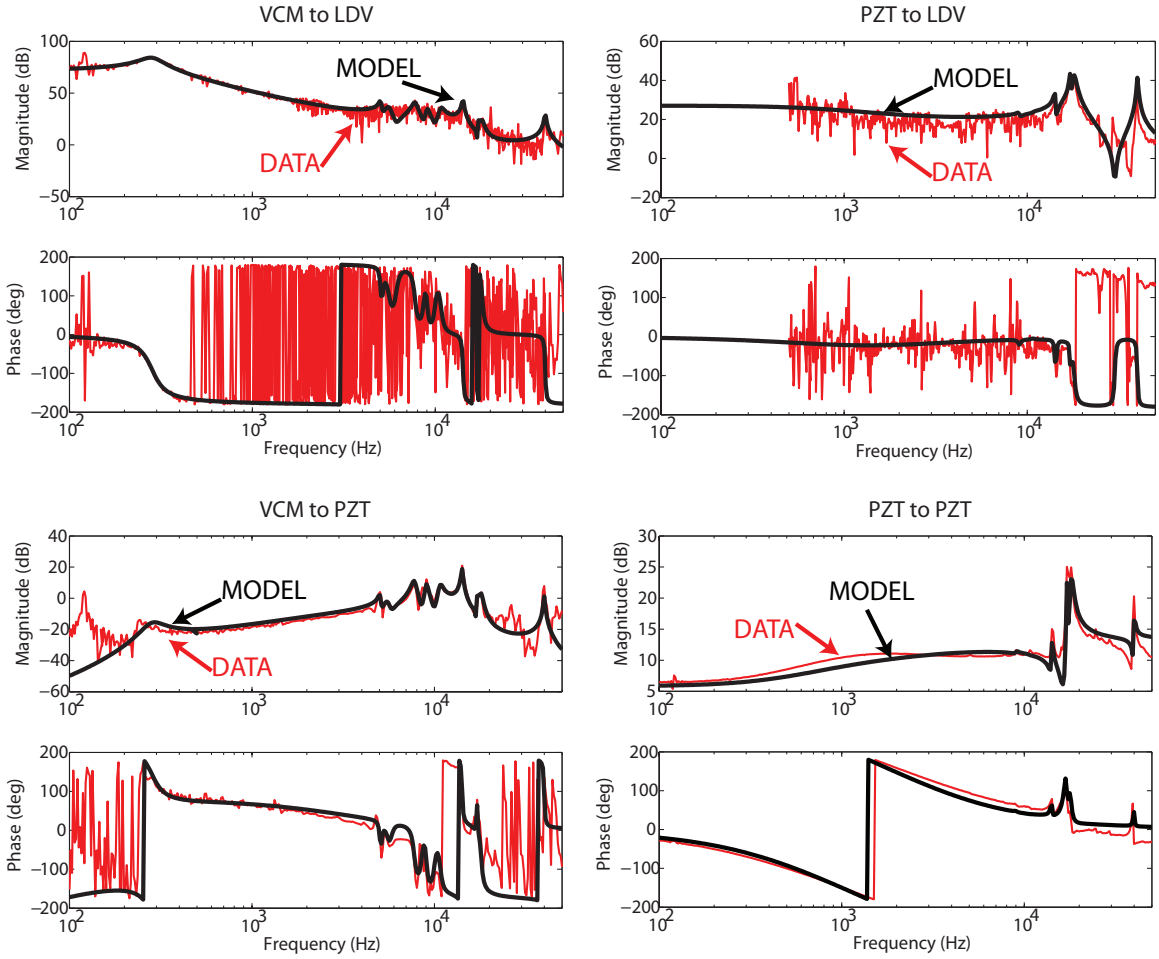

Figure 4.9: Open loop frequency response magnitudes of self-sensing PZT-actuated suspensions, from VCM input and PZT input to sensor output and to LDV output.

4.6 Comparison Of Sensing Methods

Working with the self-sensing suspension yielded some important insights about strain sensing on suspensions, and the relative merits of thin-film sensing. With thin-film sensing, the sensor design is decoupled from the actuator design, and sensor location, shape, and configuration can be optimized accordingly. Self-sensing constrains the sensors to be the same configuration as the actuators. This can be limiting for sensor design, but it has the

Table 4.2: Comparison of Separate Thin-Film Sensors and Self-sensing Actuators

	Thin-film sensors with separate actuator	Self-sensing actuator
Flexible design	Yes	No
Affect dynamics	No	Yes
Easy to fabricate	No	Yes
Compatible with suspension fabrication	Yes	Possibly
Mode cancelation	Yes	Yes
Collocated sensing and actuation	Nearly	Yes
Extra external leads	Yes	No
Signal distortion	Moderate	Large

benefit of collocated sensing and actuation. As far as fabrication, thin-film sensors have the potential to be compatible with suspension fabrication that uses similar additive and subtractive processes. However, sensor yield is sensitive to process parameters and subsequent fabrication steps. Depending on the actuator used, self-sensing can be much more physically robust, although larger bulk piezoelectric elements add complicated assembly steps and can significantly alter suspension dynamics. Self-sensing has the advantage of requiring fewer external electrical leads, since the same electrodes are used for both actuation and sensing. Regarding modal selectivity, thin-film sensing can be configured to interconnect symmetrical sensors and cancel some non-off-track modes. Again, self-sensing depends on the actuation configuration, but as long as two symmetrical actuators elements are used, it will also be able to incorporate mode cancelation.

The dynamics of the two sensing schemes were comparable. Both sensing schemes demonstrated excellent resolution in the high frequency range of interest. Both detected some non-off-track modes in the mid frequency range when excited by the VCM. Finally, both thin-film sensors and self-sensing experienced electrical feedthrough effects. Feedthrough is a known issue with self-sensing, even with accurate tuning, and it can be modeled analytically based on the designed circuit. We discovered that the thin-film sensors in our configuration also experience feedthrough because of their proximity to the larger actuators. However, this effect was more difficult to model because the feedthrough signal was transmitted through unknown parasitic capacitances. This effect might be eliminated with a smaller actuator that situated is farther from the sensors and closer to the read/write head. Although it should be noted that in the self-sensing dynamics, the feedthrough appears to have some benefit, drowning out non-off-track modes and emphasizing off-track suspension modes. Table 4.2 summarizes the comparison between thin-film piezoelectric sensing and self-sensing.

4.7 Summary

This chapter discussed self-sensing PZT actuation, which has been studied before in HDDs and may be considered a competitive alternative to instrumented suspensions. After reviewing self-sensing concepts, circuit design and tuning were described in detail. A self-sensing test bed was fabricated and tested in a similar manner to the instrumented suspension prototypes, allowing a critical comparison of the two methods. The two sensing techniques are, in fact, fairly comparable, each with some advantages and disadvantages.

Chapter 5

Closed-Loop Control

Numerous types of control strategies have been applied to the HDD servo system, including classical single-input-single-output (SISO) methods, modern multi-input-multi-output (MIMO) synthesis, neural networks, and adaptive control. Choosing an appropriate control framework depends on the performance objectives, the hardware characteristics, the nature of the plant dynamics and disturbances, and the computational complexity of controller design and/or implementation. The dual-stage, multi-sensing HDD system implied by the hardware developed in this paper has several characteristics that motivate the selection of the control system. First and foremost, the close-loop system is subject to extremely aggressive performance demands. At the same time, HDDs are a mass produced product, resulting in slight variations from drive to drive. Thus, robustness is a required feature of any servo control system. Incorporation of additional actuators and sensors leads to a MIMO system. Moreover, the sensors may operate at different rates. Simple SISO approaches can be powerful because they are relatively easy and intuitive to design, but they may not obtain the best performance possible because they ignore coupling in the MIMO system. For multi-rate MIMO systems, [48] showed that modern multi-rate MIMO synthesis approaches result in better tracking performance and robustness than simpler SISO-based methods. While these MIMO methods can be somewhat computationally intensive, Conway has developed more efficient algorithms showing promise[49, 50]. But since optimal performance is still the highest priority, we also looked to adaptive approaches that can regain some of the performance lost by robust control design. Specifically, I explored an adaptive controller based on a minimum variance objective to reduce off-track motion.

This chapter contains three studies relevant to implementing feedback control using auxiliary strain sensing. First, a simulation study using the nominal plant and optimal H_2 control design gave a comparison of best case performance when strain sensing is added at different rates. Next, strain sensing was used experimentally in a simple damping controller, which could be operated at an arbitrarily high rate, and could allow the controller bandwidth to be increased while still satisfying robustness margins. Finally, an advanced adaptive control scheme was proposed and developed, with simulations that demonstrate the potential of such an approach.

5.1 Optimal Closed-Loop Simulations

The most significant advantage of adding auxiliary strain sensing is the ability to detect position error at a faster rate than the PES. I employed multi-rate, constrained H_2 design to evaluate the potential benefits of high-rate strain sensing in a multi-sensor, dual-stage framework. The objective of this study was to evaluate the performance with varying sampling times in the context of closed-loop control. Therefore, I used a nominal control design to avoid the introduction of weighting functions and additional design parameters that would skew the comparison. Reference [49] described a new computationally efficient, iterative quasi-Newton algorithm for synthesizing multi-rate, constrained nominal H_2 controllers. Consider the diagram in Fig. 5.1, which is in the form of a linear fractional transformation [51]. In this diagram, y is a vector of measurements used for feedback control, u is a vector of control inputs, d is a vector of stochastic disturbance inputs such as windage and measurement noise, z_1 is a vector of signals we would like to make as small as possible, such as the PES, and z_2 is a vector of signals that have specific limits, such as the actuator control signal. The algorithm in [49] solves the constrained minimization problem,

$$\begin{aligned} &\min_{K_{H2}} \|\mathbb{M}_1\|_2^2 \\ &\text{subject to} \|\mathbb{M}_2\|_2^2 < \gamma \end{aligned} \tag{5.1}$$

where K_{H2} is the linear, observer-based state space controller to be designed. $\mathbb{M}_1$ and $\mathbb{M}_2$ are the closed-loop mappings from d to z_1 and from d to z_2, respectively, and γ is a vector that imposes constraints on the elements of z_2. In other words, for our problem, the optimization directly minimized the PES variance while constraining the control inputs to be less than given voltage levels, rather than minimizing a weighted sum of the PES and control inputs, as in the conventional unconstrained H_2 problem.

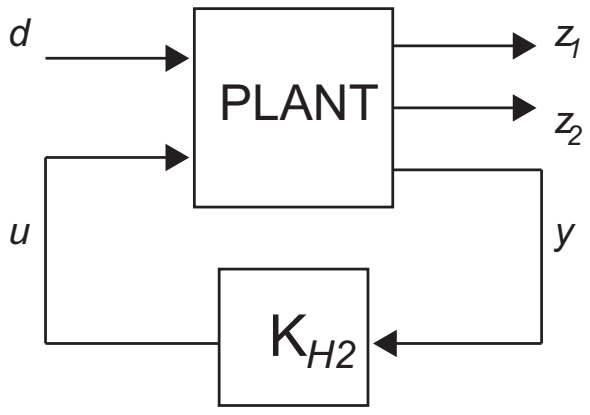

Figure 5.1: Block diagram of the plant to be controlled and the optimal H_2 controller, represented by a linear fractional transformation.

To handle the multi-rate sensing, a lifting technique was used to transform the periodic

time varying system into a linear time invariant system. Consider a general linear periodic time varying, discrete time system, G_{LPTV}. Define N_P as the period of the discrete time system given in number of sample times. For example, if the strain sensors and actuators are operated at four times the rate of the PES signal, than the period of G_{LPTV}, $N_P = 4$.

$$\begin{aligned} x_P(k+1) &= A_P(k)x_P(k) + B_P(k)u(k) && (5.2)\\ y_P(k) &= C_P(k)x_P(k) + D_P(k)u(k). && (5.3) \end{aligned}$$

In this system, $x_P \in \mathbb{R}^{n_x}$, $u \in \mathbb{R}^m$, and $y_P \in \mathbb{R}^{n_y}$. Define the matrix, $\mathbb{Z} \in \mathbb{R}^{N_p \times n_x}$,

$$\mathbb{Z} = \begin{bmatrix} 0 & I_{n_x} & & 0 \\ & \ddots & \ddots & \\ & & \ddots & I_{n_x} \\ I_{n_x} & & 0 & \end{bmatrix}, \qquad (5.4)$$

in which I_{n_x} is the $n_x \times n_x$ identity matrix, and n_x is the number of states in G_{LPTV}. Construct the block diagonal matrices

$$\begin{aligned} \bar{A} &:= \text{blkdiag}\{A_P(1), \ldots, A_P(N_P)\} && (5.5)\\ \bar{B} &:= \text{blkdiag}\{B_P(1), \ldots, B_P(N_P)\} \\ \bar{C} &:= \text{blkdiag}\{C_P(1), \ldots, C_P(N_P)\} \\ \bar{D} &:= \text{blkdiag}\{D_P(1), \ldots, D_P(N_P)\} \end{aligned}$$

Then the system can be represented by an equivalent linear time invariant (LTI) system, G_{LTI},

$$\begin{aligned} \bar{x}(k+1) &= \mathbb{Z}^T\bar{A}\bar{x}(k) + \mathbb{Z}^T\bar{B}u(k) && (5.6)\\ \bar{y}(k) &= \bar{C}\bar{x}(k) + \bar{D}\bar{u}(k), && (5.7) \end{aligned}$$

with $\bar{x}(k+1) \in \mathbb{R}^{N_P \times n_x}$,$\bar{y}(k+1) \in \mathbb{R}^{N_P \times n_y}$ and $\bar{u}(k) = [u(k - N_p + 1)^T, u(k - N_p + 2)^T, \ldots, u(k)^T]^T$. A LTI controller, such as the one [49], can then be designed. Finally, the designed controller is decomposed into a linear periodic time-varying controller that can be applied to the real system.

For this study, I used the model of the instrumented suspension that was presented in Chapter 3 and shown in Fig. 3.15. The VCM input was limited to 5 V at 3σ and the PZT input was limited to 10 V at 3σ. (Note that the VCM input in our experiments is the voltage input into a conditioning circuit for a current amplifier.) In the simulations, the strain sensing was sampled N times as fast as the PES, where N = 1,2,4, and the PES sample rate was 25 kHz. As a baseline, there was also a simulation that did not use the sensing signals, referred to as "$N = 0$." For consistency in all cases, the continuous time model was discretized at the same fast sampling rate (e.g. 100 kHz), then the sampling and actuation were adjusted to generate the appropriate multi-sampling characteristics. Windage was applied at the fast sample rate. When modeling the discrete-time plant, it was necessary to scale the stochastic windage input by $\frac{1}{\sqrt{T_s}}$, compared to the continuous

Table 5.1: Closed-loop simulation results for dual stage instrumented suspensions

Sensing Rate	**% Reduction in off-track motion variance**	**VCM Input** 3σ (V)	**PZT Input** 3σ (V)
$N = 0$ (PES only)	37%	1.4	10
$N = 1$	46%	1.7	6.0
$N = 2$	52%	2.8	6.7
$N = 4$	59%	4.5	6.7

time model, where T_s is the sampling time [52]. Windage was the only disturbance that I considered, since the spectrum of track runout and disk disturbances are at low enough frequencies to be adequately attenuated with the conventional PES signal. Moreover, our experimental setup did not explicitly measure PES, so accurate characterization and verification of the runout disturbance was not possible. Results are shown in Table 5.1, reported as the percentage reduction in off-track motion variance due to windage. By adding strain sensing at the same rate as the PES, the reduction improved from 37% to 46%, indicating that the improved sensitivity of the strain sensors alone is beneficial. Then, by increasing the sample rate of the strain sensors, windage reduction is further improved to as much as 59%. This improvement is attributed to increasing Nyquist frequency, which is half of the sampling frequency. For example, at 25 kHz, the Nyquist frequency is 12.5 kHz, which is less than some of the resonant modes of the system. But at 100 kHz (N=4), the Nyquist frequency of 50 kHz is beyond the modeled resonant modes. Another observation is that without extra sensors, the PZT actuator saturates. But with auxiliary sensing added at higher and higher rates, the two actuators appear to share the load more evenly. One interpretation is that since near-optimal performance was achieved while not requiring the control signals to be close to their respective saturation limits, the optimal performance level was not sensitive to the values of their limits. In effect, control was "cheaper" when more information was available to the controller. This phenomenon may also be related to distortion around the Nyquist frequency that resulted in more control action around the high frequency modes.

5.2 Closed-Loop Damping Experiments

This section describes experimental implementation of strain sensing for damping control. Damping control can be operated with an arbitrarily high sampling rate, and it is a simple, intuitive controller. It is a powerful technique because if high frequency vibration modes can be damped, then the closed-loop bandwidth of the controller can be increased simply by increasing the loop gain, without violating robustness margins. To illustrate this, Fig. 5.2 shows a simple plant with a peak at high frequency. By considering a constant feedback gain, the reader can visualize how increasing the open loop gain, which shifts the magnitude curve up, increases bandwidth but also pushes the high frequency peak closer to the 0dB crossover. When this peak is close to 0dB, the gain and phase margins are

very small. Sometimes this limitation can be addressed by adding a notch filter in the control loop. But notch filters tend to have low robustness to frequency variations. A better solution would be to implement a more robust damping controller using the second stage actuator, and then design the outer tracking loop with the VCM and the damped plant. Examples of such a scheme are described in [40] and [20].

First, we present the results of an attempt to incorporate damping using strain sensors on the single-stage prototypes. This result emphasized the need to proceed to the dual-stage instrumented prototypes. The following section presents the results of damping experiments with the dual-stage prototypes.

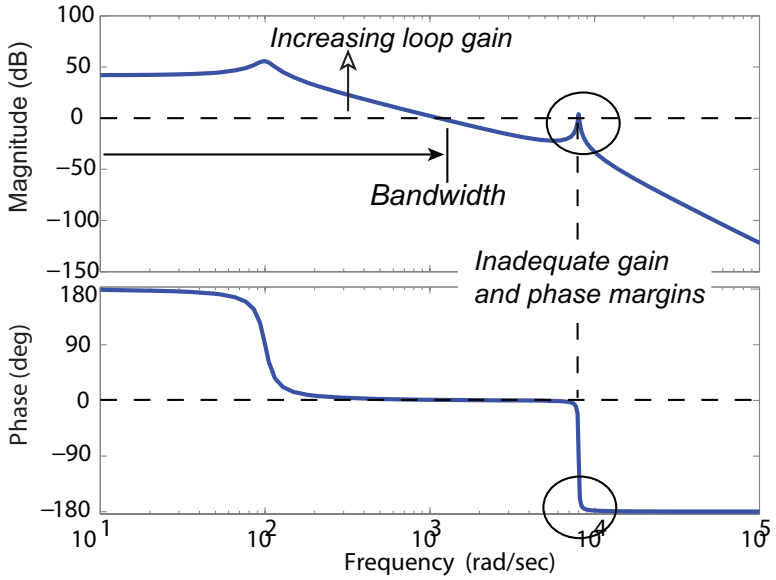

Figure 5.2: Simple example illustrating how a high frequency peak can limit the bandwidth of a system. As the loop gain is increased, the high frequency peak approaches the 0dB crossover, causing inadequate robustness.

5.2.1 Experiments On Single-Stage Prototypes

As mentioned, the first generation prototypes did not incorporate symmetrical interconnected sensors and were very sensitive to many non-off-track modes. However, we attempted to design and implement a closed-loop controller to gain some insight about the feasibility of vibration suppression using added sensing, but no dual-stage actuation. The experimental hardware had been damaged and repaired, resulting in altered dynamics, as seen in the magnitude responses in Fig. 5.3. Non-off-track modes in the sensor signal occurred very close to relevant off-track modes. A new model including non-off-track modes was identified, as described in Section 3

The plant was discretized at a rate of 75 kHz with an input delay of 6 μs. We used frequency-shaped H_2 design to synthesize the robust damping controller. A shaping filter

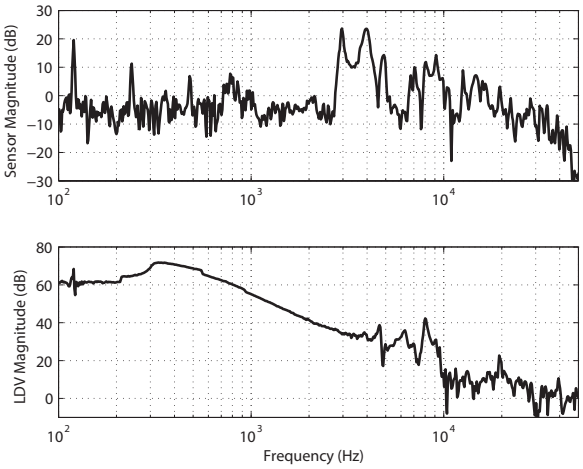

Figure 5.3: Open loop frequency response magnitudes of repaired single-stage instrumented suspension prototypes, from VCM input and PZT input to sensor output and to LDV output.

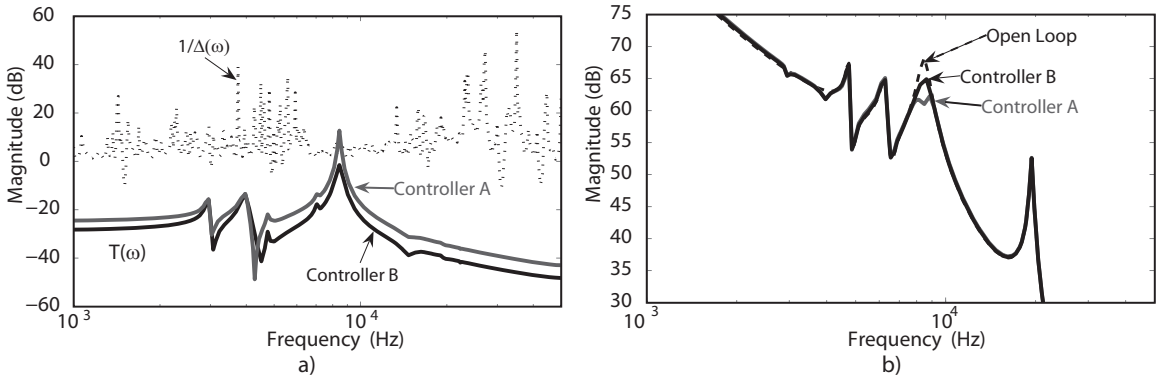

Figure 5.4: Damping control designs for a single-stage instrumented suspension. a) illustrates the robustness margin, and b) shows the closed-loop damping performance, of two possible designs.

on the output performance focused control action onto a narrow band of off-track modes, while a shaping filter on the control input was used to achieve desired robustness. The robustness criteria was given by the condition,

$$\|T(\omega)\Delta(\omega)\|_\infty < 1 \tag{5.8}$$

where $T(\omega)$ is the magnitude of the complimentary sensitivity transfer function, and $\Delta(\omega)$ is the frequency dependent model error [51]. $\Delta(\omega)$ was computed explicitly from the experimental data, and the condition in Eq. (5.8) was checked graphically. I targeted 5 dB

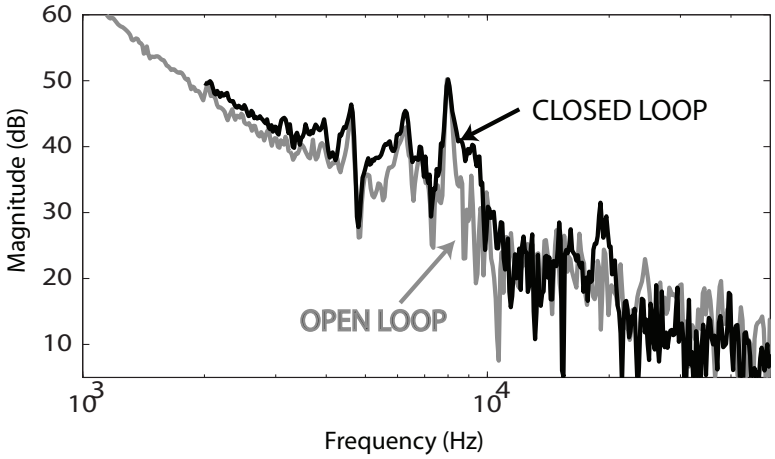

Figure 5.5: Experimental open-loop versus closed-loop measurements for damping control using VCM and sensors.

of gain margin. I performed many iterations on the shaping filters. The robustness margins of two controller designs are shown in Fig. 5.4 a), and the open-loop and closed-loop off-track frequency responses are shown in Fig. 5.4 b). Controller **A** violates robustness requirements, while controller **B** meets the robustness requirements but achieves very little damping of the major off-track modes. Even when I added more states to the model to account for non-off-track modes, I could not achieve better vibration suppression. Because of the many modes in the frequency range of interest, model error remained a limiting factor because of the robustness criteria. Fig. 5.5 shows the implementation results of controller **B**, plotting the open loop and closed loop transfer functions from the VCM to the off-track displacement. As predicted, the modes targeted by the narrow band filters are not suppressed, while other modes appear to be amplified. From this study, it was apparent that there is a fundamental robustness limitation when using the VCM to damp high-frequency modes that are close together. It is especially problematic when there are many non-off-track modes in the sensor signal, adding significant phase uncertainty to the measurement. It is not surprising that these problems were encountered, since the VCM and strain sensors are not collocated.

Without dual-stage actuation, the information obtained from sensing cannot be used effectively due to model uncertainty and phase spillover among high-frequency structural modes. The results emphasized the necessity of cancelation of non-off-track modes, as described in Chapter 2. Therefore, the new experimental suspensions were designed to incorporate both dual-stage actuation, as well as mode cancelation via symmetrical interconnected sensors.

5.2.2 Experiments On Dual-Stage Prototypes

The open-loop response of the new dual-stage instrumented suspension prototypes, as seen in Fig. 3.15, appeared to have cleaner dynamics with fewer non-off-track modes in the high-frequency range. Moreover, an obvious larger (sway) mode appears in all the frequency response measurements. Combining these observations with the known advantages of collocated sensing and control, we were optimistic that we could achieve successful feedback control. Again, I chose to use a simple inner damping loop to demonstrate high-rate feedback control with the ZnO sensors, this time using the PZT actuator instead of the VCM. It is not immediately clear that using feedback from the sensors to damp vibrations in the PZT response would benefit tracking control. Therefore, to motivate why this would be useful in an overall dual-stage servo controller, we considered the method of *sensitivity decoupling* (SD), as described, for example, in [53] and [40]. The block diagram for a sensitivity decoupling controller is shown in Fig. 5.6.

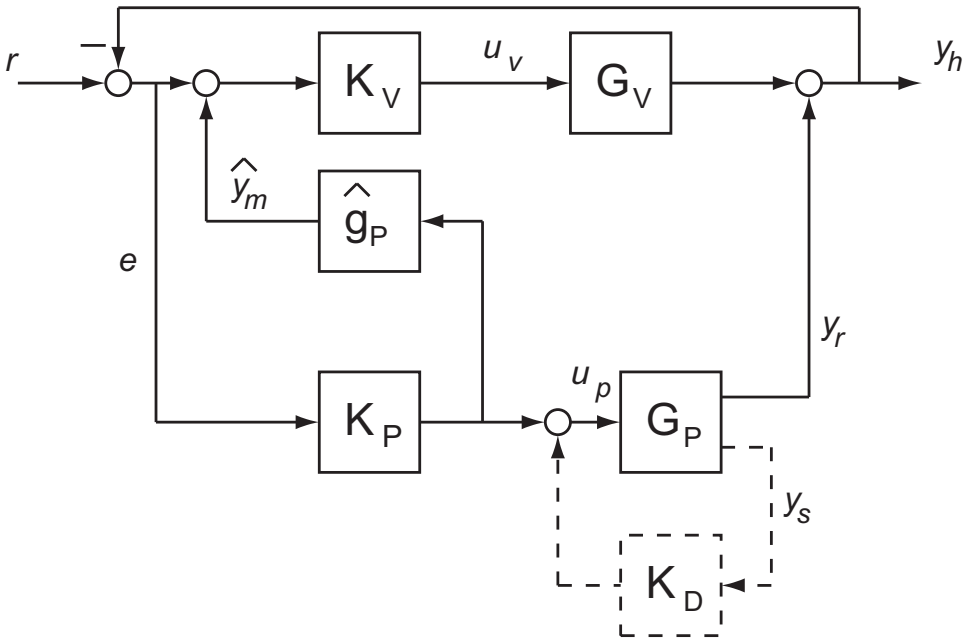

Figure 5.6: Block diagram of a sensitivity decoupling controller with optional inner damping loop.

In this diagram, y_h and y_s are the off-track motion measurement (from the LDV in our case) and strain sensor measurement, respectively; y_r represents the relative off-track motion caused by the PZT actuator; G_p and G_v are the models of the plant dynamics from the PZT actuator and VCM actuator, respectively; u_v and u_p are the actuator inputs into G_p and G_v; r represents track runout; e is the net off-track motion; K_v and K_p are the loop controllers to be designed; K_D is the inner damping controller; and $\hat{g_p}$ is a constant gain used to approximate the physical displacement of the read/write head as a result of the PZT actuator input. Disregarding K_D, and assuming that $\hat{g_p}$ provides a good approximation of

y_r, the open-loop transfer function from r to y_h, G_{open} is

$$G_{open} = G_p K_p + G_v K_v + G_v K_v G_p K_p. \tag{5.9}$$

The total sensitivity function, S_T is then

$$\begin{aligned} S_T &= \frac{1}{1 + G_{open}} \\ &= \frac{1}{(1 + G_v K_v)(1 + G_p K_p)} \\ &= \left(\frac{1}{1 + G_v K_v}\right)\left(\frac{1}{1 + G_p K_p}\right) \\ &= S_v S_p, \end{aligned} \tag{5.10}$$

where S_v and S_p are the sensitivity functions for the VCM loop and PZT loop respectively. The design of these two loops can therefore be designed independently using classical SISO techniques. The VCM loop targets tracking control, while the PZT loop can focus energy on the high-frequency range to increase bandwidth. Furthermore, if the PZT loop can be damped using feedback of high-rate strain sensing, bandwidth can be further augmented, as described in the previous section.

I employed a robust *active mode damping* (AMD) controller, similar to that proposed in [20] for a HDD application. The advantage of this design is its simplicity, relatively low order, and robustness. The controller was designed in continuous time, and then discretized at the desired sampling rate. A controller $K_{D,i}(s)$ is designed for each mode at frequency ω_i, as follows:

$$K_{D,i}(s) = \left(\frac{s + \frac{\omega_i}{\phi_i}}{s + \frac{\beta_i \omega_i}{\phi_i}}\right)\left(\frac{s + \beta_i \phi_i \omega_i}{s + \phi_i \omega_i}\right), \tag{5.11}$$

where ϕ_i and β_i are constant parameters to be tuned. Fig. 5.7 illustrates the effect of changing ϕ_i and β_i. It shows that ϕ_i widens the range of increased magnitude and effectively adds robustness to frequency shifts, while β_i adds phase lead at the frequency, ω_i and to help stabilize the loop. Reasonable values for these parameters are $1 < \phi_i < 3$ and $\phi_i < \beta_i < 15$. An AMD controller can be designed for N_m different modes. The overall AMD controller is then

$$K_D(s) = \prod_{i=1}^{N_m} K_{D,i}(s). \tag{5.12}$$

The controller and plant were discretized using a sampling frequency of 120 kHz, which is aggressive, but still allowed enough time during one sampling interval (8.3 μs) for our DSP board to process the control algorithm. Once again, the hardware was damaged and had to be repaired, so the dynamics of the system for this experiment were slightly altered from those presented in Chapter 3. After numerous design iterations, a controller

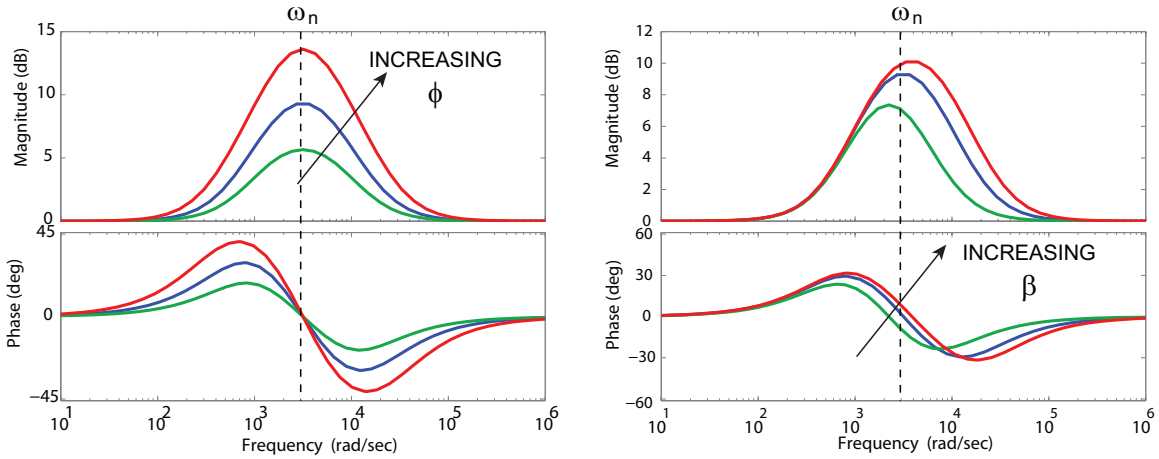

Figure 5.7: Simple example showing the effects of the parameters ϕ_i and β_i on the frequency response of the active mode damping controller.

was designed whose frequency response in discrete time is shown in Fig. 5.8. Note that a notch filter was added at around 14 kHz because the resonance mode there is weakly observable in the sensor response, and we did not want to excite this mode in the off-track displacement. Similar to the single-stage prototypes, the robustness requirement was the limiting factor in the damping control design. The gain and phase margins for this controller are shown in Fig. 5.9. The peaks at the resonant frequencies are fairly close to the 0dB crossover. Making the control gain more aggressive around certain frequencies caused the gain and/or phase margins to be violated. Nonetheless, it was possible to design a controller that predicted moderate damping around the sway mode at about 20.5 kHz. I verified the controller performance in a simulation that used a full-order plant model and mimicked the conditions of the DSP and experimental set-up. The output of the simulation was stable and demonstrated some attenuation of the mode at 20.5 kHz. The simulation also ensured that the command signal to the actuator was within safe limits.

Before implementing a controller, it was necessary to apply an analog anti-aliasing filter to the sensor output to ensure that any modes or noise in the sensor signal at frequencies beyond the Nyquist frequency would be attenuated in the sensor signal. For example, an oscillation around 100 kHz was present in the open loop sensor signal. But with a sampling time of 120 kHz, the corresponding Nyquist frequency is 60 kHz. The 100 kHz oscillation could emerge as a lower-frequency peak in the discretized sensor signal due to aliasing, and could in turn excite the actuator in closed-loop operation. I used a circuit with a resistor and capacitor tuned to yield a corner frequency of about 25 kHz, and unity DC gain.

We successfully implemented the AMD controller on the experimental hardware. Fig. 5.10 shows the predicted damping by comparing the open and closed-loop frequency response from u_p to y_s. The experimental result in Fig. 5.11 matches the prediction fairly well, indicating that the model is accurate, and the sensor noise and aliasing effects are small. However, the important transfer function to consider for sensitivity decoupling con-

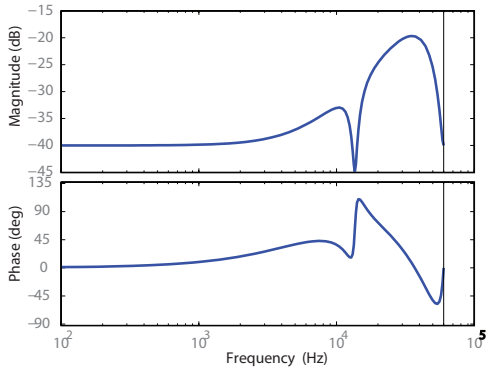

Figure 5.8: Frequency response of the designed AMD controller.

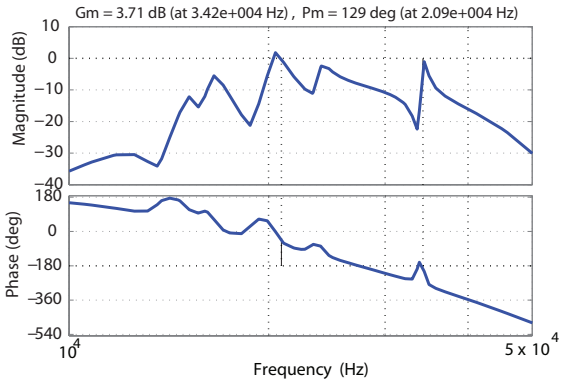

Figure 5.9: Plot of gain and phase margins for the designed AMD controller.

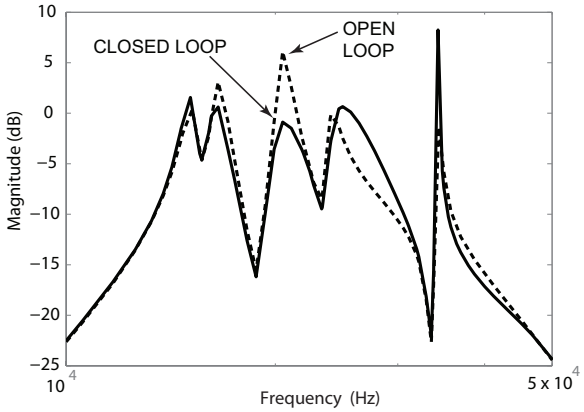

Figure 5.10: Predicted open- and closed-loop response between u_p and y_s with the AMD controller.

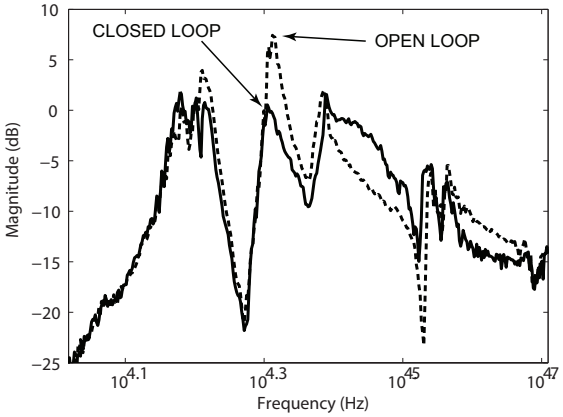

Figure 5.11: Measured open- and closed-loop response between u_p and y_s with the AMD controller.

trol is the damped transfer function from the PZT to the off-track displacement. Fig. 5.12 shows the predicted damping of this transfer function, with moderate suppression of the sway mode at 20.5 kHz. However, the experimental results in Fig. 5.13 revealed a hidden mode around 20 kHz, very close to the sway mode, that was not suppressed.

In both the sensor response and the off-track response, it was predicted that the mode at around 34 kHz would be significantly amplified by the controller. The experimental transfer functions did not detect this amplification, possibly because of averaging, or proximity to the Nyquist frequency. However, the mode was visibly excited in the sensor signal when the controller was turned on. To record this, I measured the frequency spectrum with the controller on, but no external actuator excitation. Figs. 5.14 and 5.15 clearly show the amplification of this mode at 34 kHz. An appropriate way to prevent the excitation of this mode would be to apply a notch filter to the control signal. However, this frequency was so close to the Nyquist frequency associated with the sampling rate that such a notch was

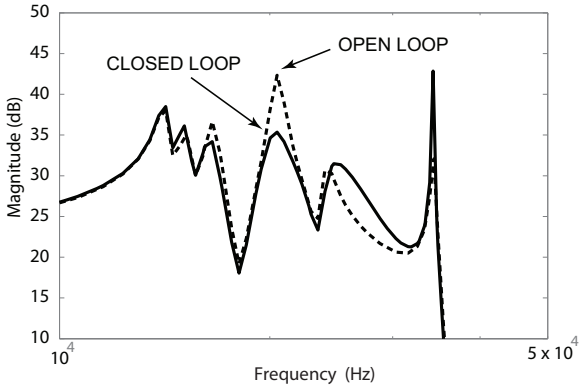

Figure 5.12: Predicted open- and closed-loop response between u_p and y_h with the AMD controller.

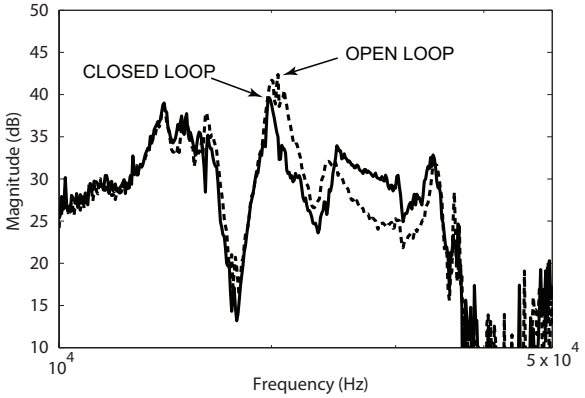

Figure 5.13: Measured open- and closed-loop response between u_p and y_h with the AMD controller.

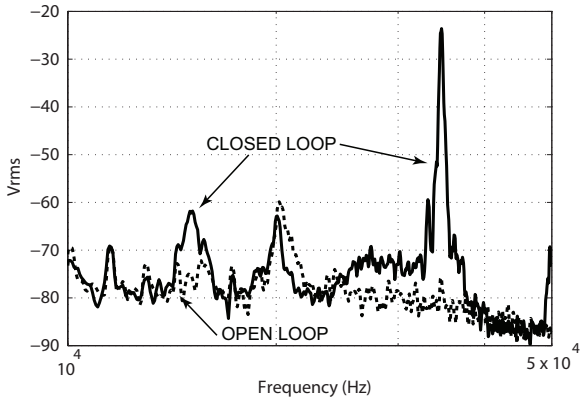

Figure 5.14: Measured open- and closed-loop response between w and y_s with the AMD controller.

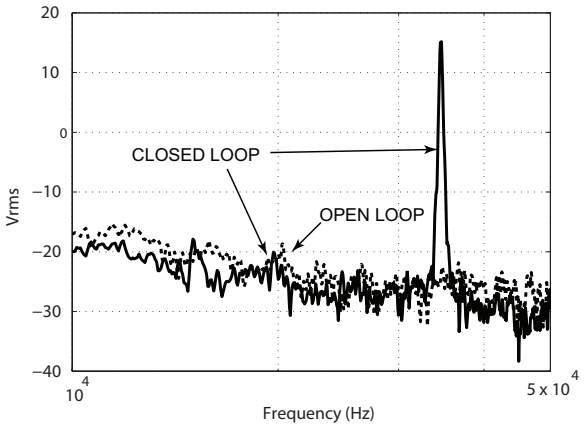

Figure 5.15: Measured open- and closed-loop response between w and y_h with the AMD controller.

difficult to design into the controller at a sampling rate of 120 kHz.

The PZT control signal was well within its limits, with a maximum voltage of about .15 V. We also empirically observed decent robustness of the controller, as it tolerated small adjustments in the overall gain, and small shifts in frequencies without going unstable.

5.3 Adaptive Filtering

Much of the previous work in the area of vibration suppression in HDDs with auxiliary sensors has focused on feedback control, assuming an accurate model of the system and airflow disturbances. However, disk drives vary throughout the manufacturing line, and disturbance characteristics vary throughout operation. Modern robust control synthesis

techniques seek to solve for a feedback controller that optimizes closed-loop performance over a range of plant variations. But optimal robust stability and robust performance inevitably sacrifice some closed-loop performance. The control scheme developed in this section proposed to append a nominal robust controller with an adaptive filter that utilized strain sensing to respond to uncertain disturbance conditions and attain optimal performance online. A lattice filter design provided computational efficiency. I demonstrated the potential benefit of this approach through simulation.

While robust control design typically accounts for uncertainties in the plant model, a common assumption is that the disturbances, such as windage in a disk drive, can be characterized with a fixed model. However, in a real disk drive, the windage disturbance can vary as environmental conditions change [54] and as the head moves to different radii on the disk [55]. Since the auxiliary strain sensors are very sensitive to high frequency structural vibrations, we designed an adaptive filter-based controller that exploits the strain signal to identify changes in windage characteristics and minimize the resulting tracking error. This section describes the proposed framework. Signals and filters will be expressed in the discrete time domain using the time index, k, and the unit delay operator, q^{-1}. In some cases, to avoid clutter, the k and q^{-1} arguments will be dropped from linear operators. $\mathcal{F}_n$ is defined as the set of all real proper finite-impulse response (FIR) filters of order n. The notation $[\star]^T$ means take the transpose and $[\star]^B$ means to reverse the order of the elements of a vector. ("$\star$" refers to an arbitrary value, variable, or index).

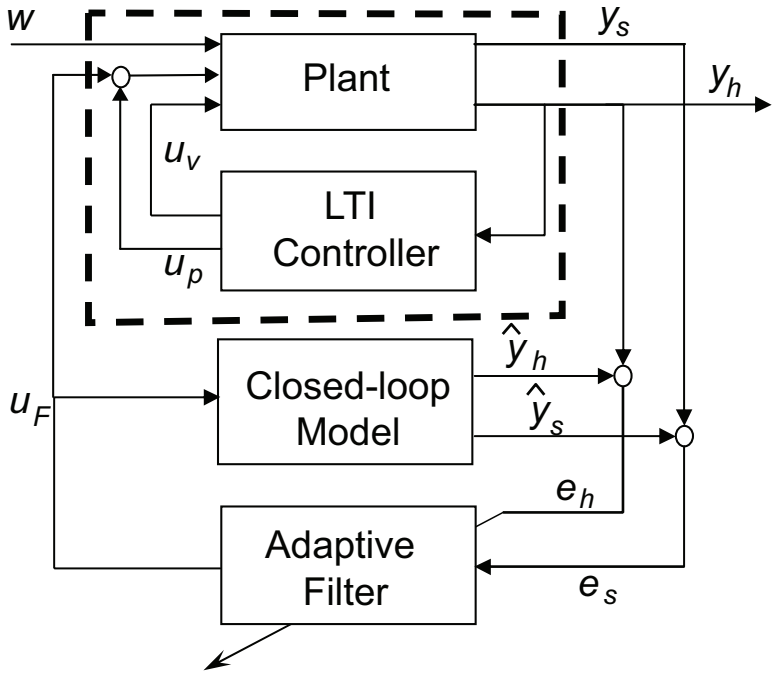

Figure 5.16: Block diagram of control architecture using an adaptive filter.

Fig. 5.16 shows a block diagram of the proposed framework. The baseline closed-

loop system consists of a robust, discrete time, MIMO controller making use of dual-stage actuation and multiple sensors. A model of this closed-loop system is obtained, either from a priori knowledge of the plant model and baseline controller, or from online identification. Measurements are available from the LDV and the strain sensor, which are respectively denoted by $y_h(k)$ and $y_s(k)$. The effect of the windage, $w(k)$, on the closed-loop plant output can be observed from these measurements. The objective is to detect the effect of the windage on the plant output, and use an adaptive filter to generate a PZT control input, $u_F(k)$ that will cancel this affect. Note that u_F is added to the PZT control input generated by the baseline controller. In order to decouple the effect of windage disturbance from the effect of this added control input, $u_F(k)$ is also input into the closed-loop plant model to generate estimates of plant outputs, $\hat{y_h}(k)$ and $\hat{y_s}(k)$. The estimates are subtracted from the measurements to obtain the residuals

$$e_h(k) = y_h(k) - \hat{y_h}(k) \tag{5.13}$$
$$e_s(k) = y_s(k) - \hat{y_s}(k) \tag{5.14}$$

The proposed adaptive filter uses the residual from the strain sensor, $e_s(k)$, as the filter input, and uses the residual from the head displacement, $e_h(k)$ to tune the filter. The formulation of the filter is described as follows. The closed loop system was modeled as

$$y_h(k) = G_{u,h}u_F(k) + G_{w,h}w(k) \tag{5.15}$$
$$y_s(k) = G_{u,s}u_F(k) + G_{w,s}w(k) \tag{5.16}$$

where $G_{u,h}$, $G_{u,s}$, $G_{w,h}$, and $G_{w,s}$, are mappings that represent the closed-loop transfer functions between the inputs and outputs corresponding to the subscripts. The objective is to minimize the variance of $y_h(k)$, restricting the filter, F, to be in $\mathcal{F}_n$.

$$\min E[y_h(k)^2] = \min_{F\in\mathcal{F}_n} \|G_{u,h}u_F + G_{w,h}w(k)\|_2 \tag{5.17}$$

Since $u_F(k)$ is generated by the filter, F, with $e_s(k)$ as the input,

$$\min E[y_h(k)^2] = \min_{F\in\mathcal{F}_n} \|G_{u,h}Fe_s(k) + G_{w,h}w(k)\|_2. \tag{5.18}$$

Here we assume the FIR filter is realized as a transversal filter with n taps, as in

$$F = F(H; q^{-1}) = h_0 + h_1q^{-1} + \ldots + h_nq^{-n} \tag{5.19}$$

and H is the $n \times 1$ tap weight vector $H = (\ h_0 \quad h_1 \quad \ldots \quad h_n\ )^T$. Using the fact that we can commute $G_{u,h}$ and F, and defining the additional filtered signal,

$$m(k) = G_{u,h}e_s(k), \tag{5.20}$$

we have

$$\min E[y_h(k)^2] = \min_{F\in\mathcal{F}_n} \|Fm(k) + e_h(k)\|_2. \tag{5.21}$$

Note the residual, $e_h(k)$, is an approximation of the term $G_{w,h}w$. Since

$$\hat{y_h} = \hat{G}_{u,h}u_F(k), \tag{5.22}$$

where $\hat{G}_{u,h}$ is the model of the closed-loop mapping, $G_{u,h}$, then referring to Eq. (5.15),

$$G_{w,h}w = y_h(k) - G_{u,h}u_F(k) \approx y_h(k) - \hat{y_h}(k) = e_h(k). \tag{5.23}$$

The expression on the right side of Eq. (5.21) is in the form of a Wiener filter problem, as illustrated in Fig. 5.17. The solution can be obtained from classical Wiener filtering theory [56] and is given by

$$H^\circ = E[M(k)M(k)^T]^{-1}E[M(k)e_h(k)] \tag{5.24}$$

$$M(k) = [\ m(k) \quad m(k-1) \quad \dots \quad m(k-n)\ ]^T.$$

The optimal cost is

$$E[y_h(k)^2] = E[e_h(k)e_h(k)] - E[M(k)e_h(k)]^T E[M(k)M(k)^T]^{-1}E[M(k)e_h(k)] \tag{5.25}$$

Similar filtering frameworks have been successfully developed and implemented for HDD tracking control, using as the filter input the PES [57], and an accelerometer [58]. Experimental results in [57] and [58] demonstrated attenuation of random disturbances by such an add-on adaptive controller.

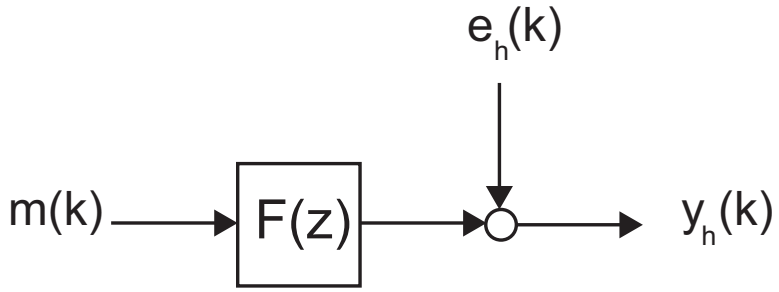

Figure 5.17: Adaptive filter framework reduced to a basic Wiener filter problem.

5.3.1 Lattice Filter Formulation

The solution given in Eq. (5.24) is a batch solution for block estimation. This means that a block of information collected for a certain amount of time is used to compute the filter coefficients offline. But implementing the filter in an adaptive context requires a recursive algorithm that updates the filter parameters with each time step as new information is measured. The performance of such algorithms in terms of convergence and numerical stability essentially depends on how the inverse of the matrix $E[M(k)M(k)^T]$ is computed

or estimated. This in turn depends on both the class of algorithm used, and the filter structure. Two commonly used classes of adaptive filtering algorithms are recursive least squares (RLS) and stochastic gradient (SG) methods. SG methods tend to be easier to implement, but converge slowly. RLS algorithm have the potential for faster convergence, but are more complicated. For high filter orders both adaptive algorithms are prone to large transients during the time when the parameters have not reached their optimal values. As for the filter structure, two main types of FIR filter structures are transversal filters and lattice filters. In general, the lattice filter is known to have superior convergence properties to transversal filters [59]. Moreover, the lattice filter structure is attractive because it results in orthogonalization of FIR parameters [56]. This allows the order of the adaptive FIR lattice filter be be progressively increased, without requiring the re-adaptation of the lower order FIR parameters. Thus, the order of the filter can be gradually increased while still remaining optimal, mitigating the problem with transients. Experimental and simulation results for acoustic noise control [60] and laser beam jitter suppression [61] illustrate the effectiveness of the use of adaptive FIR lattice filters using a framework similar to that in [57] and [58]. In this work, I used a gradient-based lattice filter that combines the nice properties of the lattice filter while being easier to implement. In this section, we give a cursory overview of lattice filter derivation. For more details on the lattice filter formulation, the reader is referred to [56].

The basis of the lattice filter is the forward and backward error predictors of order M for an arbitrary real scalar signal, $v(k)$, defined by $f_M(k)$ and $b_M(k)$, respectively:

$$f_M(k) = v(k) - \sum_{n=1}^{M} p_n^T v(k-n) \tag{5.26}$$

$$b_M(k) = v(k-M) - \sum_{n=1}^{M} q_n^T v(k-n+1) \tag{5.27}$$

or in vector form,

$$f_M(k) = \begin{bmatrix} 1 & -\mathbf{p^T} \end{bmatrix} \begin{bmatrix} v(k) \\ v(k-1) \\ \vdots \\ v(k-M) \end{bmatrix} \tag{5.28}$$

$$b_M(k) = \begin{bmatrix} -\mathbf{q^T} & 1 \end{bmatrix} \begin{bmatrix} v(k) \\ v(k-1) \\ \vdots \\ v(k-M) \end{bmatrix} \tag{5.29}$$

In the following, we assume that v(k) is a wide-sense stationary process. Similar to Eq. (**??**), the optimal coefficients, $\mathbf{p_o}$ and $\mathbf{q_o}$ are given by the Weiner-Hopf equations,

$$\mathbf{R p_o} = \mathbf{r} \tag{5.30}$$

$$\mathbf{R q_o} = \mathbf{r^B} \tag{5.31}$$

where the autocorrelation matrix, $\mathbf{R}$, and the cross correlation vector, $\mathbf{r}$, are defined by

$$\mathbf{R} = E\left[\begin{bmatrix} v(k-1) \\ \vdots \\ v(k-M) \end{bmatrix} \begin{bmatrix} v(k-1) & \dots & v(k-M) \end{bmatrix}\right] \tag{5.32}$$

$$\mathbf{r} = E\left[\begin{bmatrix} v(k-1) \\ \vdots \\ v(k-M) \end{bmatrix} v(k)\right], \tag{5.33}$$

By combining Eqs. (5.30) and (5.31), and with some manipulation, it can be shown that the optimal coefficients of the forward and backward predictors are related by

$$\mathbf{q_o^B} = \mathbf{p_o}. \tag{5.34}$$

Next, we introduce the Levinson-Durbin algorithm that recursively updates the set of optimal prediction coefficients with respect to the order of the predictor, M:

$$\begin{bmatrix} 1 \\ \mathbf{-p_M} \end{bmatrix} = \begin{bmatrix} 1 \\ \mathbf{-p_{M-1}} \\ 0 \end{bmatrix} + \Gamma_M \begin{bmatrix} 0 \\ 1 \\ \mathbf{-p^B_{M-1}} \end{bmatrix} \tag{5.35}$$

Γ_M is called the *reflection coefficient* associated with order M, and it is related to $\mathbf{R}$ and $\mathbf{r}$. Note that there is an equivalent equation for the backward predictor. Using the fact from Eq. (5.34), the equations for the forward and backward predictors can be combined, and the $\mathbf{p}_\star$ and $\mathbf{q}_\star$ coefficients can be eliminated, yielding the following:

$$\begin{bmatrix} f_M(k) \\ b_M(k) \end{bmatrix} = \begin{bmatrix} 1 & \Gamma_M \\ \Gamma_M & 1 \end{bmatrix} \begin{bmatrix} f_{M-1}(k) \\ b_{M-1}(k-1) \end{bmatrix} \tag{5.36}$$

To summarize, by combining the backward and forward predictor, the optimal prediction problem has been reparameterized in terms of reflection coefficients instead of transversal filter coefficients. A valuable property of this formulation is that the backwards predictions associated with different orders are orthogonal. This means that the optimal values of $b_0(k)$, $b_1(k)$, $b_2(k)...b_M(k)$ are independent of each other. For example, suppose we determine the optimal coefficients, Γ_1 and Γ_2 for a 2nd order predictor. Then, increase the order to 3rd order and obtain the optimal coefficients. Γ_1 and Γ_2 will be the same. This is not the case for a transversal filter.

Finally, the lattice structure can be extended to joint process estimation in which a second set of weights is applied to the backward error signals of different orders. Fig. 5.18 illustrates a block diagram for a lattice-based FIR filter, showing the formulation that is equivalent to the Wiener filter is Fig. 5.17. While this structure appears to make the joint-process estimation more complicated, with three times as many parameters as a simple transversal filter, the orthogonal properties of the algorithm eliminate the need to invert the $\mathbf{R}$ matrix, making the algorithm more computationally efficient.

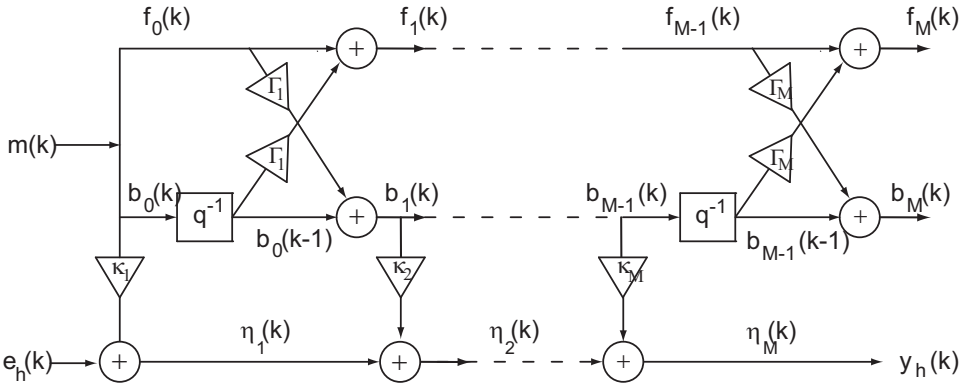

Figure 5.18: Lattice filter structure used to tune the filter parameters; it is equivalent to the Wiener filter formulation.

5.3.2 Gradient-Based Algorithm

I used a gradient-based algorithm as developed in [56] and [60]. To derive a recursive algorithm, we start with the relationship between stages of the lattice filter shown in Fig. 5.18, given in the following equations:

$$f_n(k) = f_{n-1}(k) + b_{n-1}(k-1)\Gamma_n^f(k) \quad (5.37)$$

$$b_n(k) = b_{n-1}(k-1) + f_{n-1}(k)\Gamma_n^b(k). \quad (5.38)$$

The objective for the optimal prediction parameters is to minimize the following costs:

$$J_n^f(k) = E[f_n(k)^2] \quad (5.39)$$

$$J_n^b(k) = E[b_n(k)^2]. \quad (5.40)$$

Let us consider the first equation in Eq. (5.39). Recall that we are trying to identify the reflection coefficient, Γ_n^f. Expanding the cost function, we get

$$J_n^f(k) = E[f_{n-1}(k)^2 + 2f_{n-1}(k)b_{n-1}(k-1)\Gamma_n^f(k) + [b_{n-1}(k-1)\Gamma_n^f(k)]^2] \quad (5.41)$$

The gradient of this expression with respect to $\Gamma_n^f(k)$ is

$$\begin{aligned} \nabla(J_n^f(k)) &= E[2f_{n-1}(k)b_{n-1}(k-1) + 2b_{n-1}(k-1)^2\Gamma_n^f(k)] \\ &= E[2b_{n-1}(k-1)[f_{n-1}(k) + b_{n-1}(k-1)\Gamma_n^f(k)]] \\ &= 2E[b_{n-1}(k-1)f_n(k)]. \end{aligned} \quad (5.42)$$

Similarly, the gradient of $J_n^b(k)$ with respect to $\Gamma_n^b(k)$ is

$$\nabla(J_n^b(k)) = 2E[f_{n-1}(k)b_n(k)]. \quad (5.43)$$

The instantaneous estimates for the gradients of the cost functions are then

$$\nabla(J_n^f(k)) \approx 2b_{n-1}(k-1)f_n(k) \quad (5.44)$$

$$\nabla(J_n^b(k)) \approx 2f_{n-1}(k)b_n(k). \quad (5.45)$$

The reflection coefficients can then be updated recursively using the method of steepest descent, as in

$$\Gamma_n^f(k+1) = \Gamma_n^f(k) + \delta_n^f(k)[b_{n-1}(k-1)f_n(k)] \quad (5.46)$$
$$\Gamma_n^b(k+1) = \Gamma_n^b(k) + \delta_n^b(k)[f_{n-1}(k)b_n(k)], \quad (5.47)$$

where $\delta_n^f(k)$ and $\delta_n^f(k)$ are time-varying step size parameters. In order to balance convergence and robustness, the recommended update equations for the step size parameters are

$$\frac{1}{\delta_n^f(k)} = \lambda\frac{1}{\delta_n^f(k-1)} + b_{n-1}(k-1)^2 \quad (5.48)$$
$$\frac{1}{\delta_n^b(k)} = \lambda\frac{1}{\delta_n^b(k-1)} + f_{n-1}(k)^2 \quad (5.49)$$

with forgetting factor $0 < \lambda < 1$ [60].

The recursive algorithm to update the FIR coefficients is derived in a similar manner. The output error, $\eta_n(k)$, at each stage, is given by

$$\eta_n(k) = \eta_{n-1}(k) + b_{n-1}(k)\kappa_n(k). \quad (5.50)$$

The objective is to minimize the variance of the output error, $J_n^\eta(k)$. Similar to Eqs. (5.43) and (5.44), the instantaneous estimate for the gradient of the cost function is

$$\nabla(J_n^\eta(k)) = 2b_{n-1}(k)\eta_n(k). \quad (5.51)$$

Correspondingly, the FIR coefficients may be computed recursively by

$$\kappa_n(k+1) = \kappa_n(k) + \delta_n^\eta(k)[b_{n-1}(k)\eta_n(k)], \quad (5.52)$$

with step size, δ_n^η. According to [60],

$$\frac{1}{\delta_n^\eta(k)} = \frac{1}{\delta_n^f(k+1)}, \quad (5.53)$$

slightly simplifying the algorithm. The gradient-based algorithm for tuning the FIR lattice filter coefficients is outlined in Algorithm 1. Note that this algorithm only tunes the coefficients, but does not generate the actual control output. A separate set of recursive equations is required to output the actual control command signal. Fig. 5.19 illustrated the lattice filter used to generate the actual control signal.

5.3.3 Implementation And Simulation Results

Using MATLAB, I coded and applied the adaptive lattice filter framework in simulation to a plant model based on the dual-stage HDD with ZnO sensors. First, I designed a baseline controller assuming a certain windage model. Then, I injected a different windage

Time initialization: k = -1
for $n = 1$ *to* N **do**
$b_n(-1) = 0$;
$(\delta_n^f)^{-1} = (\delta_n^b)^{-1} = c$, c is a small positive number;
$\Gamma_n^f(-1) = \Gamma_n^b(-1) = 0$;
$\kappa_n(-1) = 0$;
end
while $k \geq 0$ **do**
Order initialization: $n = 0$
$f_0(k) = b_0(k) = m(k)$;
$\eta_0(k) = e_h(k)$;
for $n = 1$ *to* N **do**
$(\delta_n^f(k))^{-1} = \lambda * (\delta_n^f(k-1))^{-1} + b_{n-1}^2(k-1)$;
$(\delta_n^b(k))^{-1} = \lambda * (\delta_n^b(k-1))^{-1} + f_{n-1}^2(k)$;
$\Gamma_n^f(k) = \Gamma_n^f(k-1) + \delta_n^f(k-1)b_{n-1}(k-2)f_n(k-1)$;
$\Gamma_n^b(k) = \Gamma_n^b(k-1) + \delta_n^b(k-1)f_{n-1}(k-1)b_n(k-1)$;
$f_n(k) = f_{n-1}(k) + b_{n-1}(k-1)\Gamma_n^f(k)$;
$b_n(k) = b_{n-1}(k-1) + f_{n-1}(k)\Gamma_n^b(k)$;
$\kappa_n(k) = \kappa_n(k-1) + \delta_n^f(k)b_{n-1}(k-1)\eta_n(k-1)$;
$\eta_n(k) = \eta_{n-1}(k) + b_{n-1}(k)\kappa_n(k)$;
end
end

Algorithm 1: Gradient-based algorithm for tuning lattice filter coefficients

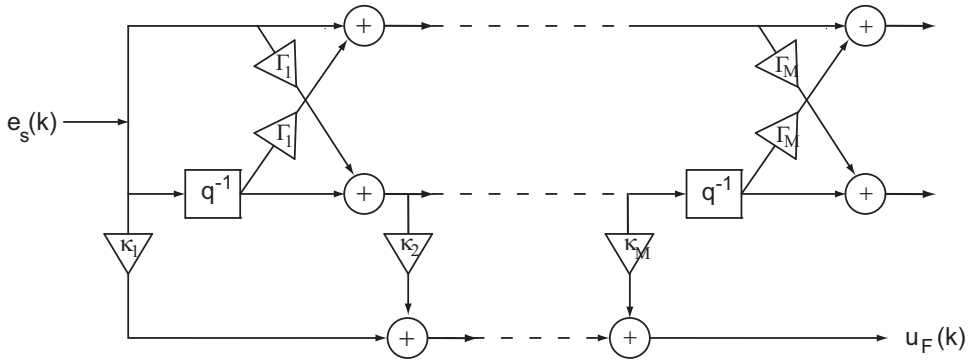

Figure 5.19: Lattice filter used to generate additive control input, u_F.

disturbance into the baseline closed-loop system. The lattice filter was turned on to evaluate how well the new windage disturbance can be rejected.

I used the plant model identified in Chapter 3, and shown in Fig. 3.15, with two modes eliminated to make the model order more reasonable. Noise in the piezoelectric sensor and LDV were assumed to be .003 V and .002 V, respectively, with the LDV scale set to 500 nm per V. As a baseline controller, I designed a frequency-shaped discrete time H_2 controller

for the dual-input, dual-output system. The plant was discretized at a rate of 75 kHz, and an input delay of 6 μs was assumed, which is based on experience with our experimental set up and typical controller order. A simple windage model characterized the disturbance as a white noise added to the VCM input, and scaled by 1e-4. Once again, I did not consider runout disturbance, to be consistent with the experimental setup, and with other control studies in this chapter. During control design, frequency shaping filters balanced the usage of the actuators and closed-loop performance. I reduced the controller order to 12 states using balanced truncation. The baseline controller reduced the standard deviation of the motion from windage disturbance from 361 nm to 5.4 nm, as predicted by the norm of the linear time invariant open-loop and closed-loop systems.

Next, a new windage model was injected into the baseline closed-loop system by passing the white noise through a coloring filter before adding it to the VCM input. The coloring filter used in the simulation added a peak around 12 kHz, as shown in Fig. 5.20. The continuous time transfer function for the coloring filter is given by

$$W_c = \frac{80000s + 6.4 * 10^9}{s^2 + 100s + 6.4 * 10^9}. \tag{5.54}$$

This new windage disturbance increased the standard deviation of off-track motion to 75.4 nm, as predicted by the system norm. The discrete-time closed loop plant was simulated in MATLAB with the add-on adaptive lattice filter. Simulations were performed for filter orders of 2 and 4, and varying forgetting factors.

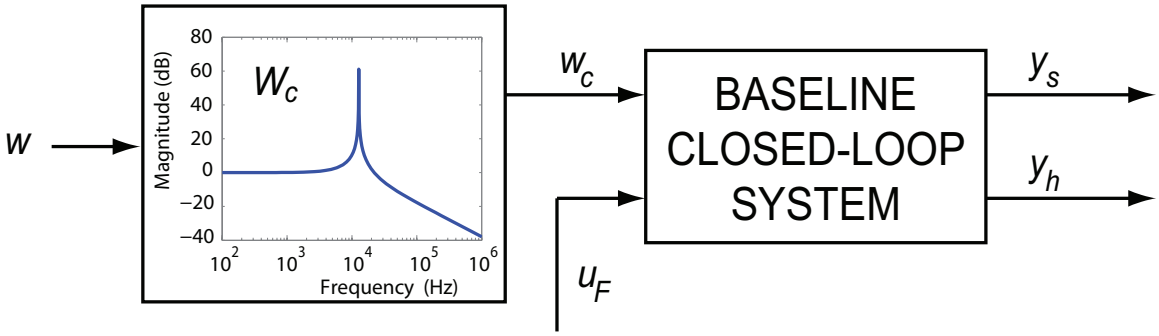

Figure 5.20: Coloring filter used to generate an unmodeled windage disturbance.

Performance was sensitive to the choice of forgetting factor. As expected, there was a trade-off between slow convergence and rapid fluctuations in the parameter values excited by exogenous stochastic disturbances. The example in Fig. 5.21 had a forgetting factor of $\lambda = .9$. The output converged in 1.3 milliseconds (or .16 revolutions), and the parameter values were noisy with relatively large variations. On the other hand, the example in Fig. 5.21 had a forgetting factor of $\lambda = .997$. The output converged much more slowly, in 26 milliseconds (or 3.2 revolutions), but the parameter values have small fluctuations. A forgetting factor of $\lambda = .99$ achieved a good balance, as seen in Figs. 5.23 and 5.24. These two examples demonstrated the effect of changing the filter order. The example

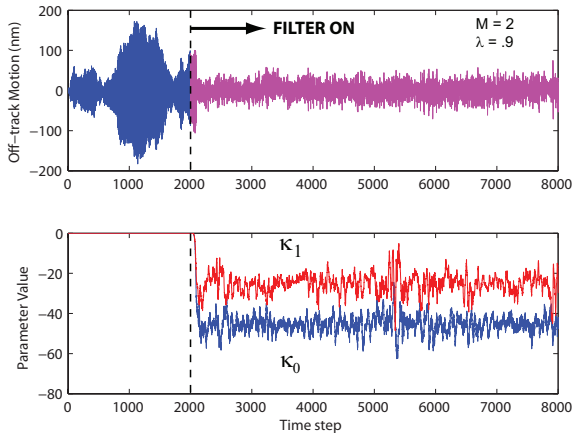

Figure 5.21: Simulation of closed-loop system with add-on lattice filter of order $M = 2$ and with a forgetting factor of $\lambda = .9$. Top: time response, bottom: filter parameters.

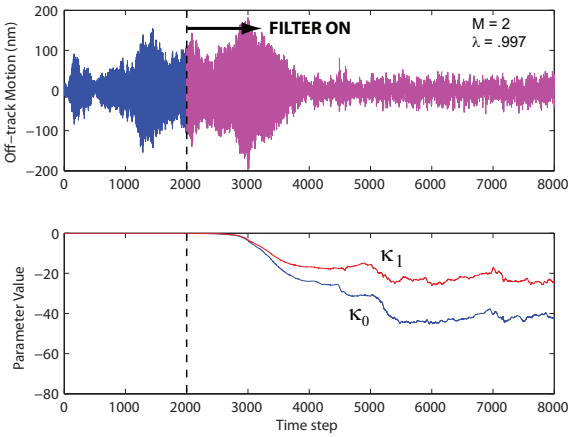

Figure 5.22: Simulation of closed-loop system with add-on lattice filter of order $M = 2$ and with a forgetting factor of $\lambda = .997$. Top: time response, bottom: filter parameters.

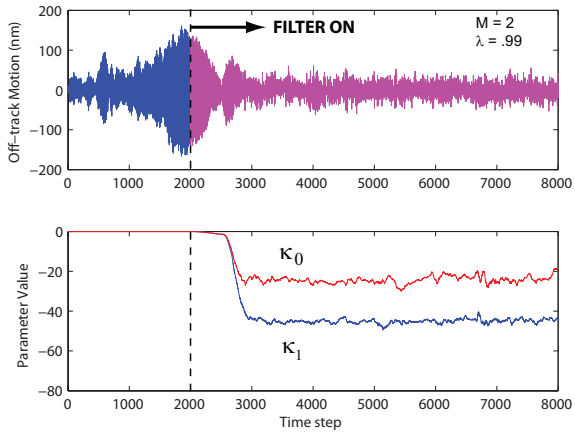

Figure 5.23: Simulation of closed-loop system with add-on lattice filter of order $M = 2$ and with a forgetting factor of $\lambda = .99$. Top: time response, bottom: filter parameters.

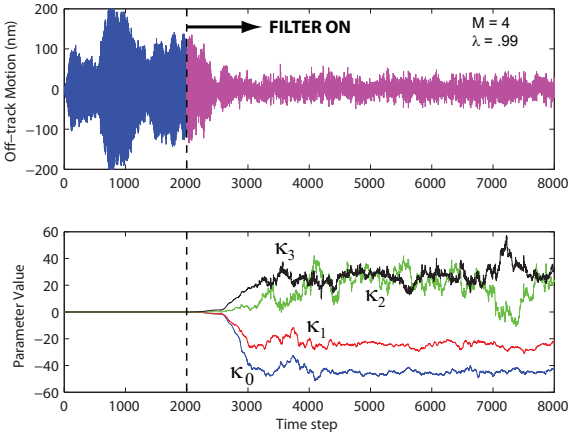

Figure 5.24: Simulation of closed-loop system with add-on lattice filter of order $M = 4$ and with a forgetting factor of $\lambda = .99$. Top: time response, bottom: filter parameters.

with a single-stage lattice (two parameters), the output converged in 12 milliseconds (or 1.4 revolutions) revolutions, and reduced the standard deviation of the output to 16.8. With a three-stage lattice (four parameters), the output converged in 13 milliseconds (or 1.6 revolutions) and reduced the standard deviation of the output to 16.3 nm. Thus, I

observed that increasing the order did not improve the performance much. This seemed reasonable, since the order of the unmodeled windage in Eq. (5.54) was small.

I observed that the effectiveness of the adaptive filter was sensitive to the weighting functions that were used to design the baseline controller, and to how the windage was modeled. This may be because the weighting functions and disturbance models affect the optimization cost function for the H_2 control design. On the other hand, the filtering problem minimized the variance of the output with no frequency shaping.

To verify that the lattice filter parameters converged to the correct values, I analytically derived the optimal parameters for an equivalent transversal filter and compared the two sets of parameters. Recall the Wiener filter structure, shown in Fig. 5.17. Using models of the plant and disturbances, I constructed an extended discrete time state space system with the signals $m(k)$ and $e_h(k)$ as the outputs:

$$\begin{aligned} \xi(k+1) &= A_e\xi(k) + B_e w_e(k) && (5.55) \\ y_e(k) = \begin{bmatrix} m(k) \\ e_h(k) \end{bmatrix} &= C_e\xi(k) + D_e w_e(k), && (5.56) \end{aligned}$$

where $w_e(k)$ is an extended vector of exogenous white noise inputs of measurement noise and windage excitation, with covariance W_e. Then I computed the autocorrelation matrix and cross-correlation vector of the extended system. In the following, the notation $\Lambda^\ell_\bigstar$ is defined as follows:

$$\Lambda^\ell_\bigstar = E[\bigstar(k-\ell)\bigstar^T(k)] \tag{5.57}$$

The steady-state covariance of $\xi(k+1)$, Λ^0_ξ, was found by solving the Lyapunov equation [62]

$$\Lambda^0_\xi - A_e\Lambda^0_\xi A_e^T = B_e W_e B_e^T. \tag{5.58}$$

The covariance matrix of $y_e(k+1)$, $\Lambda^0_{y_e}$, is then

$$\Lambda^0_{y_e} = C_e\Lambda^0_\xi C_e^T + D_e W_e D_e^T. \tag{5.59}$$

The autocorrelation matrix of $\xi(k+1)$, Λ^ℓ_ξ, is given by

$$\Lambda^\ell_\xi = \Lambda^0_\xi A^{T\ell}. \tag{5.60}$$

For $\ell \neq 0$, the autocorrelation matrix of $y_e(k+1)$, $\Lambda^\ell_{y_e}$, is computed as follows:

$$\begin{aligned} \Lambda^\ell_{y_e} &= E[y_e(k-\ell)y_e^T(k)] \\ &= E[\{C_e\xi(k-\ell) + D_e w_e(k-\ell)\}\{C_e\xi(k) + D_e w_e(k)\}^T] \\ &= E[C_e\xi(k-\ell)\xi^T(k)C_e^T + D_e w_e(k-\ell)\xi^T(k)C_e^T]. \end{aligned} \tag{5.61}$$

The last line of Eq. (5.61) follows since $w_e(k)$ is white and it is not correlated to previous values of $\xi(k)$. Expanding $\xi(k)$ using the solution for linear discrete time systems,

$$\xi(k) = A_e^\ell\xi(k-\ell) + \sum_{j=1}^{\ell} A_e^{(j-1)} B_e w_e(k-j). \tag{5.62}$$

The only term correlated with $w(k-l)$ is $A_e^{\ell-1}B_e w_e(k-\ell)$, so

$$\begin{aligned}\Lambda_{y_e}^{\ell} &= E[C_e\xi(k-\ell)\xi^T(k)C_e^T + D_e w_e(k-\ell)w_e^T(k-\ell)B_e^T A_e^{T(\ell-1)}C_e^T] \\ &= C_e\Lambda_\xi^\ell C_e^T + D_e W_e B_e^T A^{T(\ell-1)}C_e^T. \end{aligned} \tag{5.63}$$

Since

$$\Lambda_{y_e}^{\ell} = E\begin{bmatrix} m(k-\ell)m^T(k) & m(k-\ell)e_h^T(k) \\ e_h(k-\ell)m^T(k) & e_h(k-\ell)e_h^T(k) \end{bmatrix}, \tag{5.64}$$

we have all the information we need to obtain the solution for the optimal transversal filter parameters, as well as the optimal cost, as in Eqs. (5.24) and (5.25), respectively.

Using the block diagram in Fig. 5.18, I derived a relation between the lattice filter parameters and the transversal parameters. For example, for a first order filter,

$$u_F(k) = \kappa_1 e_s(k) + \kappa_2[\Gamma_1 e_s(k) + e_s(k-1)] \tag{5.65}$$

so the parameters for the filter, $u_F(k) = h_1 e_s(k) + h_2 e_s(k-1)$ can be related to the lattice filter parameters by

$$h_1 = \kappa_1 + \kappa_2 * \Gamma_1 \tag{5.66}$$

$$h_2 = \kappa_2 \tag{5.67}$$

Using these equations, I was able to verify that the simulations performed as expected and converged upon the correct parameters. For a filter with two parameters, the theoretical Wiener filter parameters are h_1 = -33, and h_2 = -24. From the simulation, the parameters for a single stage lattice filter converged to κ_1 = -44, κ_2 = -24, and Γ_1 = -.47. From Eq. (5.66) the estimated Wiener filter parameters computed from the lattice filter parameters are $\hat{h_1}$ = -32.7, and $\hat{h_2}$ = -24. The theoretical minimum computed from Eq. (5.25) was 16.9 nm with two parameters and 16.2 with four parameters. This is also consistent with the standard deviation of the simulation after parameter convergence.

5.3.4 Remarks On Stability

The adaptive scheme described in this section uses an explicit model of the baseline closed-loop system. This framework is referred to as *internal model control* (IMC) [51] [63]. As discussed in [63], the IMC structure can be expressed as a special case of the Youla parameterization of all stabilizing controllers for a given stable plant. To review a sketch of this results, suppose the transfer function of a plant, $P(s)$, is stable. It is a known result that every stabilizing controller, $K(s)$, can be represented by

$$K(s) = \frac{Q(s)}{1 - P(s)Q(s)}, \tag{5.68}$$

where $Q(s)$ is any stable, rational transfer function [51]. An equivalent feedback system is illustrated in Fig. 5.25. This in turn can be transformed into the IMC structure shown in Fig. 5.26. This IMC structure resembles the adaptive filter framework pictured in Fig.

5.16. In our case, $P(s)$ is the baseline closed-loop plant, which was designed to be stable, and $Q(s)$ is the adaptive filter. Since we choose the filter to be a FIR filter, it will be stable, and so the overall feedback system will stabilizing. The caveat is that an accurate model of the baseline system is required. For our set-up, this is reasonable, since we are able to identify and reliable model offline (as demonstrated by the matching between predicted and experimental results in Section 5.2.2.) Researchers have proposed similar IMC frameworks in which the internal plant model is updated online [58] [63]. To apply this adaptive scheme to actual HDDs, such modifications will be necessary.

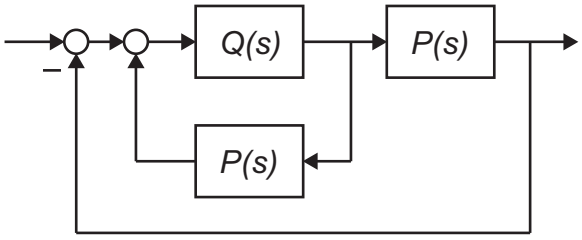

Figure 5.25: Equivalent block diagram of Youla parameterized system.

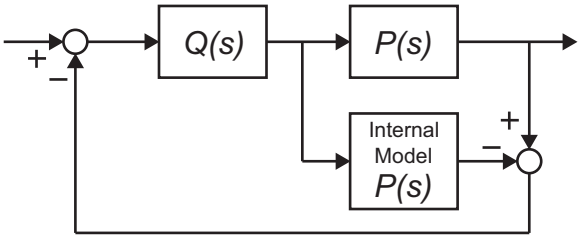

Figure 5.26: Equivalent block diagram of internal model control structure.

5.4 Summary

This chapter covered several studies that assessed the potential improvements that instrumented suspensions could afford for suppression of off-track vibrations. All of these studies used realistic models identified from the results of testing as in Chapter 3. Simulations of optimal, nominal H_2 control using multi-rate sensing showed that vibration suppression could potentially be improved by adding extra high-rate sensing. Dual-stage instrumented suspensions demonstrated some feedback action that attenuated a narrow band of vibration modes. However, performance was limited due to the irregular dynamics of the prototypes. Finally, a more elaborate adaptive controller was developed and simulated which used sensor measurements to adjust to varying windage disturbance and achieve better performance online.

Chapter 6

Conclusions and Future Work

6.1 Conclusions

This paper described the integration of thin-film ZnO strain sensors onto hard disk drive suspensions for improved vibration suppression and tracking control. Major contributions of this dissertation research were:

1. process improvement and characterization of ZnO deposition on steel substrates,
2. complete fabrication of new dual-stage instrumented suspension prototypes,
3. installation and comprehensive dynamic testing of several dual-stage instrumented suspension prototypes,
4. critical comparison of dual-stage instrumented suspensions and self-sensing PZT actuated suspensions,
5. experimental demonstration of sensor feedback used for vibration suppression, and
6. development and simulation of an adaptive lattice filter that uses instrumented suspensions.

I compared the performance of the new dual-stage prototypes with earlier single-stage prototypes. Both prototypes exhibited superior SNR compared to LDV measurements. The interconnection of symmetrical sensors in the newer prototypes to cancel bending modes and common noise resulted in a cleaner sensor response in the high-frequency range of interest, but did not entirely eliminate all non-off-track modes. Regardless, the improved dynamics and the addition of a dual-stage controller resulted in a prototype with open-loop dynamics that were conducive to feedback control.

I achieved the first successful demonstration of feedback control using instrumented suspensions. A simple and somewhat conservative damping controller was able to attenuate some high-frequency modes to provide extra margin for decoupled dual-stage control design. However, the experimental prototypes exhibited irregular dynamics, making simple damping control difficult. To explore a more high-performance control, I designed and

simulated an advanced adaptive filter that was able to use the sensors to minimize off-track motion in the face of changing windage disturbances.

Throughout the process of experimental measurements, I encountered many problems with hardware reliability, since it was necessary for multiple tiny and fragile components to be operating correctly simultaneously. In particular, the miniaturized instrumentation circuit was difficult to assemble and debug. For successful implementation of instrumented suspensions in the future, development of a reliable circuit using more standardized integrated circuitry will be crucial. Also, more automated assembly practices will significantly reduce failures in future prototypes.

Due to the reliability limitations of the instrumented suspensions, an alternate sensing platform was developed in parallel using self-sensing techniques. I discovered that self-sensing had both practical advantages and disadvantages compared to instrumented suspensions. Thus, it is anticipated that both techniques could provide a good sensing method, depending on the application and hardware configuration.

6.2 Future Work

Several areas could be targeted to improve the integrity and performance of the prototypes. First, the process of etching the steel wafer around the fabricated sensors needs to be optimized so that dramatic lateral etching does not occur. Second, while cracking was successfully eliminated during sensor processing, the sensors were still prone to cracking during forming of the hinge and assembly of the suspension. It is possible that a more physically robust sensor could be fabricated from a piezoelectric polymer such as PVDF. This would, of course, require extensive process development. Third, both the instrumented suspension and self-sensing suspension suffered from electrical feedthrough, which is a common problem in micro-scale systems with closely situated actuators and sensors. A method of frequency modulation could provide better decoupling of the actuator and sensor signals in both cases.

Regarding closed-loop control, the next step would be to improve the damping controller by implementing a high-rate notch filter to target the peak at 34 kHz. After that, a complete dual-stage controller using sensitivity decoupling can be demonstrated. The adaptive control study opened up a few directions as well. The design might be improved with frequency shaping applied to the adaptive filter, so that the objective more closely matches the cost function used in H_2 control. When applying an adaptive controller, it is common to find that the performance is sensitive to algorithm parameters such as forgetting factor and step size. The sensitivity to such parameters in the instrumented suspension system needs to be more thoroughly examined before a real controller could be implemented. Finally, we began to reformulate the adaptive filter to use controller residuals instead of the internal model approach. It is anticipated that this scheme could enable reduced computation and better robustness, but this approach requires further development.

Bibliography

[1] P. Antsaklis, A. Michel, Linear Systems, McGraw-Hill, 1998.

[2] C. M. Kozierok, http://www.pcguide.com/ref/hdd/op/spin_Speed.htm (2001).

[3] G. F. Franklin, J. D. Powell, M. Workman, Digital Control of Dynamic Systems, 3rd Edition, Addison Wesley Longman, Inc., Menlo Park, CA, USA, 1998.

[4] R. M. Ehrlich, P. A. Weaver, The use of multirate notch filters in embedded-servo disk drives, in: Proceedings of the American Control Conference, 1995, pp. 4156–4160.

[5] T. Asumi, T. Arisaka, T. Shimizu, H. Masuda, Head-positioning control using resonant modes in hard disk drives, IEEE Transactions on Mechatronics 10 (2005) 378–384.

[6] R. Evans, J. Griesbach, W. Messner, Piezoelectric microactuator for dual-stage control, IEEE Transactions on Magnetics 35 (1999) 977–81.

[7] M. Tokuyama, T. Shimizu, H. Masuda, S. Nakamura, M. Hanya, O. Iriuchijima, J. Soga, Development of ϕ-shaped actuated suspension for 100-ktpi hard disk drives, IEEE Transactions on Magnetics 33 (3) (2001) 1184–6.

[8] I. Naniwa, S. Nakamura, S. Saegusa, K. Sato, Low voltage driven piggy-back actuator of hard disk drives, in: IEEE International MEMS 99 Conference, Orlando, FL, USA, 1999, pp. 49–52.

[9] S. Koganezawa, K. Takaishi, Y. Mizoshita, Y. Uematsu, T. Yamada, Development of integrated piggyback milli-actuator for high density magnetic recording, in: International Conference on Micromechatronics for Information and Precision Equipment, 1997, pp. 20–23.

[10] D. Horsley, Ph.D. Dissertation: Microfabricated electrostatic actuators for magnetic disk drives, University of California, Berkeley, CA, USA, 1998.

[11] T. Hirano, L. Fan, T. Semba, W. Lee, J. Hong, S. Pattanaik, P. Webb, W.-H. Juan, S. Chan, High-bandwidth hdd tracking servo by a moving-slider micro-actuator, IEEE Transactions on Magnetics 35 (1999) 3670–72.

[12] H. Fujita, K. Suzuki, M. Ataka, S. Nakamura, A microactuator for head positioning system of hard disk drives, IEEE Transactions on Magnetics 35 (1999) 1006–10.

[13] H. Kuwajima, K. Matsuoka, Thin film piezoelectric dual-stage actuator for hdd, in: InterMag Europe, Session BS04, Amsterdam, Netherlands, 2002, p. BS4.

[14] S. Nakamura, K. Suzuki, M. Ataka, K. Mukasa, An electrostatic microactuator for a magnetic head tracking system of hard disk drives, in: Advances in Information Storage Systems, Vol. 10, Singapore, 1998, pp. 83–99.

[15] H. Toshiyoshi, M. Mita, H. Fujita, A mems piggyback actuator for hard-disk drives, Journal of Microelectromechanical Systems 11 (6) (2002) 648–54.

[16] M. T. White, M. Tomizuka, Increased disturbance rejection in magnetic disk drive by acceleration feedforward control, IFAC Journal of Control Engineering Practice 5 (6) (1997) 741–51.

[17] F. Y. Huang, W. Semba, W. Imaino, F. Lee, Active damping in hdd actuator, IEEE Transactions and Magnetics 37 (2) (2001) 847–849.

[18] Y. Li, R. Horowitz, R. Evans, Vibration control of a pzt actuated suspension dual-stage servo system using a pzt sensor, IEEE Transactions on Magnetics 39 (2003) 932–7.

[19] M. Sasaki, H. Yamada, Y. Nam, S. Ito, Two-degree-of-freedom control of a self-sensing micro-actuator for hdd using neural networks, in: 9th International Conference on Control, Automation, Robotics and Vision, Singapore, 2006, pp. 1–6.

[20] C. K. Pang, G. Guo, B. M. Chen, T. H. Lee, Nanopositioning sensing and control in hdd dual-stage servo systems, in: Proceedings of the 2004 IEEE International Conference on Control Applications, Vol. 1, 2004, pp. 551–556.

[21] S.-H. Lee, C. C. Chung, C. W. Lee, Active high-frequency vibration rejection in hard disk drives, IEEE Transactions on Mechatronics 11 (2006) 339–345.

[22] P. Gao, S. M. Swei, Active actuation and control of a miniaturized suspension structure in hard-disk drives using a polyvinylidene-flouride actuator and sensor, Measurement Science and Technology 11 (2000) 88–94.

[23] S. Ohtsuka, S. Koganezawa, T. Hara, K. Funabashi, T. Matsuzawa, Piezoelectric film attached suspension for detecting disk flutter and reducing track misregistration, Microsystem Technology (2009) published online.

[24] Y. Huang, M. Banther, P. D. Mathur, W. C. Messner, Design and analysis of a high bandwidth disk drive servo system using an instrumented suspension, IEEE Transactions and Magnetics 4 (2) (1999) 196–206.

[25] S. Felix, S. Kon, J. Nie, R. Horowitz, Strain sensing with piezoelectric zno thin films for vibration suppression in hard disk drives, in: Proceedings of the Dynamic Systems and Control Conference, Ann Arbor, Michigan, 1008.

[26] S. Kon, High resolution mems strain sensors for vibration detection on hard disk drive instrumented suspensions, Ph.D. thesis, University of California, Berkeley (2007).

[27] K. Oldham, S. Kon, R. Horowitz, Fabrication and optimal stain sensor placement in an instrumented disk drive suspension for vibration suppression, in: Proc. of the 2004 American Control Conference, Boston, MA, USA, 2004, pp. 1855–1861.

[28] D. DeVoe, Piezoelectric thin film micromechanical beam resonators, Sensors and Actuators A: Physical 88 (2001) 263–272.

[29] G. Piazza, A. Pisano, Two-port stacked piezoelectric aluminum nitride contour-mode resonant mems, Sensors and Actuators A: Physical 136 (2007) 638–645.

[30] J. D. Adams, L. Manning, B. Rogers, M. Jones, S. Minne, Self-sensing tapping mode atomic force microscopy, Sensors and Actuators A: Physical 121 (2005) 262–266.

[31] K. Tsubouchi, N. Mikoshiba, Zero-temperature-coefficient saw devices on aln epitaxial films, IEEE Transactions on Sonics and Ultrasonics 32 (1985) 634.

[32] Y.-C. Hsua, C.-C. Wub, C.-C. Leeb, G. Z. Caoc, I. Y. Shen, Demonstration and characterization of pzt thin-film sensors and actuators for meso- and micro-structures, Thin Solid Films 485 (2005) 42–46.

[33] M.-A. Dubois, P. Muralt, Properties of aluminum nitride thin films for piezoelectric transducers and microwave filter applications, Applied Physics Letters 74 (20) (1999) 3032–3034.

[34] H. Matthews (Ed.), Surface Wave Filters, John Wiley and Sons, 1977.

[35] G. Carlotti, G. Socino, A. Petri, V. E., Acoustic investigation of the elastic properties of zno films, Applied Physics Letters 51 (23) (1987) 1889–1891.

[36] H. Iwanaga, A. Kunishige, S. Takeuchi, Anisotropic thermal expansion in wurtzite-type crystals, Journal of Material Science 35 (2000) 2451–2454.

[37] C. K. Lee, S. Cochran, A. Abrar, F. Placido, Thick aluminium nitride films deposited by room-temperature sputtering for ultrasonic applications, Ultrasonics 42 (2003) 485–490.

[38] H. S. Nalwa (Ed.), Handbook of Thin Film Materials, Vol. 3, Academic Press, 2002.

[39] L. E. McNeil, M. Grimsditch, R. H. French, Vibrational spectroscopy of aluminum nitride, Journal of the American Ceramic Society 75 (5) (1993) 1132.

[40] Y. Li, Ph.D. thesis.

[41] K. Oldham, Microdevices for vibration suppression in computer hard disk drives, Ph.D. thesis, University of California, Berkeley (2006).

[42] G. Perluzzo, C. Jen, E. Adler, Characteristics of reactive magnetron sputtered zno films, in: Proceedings of the Ultrasonics Symposium, Vol. 1, 1989, pp. 373–376.

[43] J. Lee, S. Sanghyon Kwack, H. J. Kim, Effects of substrates roughness on c-axis preferred orientation of zno films deposited by rf magnetron sputtering, in: Proceedings of the Material Research Society Symposium, Vol. 672, 2001, pp. O8.20.1–O8.20.6.

[44] D. J. Ewins, Modal Testing: theory, practice and application, 2nd Edition, John Wiley and Sons, 2000.

[45] S. O. R. Moheimani, A. J. Fleming, Piezoelectric transducers for vibration control and damping, Springer-Verlag, 2006.

[46] Y. Miyahara, M. Deschler, T. Fujii, S. Watanabe, H. Bleuler, Non-contact atomic force microscope with a pzt cantilever used for deflection sensing, direct oscillation and feedback actuation, Applied Surface Science 188 (2002) 450–455.

[47] J. S. Vipperman, R. L. Clark, Hybrid analog and digital adaptive compensation of piezoelectric sensoriactuators, Presented at AIAA/ASME Adaptive Structures Forum, New Orleans, LA, April 1995, paper AIAA-95-1098-CP.

[48] X. Huang, R. Nagamune, R. Horowitz, A comparison of multirate robust track-following control synthesis techniques for dual-stage and multi-sensing servo systems in hard disk drives, IEEE Transactions on Magnetics 42 (2006) 1896–904.

[49] R. Conway, R. Horowitz, A quasi-newton algorithm for lqg controller design with variance constraints, in: Proceedings of ASME Dynamic Systems and Control Conference, Ann Arbor, 2008, paper DSCC2008-2239.

[50] R. Conway, A μ synthesis approach to guaranteed cost control of track-following servos, in: Proceedings of the 17th IFAC World Congress, South Korea, 2008.

[51] K. Zhou (Ed.), Essentials of Robust Control, Prentice Hall, 1998.

[52] E. Hendricks, O. Jannerup, P. H. Sorensen, Linear Systems Control: Deterministic and Stochastic Methods, Springer, 2008.

[53] K. Mori, T. Munemoto, H. Otsuki, Y. Yamaguchi, K. Akagi, A dual-stage magnetic disk drive actuator using a piezoelectric device for a high track density, IEEE Transactions on Magnetics 27 (1991) 5298–5300.

[54] Z. He, V. Venkataramanan, C. Y. Ng, E. H. Ong, Vibration characteristics of hard disk drives with different internal air pressures, in: Digest of the Asia Pacific Magnetic Recording Conference, Singapore, 2009, pp. DP–07.

[55] H. Gross, Off-track vibrations of the read-write heads in hard disk drives, Ph.D. thesis, University of California, Berkeley (2003).

[56] S. Haykin, Adaptive Filter Theory, Prentice Hall, 1991.

[57] R. Horowitz, B. Li, Adaptive track-following servos for disk file actuators, IEEE Transactions on Magnetics 32 (3) (1996) 1779–1786.

[58] S. S. Pannu, R. Horowitz, Increased disturbance rejection for hard disk drives by using accelerometers, Journal of Information Storage and Processing Systems 1 (1999) 95–103.

[59] J. G. Proakis, C. M. Rader, F. Ling, C. L. Nikias, Advanced Digital Signal Processing, Macmillan, 1992.

[60] S.-J. Chen, J. S. Gibson, Feedforward adaptive noise control with multivariable gradient lattice filters, IEEE Transactions on Signal Processing 49 (2001) 511–520.

[61] P. K. Orzechowski, N. Y. Chen, J. S. Gibson, T.-C. Tsao, Optimal suppression of laser beam jitter by high-order RLS adaptive control, IEEE Transactions on Control Systems Technology 16 (2008) 255–267.

[62] K. J. Åstrom (Ed.), Stochastic Control Theory, Dover, 2006.

[63] A. Datta, J. Ochoa, Adaptive internal model control: $h2$ optimiztion for stable plants, Automatica 34 (1998) 75–82.

Appendix A

Special Processing Procedures

A.0.1 ZnO Deposition and Patterning

1. Place the steel wafer on top of Si handle wafer. Situate Si bar on top of the steel wafer. Secure in place with clips. See Figs. A.1 and A.2.

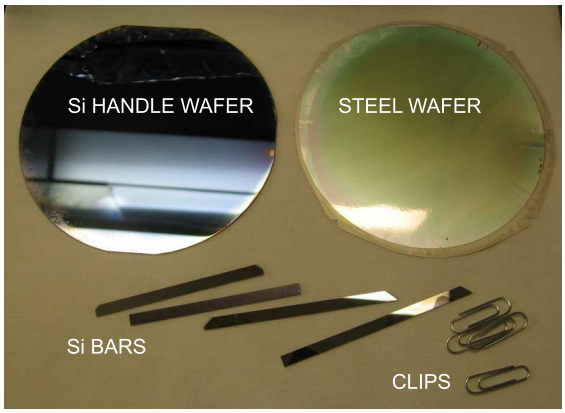

Figure A.1: Pieces required for constraining steel wafer prior to ZnO deposition.

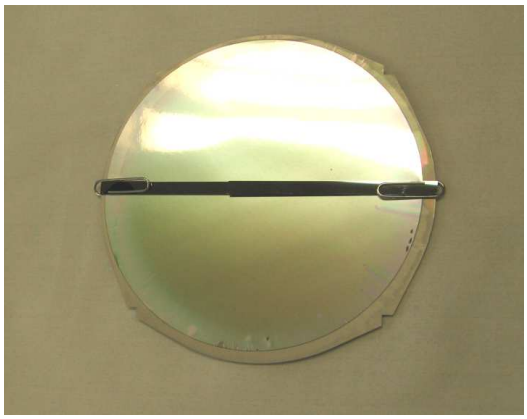

Figure A.2: Steel wafer secured to handle wafer with clamping bar.

2. Deposit ZnO using RF magnetron sputtering. Process conditions are 3.5 mTorr Ar, 3.5 mTorr O_2, 200 W RF power, and 300^{o}C substrate temperature. Allow to fully cool for 1 hour before removing wafer from vacuum chamber.

3. Lithography must be performed within an hour or two of sputtering to avoid cracking of the ZnO film.

4. Using a plastic pipette, carefully inject a drop of water under the steel wafer on each side of the bar. See Fig. A.3.

5. Using a clean lab towel, gently press down the top of the steel wafer to ensure a uniform water bond. See Fig. A.4

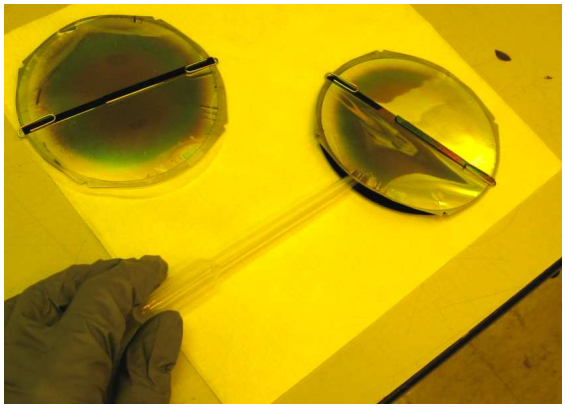

Figure A.3: Injecting water droplet underneath steel wafer.

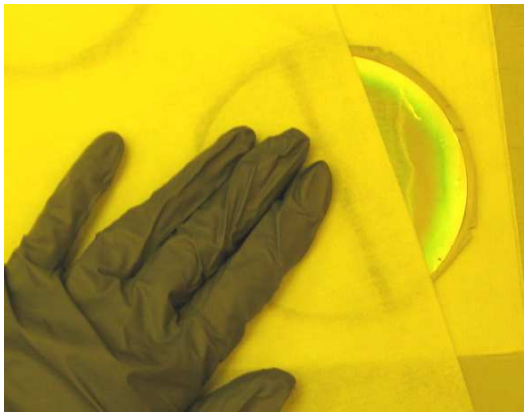

Figure A.4: Pressing down steel wafer to secure water bond.

6. Carefully remove the clips and bar; the wafer should be temporarily bonded to the Si handle wafer.
7. Spin-coat I-line photoresist at 3000 RPM for 30 seconds.
8. Soft bake on on hot plate at 90^{o}C for 60 seconds.
9. Expose for about 20 seconds.
10. Develop. After submerging the wafer in the developer, the steel wafer will become separate from the handle wafer. Gently hold down the center of the wafer with tweezers until developing is complete, then remove the wafer and handle together by clamping them both with the tweezers. Rinse with water, then sit the wafers on a flat surface, on a lab towel. As gently as possible, press the steel wafer back onto the handle wafer.
11. Hard bake on hot place at 90^{o}C for 120 seconds.
12. Wet etch the ZnO in a solution of acetic acid, phosphoric acid, and water in a ratio of 10:10:200. The steel wafer will again become separated from the handle wafer, but after ZnO etching it will flatten out and will no longer need to be constrained. Rinse with water and dry.

A.0.2 Thick Photoresist Application for Steel Etching

1. Clean wafers with acetone, isopropyl alcohol, and deionized water.
2. Treat wafer with HMDS using vacuum oven.
3. Adhere steel wafer to Si handle wafer using a water bond.

4. Spin SPR 220 thick resist onto top side by ramping first to 300 RPM for 5 seconds, and then to 1800 RPM for 30 seconds.

5. Remove waterbond, dry the wafer, and then softbake on a hot plate at 115^{o}C for 5 minutes.

6. Cool wafer and reapply water bond.

7. Expose wafer for about 25 seconds.

8. Allow exposed photoresist to sit for 30 minutes.

9. Remove water bond, dry the wafer, and do a post-exposure bake on a hot plate at 100^{o}C for 6.5 minutes.

10. Cool wafer, then develop using the proper developer designated for thick resist. It will take around 3-7 minutes to develop the wafer.

11. Hardbake in small oven at 80^{o}C for 2 hours.

12. Cool the wafer.

13. Cut a piece of cellulose paper (found around optical microscopes in the cleanroom) into a circle slightly larger than the wafer. Cut four corner notches out of the circle. Lay this paper onto the top side of the wafer.

14. Apply dots of photoresist to the wafer at the four exposed corners.

15. Cover with Si handle wafer and press at the four corners to adhere to the steel wafer. The cellulose paper will be sandwiched between the two wafers, protecting the top-side photoresist. Wait a few minutes and check the bond.

16. Turn over the stack and spin thick photoresist, as before, on the back side of the steel wafer.

17. Wait 5 minutes. Then carefully remove handle wafer and cellulose paper.

18. Hardbake in small oven at 70^{o}C for about 10 hours.